ABSTRACT

Title of Dissertation: DETECTION, EVALUATION, AND ANALYSIS OF GLOBAL FIRE ACTIVITY USING MODIS DATA

Louis Giglio, Doctor of Philosophy, 2006

Dissertation directed by: Professor Christopher O. Justice
Department of Geography

Global biomass burning plays a significant role in regional and global climate change, and spaceborne sensors offer the only practical way to monitor fire activity at these scales. This dissertation primarily concerns the development, evaluation, and use of the NASA Terra and Aqua MODIS instruments for fire monitoring. MODIS is the first satellite sensor designed specifically for global monitoring of fires. An improved operational fire detection algorithm was developed for the MODIS instrument. This algorithm offers a sensitivity to small, cool fires and minimizes false alarm rates. To support the accuracy assessment of the MODIS global fire product, an operational fire detection algorithm was developed and evaluated for the ASTER instrument, which provides higher resolution observations coincident with the Terra MODIS. The unique data set of multi-year MODIS day and night fire observations was used to analyze the global distribution of biomass burning using five different temporal metrics which

included, for the first time, mean fire radiative power, a measure of fire intensity. The metrics show the planetary extent, seasonality, and interannual variability of fire. Recognizing differences in fire activity between morning and afternoon overpasses, the impact of the diurnal cycle of fire activity was addressed using seven years of fire data from the VIRS sensor on-board the TRMM satellite. A strong diurnal cycle was found in all regions, with the time of peak burning varying between approximately 13:00 and 18:30 local time. Given interest in area burned among atmospheric chemical transport and carbon cycle modelers, a data set was developed utilizing the MODIS global fire and vegetation cover products to estimate monthly burned area at 1-degree spatial resolution. The methods, products and results presented in this thesis provide the global change research and fire management communities with products for global fire monitoring and are currently being used in the development of the next generation of operational satellite fire monitoring systems.

DETECTION, EVALUATION, AND ANALYSIS OF GLOBAL FIRE ACTIVITY USING MODIS DATA

by

Louis Giglio

Dissertation submitted to the Faculty of the Graduate School of the
University of Maryland, College Park in partial fulfillment
of the requirements for the degree of
Doctor of Philosophy
2006

Advisory Committee:

Professor Christopher O. Justice, Chair
Dr. Ivan A. Csiszar
Professor Richard F. Ellis
Professor Eric S. Kasischke
Professor Shunlin Liang

PREFACE

Some of the research in this dissertation has been previously published, or has been accepted for publication, as peer-reviewed journal articles, specifically the material presented in Chapters 2, 4, and 6. The research in these chapters, as well as the remainder of the thesis, was carried out in its entirety by Louis Giglio.

ACKNOWLEDGEMENTS

First and foremost I thank Chris Justice for encouraging me to pursue a doctorate and supporting me steadfastly throughout the process. I also thank the members of my committee, Ivan Csiszar, Richard Ellis, Eric Kasischke, and Shunlin Liang for supplying guidance and generously providing so much of their time.

For helpful technical discussions I thank Dominick Giglio (my father), Tatiana Loboda, Doug Morton, Jorge Pinzon, Jim Randerson, David Roy, Wilfrid Schroeder, Dan Slayback, and Guido van der Werf. I thank Jackie Kendall and Mike Darzi for their encouragement and assistance in meeting the demands of work during my doctoral studies. Special thanks go to Regina Oglesby, who cheerfully provided help on numerous occasions.

Finally, I thank my family for their support and patience, in particular my wife and daughter for accomodating the seemingly endless number of hours spent on my doctorate over the past four years, and my father for a thorough cover-to-cover reading of the first draft of my dissertation.

TABLE OF CONTENTS

LIST OF TABLES

LIST OF FIGURES

Chapter 1

Introduction

1.1 Research Goals and Objectives

The overarching theme of the research presented in this dissertation is the utilization, analysis, and evaluation of MODIS active fire data for fire monitoring. The specific objectives of this work were to:

1. Develop a robust MODIS active-fire detection algorithm that performs reasonably well over the entire globe.

2. Develop a robust active-fire detection algorithm for the ASTER sensor which will provide high resolution (30 m) fire maps suitable for validation of the coarser resolution fire maps produced from Terra MODIS observations (and potentially from VIRS and SEVIRI observations as well). ASTER fire maps also provide useful information for regional fire studies.

3. Develop a global, coarse-resolution MODIS active-fire data set that addresses many of the needs of the global modeling community.

4. Use the global data set to quantify the global spatial and temporal distributions of fire activity as observed by the Terra and Aqua MODIS instruments.

5. Determine in which regions of the globe a diurnal fire cycle exists, and determine the characteristics of the cycle (peak time, width of peak, etc.) within these regions.

6. Examine the implications of a diurnal fire cycle for developing long-term records of fire activity from current and future satellite sensors.

7. Explore methods for using the multi-year, global active fire data set to generate global, spatially explicit estimates of burned area. An associated objective was to gain further insight into the relationship between "fire pixels" observed while a fire is actively burning, and the remaining post-fire burn scar.

1.2 Background

1.2.1 Fire and Global Change

For millenia, fire has been a pervasive agent of change acting upon the terrestrial landscape. While fire originated as a strictly "natural" process, the phenomenon has become decidedly anthropogenic in many parts of the world. On a global scale, the overwhelming majority of fires are now initiated by humans as a tool for forest and brush clearing, crop and pasture maintenance, fuel reduction, charcoal production, cooking, hunting, heating, and occasionally, arson [Andreae, 1991, Malingreau and

Grégoire, 1996]. A smaller number of natural fires (or "wildfires") occur each year, usually started by lightning.[1]

Fire has long been acknowledged as an important factor in human history, and has for some time been recognized as an important ecological process which influences, among other attributes of a community, species composition (both floral and faunal) and plant productivity [Whelan, 1995]. The realization that fire plays a significant role in regional and global climate change, however, has emerged comparatively recently following the landmark study of Crutzen et al. [1979]. In the context of global change, the role of the phenomenon is manifested through a host of different mechanisms; a representative (but incomplete) list includes the following:

- Fire is an important process in the global carbon cycle – one that rapidly transfers carbon stored in biomass to the atmosphere – and a major source of trace gas and aerosol emissions [Crutzen et al., 1979, Crutzen and Andreae, 1990]. Among a host of other species, these trace gases include CO_2, a greenhouse gas that is thought to be the primary cause of the general warming of the Earth's atmosphere over the past century.

- Fire alters the albedo of the Earth's surface through the removal of vegetation and the deposition of ash and char. This directly effects soil temperature, which in turn alters the rates of microbial respiration and evapotranspiration.

[1] Other natural ignition sources are rare but include volcanic activity and heat produced during microbial decomposition of organic matter.

- Particulate matter produced during combustion can affect cloud formation and inhibit precipitation [Rosenfeld, 1999].

It is important to also recognize that changes in climate can affect changes in *fire regime*, a combination of the type of fire which occurs in a given region (e.g., low-intensity surface or high-intensity crown), the frequency at which fires occur, and the seasonality of burning. There is consequently the potential for substantial feedback between fire and the environment.

1.2.2 Global Fire Data

The initial global biomass burning studies of trace-gas emissions by Crutzen et al. [1979] and Seiler and Crutzen [1980] relied entirely on land-use, population, and national statistics as a source of information about worldwide fire activity. Later fire emissions studies improved this approach by using more timely statistics and incorporating regional or land-cover-specific fire return intervals [e.g., Hao et al., 1990], but remained beset by large uncertainties stemming from the paucity of timely biomass burning information. The extent of this data void was further elucidated as subsequent research revealed the broader impact of global biomass burning on atmospheric chemistry, the radiation budget, and the hydrological and biogeochemical cycles [Crutzen and Andreae, 1990, Penner et al., 1992]. By the early 1990's, a clear consensus on the need for better sources of global fire data had arisen.

Following the deployment of the first Advanced Very High Resolution Radiometer

(AVHRR) on-board the TIROS-N satellite in 1978, Dozier [1981] and Matson and Dozier [1981] showed that the middle-infrared channel of this sensor enabled the detection of sub-pixel, high temperature sources, in particular fires, within its field of view. A number of applied AVHRR fire-detection studies followed [e.g., Malingreau et al., 1985, Muirhead and Cracknell, 1985, Flannigan and Vonder Haar, 1986, Matson and Holben, 1987] and, in conjunction with the marked increase in the availability and use of satellite data in land studies over the next decade, demonstrated the potential for spaceborne sensors to supply large-scale information about biomass burning [Malingreau, 1990, Justice et al., 1993].

As the development of remotely-sensed fire data sets progressed, emissions studies began to use these data on a short term, regional basis [e.g., Kaufman et al., 1990, Setzer and Pereira, 1991, Scholes et al., 1996]. The arrival of global (or near global), multi-year fire data sets starting in the late 1990's quickly led to the widespread adoption of these data in atmospheric chemistry, fire, emissions, and carbon cycle studies [e.g., Barbosa et al., 1999, Duncan et al., 2003, van der Werf et al., 2003, Heald et al., 2003, Streets et al., 2003, Edwards et al., 2004, van der Werf et al., 2004]. One advantage these data offer over inventories is that they capture interannual variability.[2] As will be discussed in Section 1.2.4, however, some important issues and limitations exist with respect to the use of remotely-sensed fire data. Consequently, considerable

[2]For some types of small fires, such as cooking and heating fires, inventories are 1) relatively accurate and 2) the only source of information about such fires, and are unlikely to be replaced any time in the foreseeable future.

interest remains in producing consistent, reliable fire-related data sets from spaceborne sensors, and in improving the quality and utility of these data sets.

1.2.3 Satellite-Based Fire Monitoring: Sensors and Data Sets

Spaceborne sensors now monitor the Earth continuously, and offer the only practical way to monitor fire activity on a global scale. In addition to providing fire data for use in long-term studies, these sensors provide synoptic snapshots of fire activity in near-real time to support operational fire management.

To date, a number of large scale, multi-year fire data sets have been produced using observations acquired by various satellite-based sensors. A summary of these sensors and data sets is provided here and in Table 1.1, and will facilitate the subsequent discussion of the issues entailed in using remotely-sensed fire data (Section 1.2.4), as well as the discussion of the thesis organization in Section 1.3.

1.2.3.1 AVHRR

The *Advanced Very High Resolution Radiometer* (AVHRR) has been deployed on a long series of operational NOAA satellites spanning well over two decades and continuing to the present. The AVHRR was the first spaceborne instrument capable of large-scale fire detection. As first shown by Dozier [1981] and Matson and Dozier [1981], the 3.8 μm mid-infrared channel of this instrument is capable of detecting active fires very much smaller than the nominal 1 km sensor footprint. Subsequent refinements have produced a veritable zoo of fire detection algorithms for the AVHRR

[e.g., Kaufman et al., 1990, Lee and Tag, 1990, Setzer and Pereira, 1991, Langaas, 1993b, Kennedy et al., 1994, Eva and Flasse, 1996, Flasse and Ceccato, 1996, Justice et al., 1996, Randriambelo et al., 1998, Giglio et al., 1999, Boles and Verbyla, 2000, Li et al., 2000, Lasaponara et al., 2003, Soja et al., 2004]. While numerous regional AVHRR fire data sets have been produced [e.g., Sukhinin et al., 2004], the sole AVHRR active fire data set offering complete global coverage is the 18-month AVHRR Global Fire Product [Stroppiana et al., 2000b], produced under the auspices of the International Geosphere-Biosphere Programme.

1.2.3.2 GOES Imager

This scanning radiometer, simply referred to as *Imager*, is carried on-board two Geostationary Operational Environmental Satellites (GOES) "parked" in geostationary orbits to provide high temporal-frequency coverage of North and South America. The nominal spatial resolution of the Imager channels useful for fire detection is 4 km. Fire detection is performed using the method of Prins et al. [1998], an extension of earlier work by Prins and Menzel [1992] using the coarser-resolution GOES Visible Infrared Spin Scan Radiometer Atmospheric Sounder (VAS).

1.2.3.3 OLS

Multiple *Operational Linescan System* (OLS) instruments have been deployed on-board a suite of Defense Meteorological Satellite Program (DMSP) satellites occupying polar, sun-synchronous orbits. The OLS includes a high gain,

visible/near-infrared channel which permits fires (and other light sources) to be detected in nighttime imagery [Elvidge et al., 1996]. Under nighttime operating conditions the nominal spatial resolution of this channel is either 1.7 or 4 km, depending on whether or not the higher-resolution “fine” acquisition mode is in use [Elvidge et al., 1996]. At any given time, four DMSP satellites are in operation.

1.2.3.4 ATSR-2 and AATSR

The second *Along-Track Scanning Radiometer* (ATSR-2), on-board the now defunct ERS-2 spacecraft, was succeeded by the *Advanced Along-Track Scanning Radiometer* (AATSR), on-board the ENVISAT satellite (with nearly identical orbital characteristics). Both sensors have a nominal spatial resolution of 1 km. The low saturation level of the mid-infrared channel on both sensors generally restricts fire detection to nighttime imagery. The ATSR World Fire Atlas [Arino and Rosaz, 1999] is currently the longest time series of global active fire data, spanning 1996 through the present.

1.2.3.5 VIRS

The *Visible and Infrared Scanner* (VIRS) is carried on-board NASA’s Tropical Rainfall Measuring Mission (TRMM) satellite. This five-channel radiometer has a nominal spatial resolution of 2.5 km. TRMM is unique among other satellites used for fire monitoring in that it occupies a precessing orbit that permits sampling of the diurnal

cycle. Fire detection is performed using the method of Giglio et al. [2003b].[3] The archive of VIRS fire observations covers the time period from late December 1997 through the present.

1.2.3.6 MODIS

Two *Moderate Resolution Imaging Spectroradiometer* (MODIS) instruments are carried on-board NASA's Terra and Aqua satellites which occupy polar, sun-synchronous orbits. MODIS is unique among current sensors in that is has high-saturation 4 and 11 μm channels designed specifically for fire monitoring. The nominal spatial resolution of the relevant MODIS fire channels is 1 km. A suite of MODIS fire products is available [Justice et al., 2002], spanning the time period from November 2000 through the present.

[3] An alternative VIRS fire data set by Ji and Stocker [2002] is also currently produced, but has been shown to suffer from a very high incidence of false alarms along cloud edges and in areas of sun glint [Giglio and Kendall, 2004]. Contamination from the resulting false fire pixels can be so severe as to significantly misrepresent the seasonality of fire activity, as in Generoso et al. [2003].

Table 1.1: Summary of sensors currently used for fire monitoring for which long-term fire data sets have been produced. The "Day/Night Detection" column indicates whether the sensor can be used for both daytime and nighttime (DN) fire detection, or nighttime (N) fire detection only.

Sensor	Satellite Orbit	Spatial Resolution (km)	Day/Night Detection
AVHRR	sun-synchronous polar	1.1	DN
GOES Imager	geostationary	4	DN
OLS	sun-synchronous polar	1.7 or 4	N
ATSR-2/AATSR	sun-synchronous polar	1	N
VIRS	precessing	2.5	DN
MODIS	sun-synchronous polar	1	DN

1.2.4 Satellite-Based Fire Monitoring: Issues

With such a strong reliance on satellite data, it is important to recognize and understand a number of issues surrounding the use of these data. This is especially important in the context of biomass burning since 1) there is at present a plethora of satellites and sensors used for fire monitoring, and 2) very few of these systems were actually designed with fires in mind, and consequently lack the specialized capabilities required for unbiased fire monitoring. Among the most important issues are those in the following list:

- To date, most sensors used for fire monitoring detect (and in some instances, characterize) the flaming and smoldering regions of an actively burning fire. These regions are generally much smaller and far more transient than the “burn scars” that generally persist long after the active fire has finished burning. For many applications, however, such as emissions modeling, it is necessary to know the size of the burn scar. At present there is a paucity of such information.

- Due to limitations of the instrument and the detection algorithm, and obscuration by clouds, smoke, and forest canopy, not every fire is detected. The envelope of detectable fires (in terms of their size and temperature) is dependent upon observation conditions and the particular instrument and detection algorithm being used.

- Not every fire detection is real. The frequency at which these false alarms arise is

dependent upon observation conditions and the particular instrument and detection algorithm being used.

- The suite of satellites and sensors used for fire monitoring provide very different spatial and temporal sampling strategies. This can lead to inconsistencies in the respective fire data sets.

- The fire information currently provided by spaceborne sensors often does not exactly match the fire information desired by the fire community.

While this list is not exhaustive, it captures the most important elements from the perspective of long-term, global fire monitoring. For some applications the list would likely be somewhat different. From the standpoint of real-time operational fire management, for example, data latency would have a much higher priority than assumed here.

1.3 Organization of the Thesis

This dissertation is organized into seven chapters, five of which are self contained. The thesis is centered around the utilization, analysis, and evaluations of MODIS fire data, addressing the issues discussed in the previous section.

Chapter 1 (this chapter) presents a brief overview of biomass burning and satellite-based fire monitoring, and provides a context for the work presented in this dissertation.

Chapter 2 describes an operational fire detection algorithm developed for the MODIS instruments to produce a new generation of active fire products. The algorithm, which incorporates many refinements to earlier approaches, offers greater sensitivity to smaller, cooler fires, as well as a lower false alarm rate under many conditions.[4]

Chapter 3 presents an operational fire detection algorithm developed for the Advanced Spaceborne Thermal Emission and Reflection Radiometer (ASTER). ASTER is a high resolution imaging radiometer co-resident with the MODIS instrument on-board the Terra satellite. As such, high resolution ASTER fire masks have become an important tool in the ongoing accuracy assessment (validation) of the Terra MODIS active fire products generated using the algorithm developed in Chapter 2. Since ASTER lacks channels in the mid-infrared, however, the resulting fire detection algorithm is somewhat different than those developed for the sensors mentioned in Section 1.2.3. An evaluation of the algorithm is also presented.

In Chapter 4 multi-year fire products developed using the algorithm developed in Chapter 2 are analyzed. An analysis of the global distribution of biomass burning from MODIS is presented using five different temporal metrics derived from five years of data. As part of this analysis and for the first time, the global distribution of the fire radiative power (FRP), a relatively new remotely sensed quantity first proposed by Kaufman et al. [1998b] is presented. This chapter also contains a preliminary analysis of the *diurnal fire cycle* – the systematic variation in fire activity with respect to time of

[4]This chapter is a slightly revised version of material published in Giglio et al. [2003a].

day – based on three years of Terra and Aqua MODIS observations. The chapter concludes with a brief investigation into the consistency of the fire time series recorded by the two MODIS instruments.[5]

Recognizing the bias that can be introduced from differences in orbital sampling, Chapter 5 presents a detailed look at the diurnal fire cycle in 15 different regions of the tropics and subtropics. Knowledge of this cycle is critically important for interpreting (and potentially correcting) any long-term time series of active fire observations.

There is large demand for additional fire information beyond that provided by current active fire products. In particular, those concerned with trace gas emissions and resource management require burned area [Kasischke and Penner, 2004]. Chapter 6 explores the use of the product described in Chapter 4 in combination with MODIS vegetation data and fire-pixel cluster information to produce coarse resolution, spatially and temporally-explicit global estimates of burned area.[6]

Finally, in Chapter 7, the implications of the results described in previous chapters with respect to the production of a consistent, long term fire record from current and future satellite sensors are summarized and future areas for research are identified.

The structure of the thesis is shown in Fig. 1.1.

---

[5]This chapter is an expanded version of a forthcoming paper by Giglio et al. [2006a].

[6]Together, this chapter and Appendix B are expanded versions of material recently published in Giglio et al. [2006b].

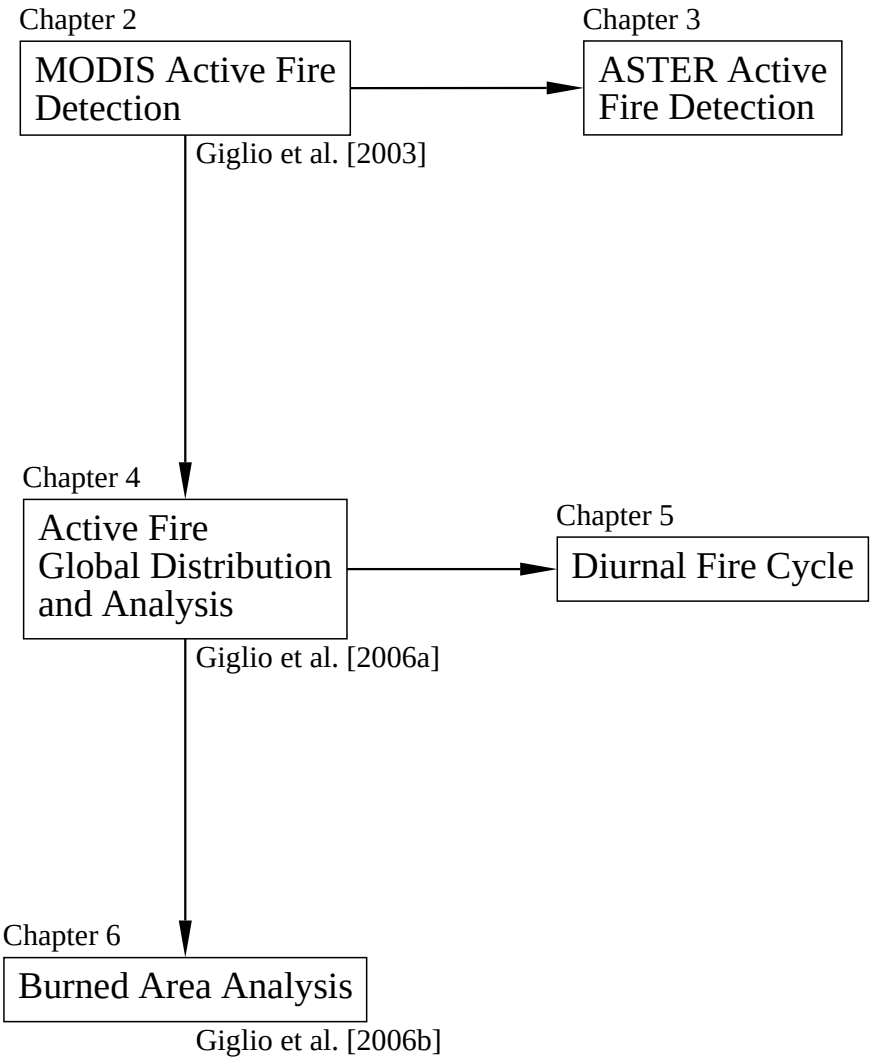

Figure 1.1: Organization of thesis.

Chapter 2

A MODIS Fire Detection Algorithm

2.1 Introduction

As part of NASA's Earth Observing System (EOS), the Moderate Resolution Imaging Spectroradiometer (MODIS) is carried on both the Terra and Aqua satellites. The MODIS instruments, which began collecting data in February 2000 (Terra) and June 2002 (Aqua), are being used to generate oceanic, atmospheric, and terrestrial data products [Kaufman et al., 1998a, Masuoka et al., 1998]. Since launch, emphasis has been given to characterizing instrument performance, determining and monitoring the quality of the data products, and undertaking validation [Morisette et al., 2002]. Based on this understanding, improvements have been made to all of the algorithms. The MODIS active fire products fall within the suite of terrestrial products, and provide information about actively burning fires, including their location and timing, instantaneous radiative power, and smoldering ratio, presented at a selection of spatial and temporal scales [Kaufman et al., 1998b, Justice et al., 2002]. A detection algorithm which identifies the active fires within each MODIS swath forms the basis of these

products.

Although the original MODIS fire detection algorithm of Kaufman et al. [1998b] functioned reasonably well following several initial post-launch revisions collectively known as “version 3” [Justice et al., 2002], two significant problems limited the overall quality of the product. Firstly, persistent false detections occurred in some deserts and sparsely vegetated land surfaces, particularly in northern Ethiopia, the Middle East, and central India. Not unexpectedly, most of these were caused by the algorithm’s absolute threshold tests. Secondly, relatively small (yet generally obvious) fires were frequently not detected. In response to these problems, we have developed a replacement version 4 contextual algorithm that offers superior sensitivity to smaller, cooler fires, and yields fewer blatant false alarms. In this chapter we describe this algorithm.

2.2 Algorithm description

The improved detection algorithm is based on the original MODIS detection algorithm [Kaufman et al., 1998b], heritage algorithms developed for the Advanced Very High Resolution Radiometer (AVHRR) and the Visible and Infrared Scanner (VIRS) [Giglio et al., 1999, 2003b], and experience with the first two years of high quality MODIS data.

The algorithm uses brightness temperatures derived from the MODIS 4 μm and 11 μm channels, denoted by T_4 and T_{11}, respectively. The MODIS instrument has two 4 μm channels, numbered 21 and 22, both of which are used by the detection

algorithm. Channel 21 saturates at nearly 500 K; channel 22 saturates at 331 K. Since the low-saturation channel (22) is less noisy and has a smaller quantization error, T_4 is derived from this channel whenever possible. However, when channel 22 saturates or has missing data, it is replaced with the high saturation channel to derive T_4. T_{11} is computed from the 11 μm channel (channel 31), which saturates at approximately 400 K for the Terra MODIS, and 340 K for the Aqua MODIS. The 12 μm channel (channel 32) is used for cloud masking; brightness temperatures for this channel are denoted by T_{12}.

The 250 m resolution red and near-infrared channels, aggregated to 1 km, are used to reject false alarms and mask clouds. These reflectances are denoted by $\rho_{0.65}$ and $\rho_{0.86}$, respectively. The 500-m 2.1 μm band, also aggregated to 1 km, is used to reject water-induced false alarms; the reflectance in this channel is denoted by $\rho_{2.1}$. A summary of all MODIS bands used in the algorithm is shown in Table 2.1.

Table 2.1: MODIS channels used in detection algorithm.

Channel Number	Central Wavelength (μm)	Purpose
1	0.65	Sun glint and coastal false alarm rejection; cloud masking.
2	0.86	Bright surface, sun glint, and coastal false alarm rejection; cloud masking.
7	2.1	Sun glint and coastal false alarm rejection.
21	4.0	High-range channel for active fire detection.
22	4.0	Low-range channel for active fire detection.
31	11.0	Active fire detection, cloud masking.
32	12.0	Cloud masking.

2.2.1 Cloud and water masking

Cloud detection was performed using a technique based on that used in the production of the International Geosphere Biosphere Program (IGBP) AVHRR-derived Global Fire Product Stroppiana et al. [2000b]. Daytime pixels are considered to be cloud-obscured if the following condition is satisfied:

$$(\rho_{0.65}+\rho_{0.86} > 0.9) \quad \text{or} \quad (T_{12} < 265\,\mathrm{K}) \quad \text{or} \quad (\rho_{0.65}+\rho_{0.86} > 0.7 \quad \text{and} \quad T_{12} < 285\,\mathrm{K})$$

Nighttime pixels are flagged as cloud if the single condition $T_{12} < 265\,\mathrm{K}$ is satisfied. These simple criteria were found to be adequate for identifying larger, cooler clouds, but consistently missed small clouds and cloud edges. One advantage, however, is that fire pixels were never observed to have been mistakenly flagged as cloud. As noted previously [Seielstad et al., 2002, Justice et al., 2002], this problem has been experienced with other cloud masking methods, including the MODIS cloud mask product [Ackerman et al., 1998]. Recent improvements in the latter, however, may allow use of the MODIS cloud mask product to be reincorporated into the fire product during a future reprocessing.

Water pixels were identified using the 1 km pre-launch land/sea mask contained in the MODIS geolocation product. Significant errors have been noted in this data set, and an improved water mask is being developed by members of the MODIS Science Team.

2.2.2 Detection algorithm components

The purpose of the detection algorithm is to identify pixels in which one or more fires are actively burning at the time of the satellite overpass; such pixels are commonly referred to as “fire pixels”. As with most other satellite-based fire detection algorithms, our approach exploits the different response of middle-infrared and long-wave-infrared bands to scenes containing hot sub-pixel targets [Dozier, 1981, Matson and Dozier, 1981]. In particular, the algorithm looks for a significant increase in radiance at 4 μm, in both an absolute sense as well as relative to the observed 11 μm radiance. This characteristic active-fire signature is the result of the enormous difference in 4 and 11 μm blackbody radiation emitted at combustion temperatures as described by the Planck function.

The algorithm examines each pixel of the MODIS swath, and ultimately assigns it to one of the following classes: *missing data*, *cloud*, *water*, *non-fire*, *fire*, or *unknown*. Pixels lacking valid data are immediately classified as *missing data* and excluded from further consideration. Cloud and water pixels are identified using the previously described cloud and water masks, and are assigned to the classes *cloud* and *water*, respectively. The fire detection algorithm considers only those land pixels that remain.

2.2.2.1 Identification of potential fire pixels

A preliminary classification is used to eliminate obvious non-fire pixels. Those pixels that remain are considered in subsequent tests (described in the next sections) to

determine if they do in fact contain an active fire.

A daytime pixel is identified as a *potential fire pixel* if $T_4 > 310\,\mathrm{K}$, $\Delta T > 10\,\mathrm{K}$, and $\rho_{0.86} < 0.3$, where $\Delta T = T_4 - T_{11}$. For nighttime pixels the reflective test is omitted and the T_4 threshold reduced to 305 K. Pixels failing these preliminary tests are immediately classified as *non-fire* pixels.

There are two logical paths through which fire pixels can be identified. The first consists of a simple absolute threshold test. This threshold must be set sufficiently high so that it is triggered only by unambiguous fire pixels, i.e. those with very little chance of being a false alarm. The second path consists of a series of contextual tests designed to identify the majority of active fire pixels which are less obvious.

2.2.2.2 Absolute threshold test

The absolute threshold criterion remains identical to one employed in the original algorithm [Kaufman et al., 1998b]:

$$T_4 > 360\,\mathrm{K} \quad (320\,\mathrm{K}\text{ at night}). \tag{2.1}$$

Despite the high daytime threshold, the utility of this test hinges upon adequate sun-glint rejection, otherwise glint-induced false alarms can occur. This issue is addressed in Section 2.2.2.6. Nighttime pixels are defined as those having a solar zenith angle $\geq 85°$.

2.2.2.3 Background characterization

In the next phase of the algorithm, which is performed regardless of the outcome of the absolute threshold test, an attempt is made to use the neighboring pixels to estimate the radiometric signal of the potential fire pixel in the absence of fire. Valid neighboring pixels in a window centered on the potential fire pixel are identified and are used to estimate a background value. Within this window, valid pixels are defined as those that 1) contain usable observations, 2) are located on land, 3) are not cloud-contaminated, and 4) are not *background fire* pixels. Background fire pixels are in turn defined as those having $T_4 > 325\,\mathrm{K}$ and $\Delta T > 20\,\mathrm{K}$ for daytime observations, or $T_4 > 310\,\mathrm{K}$ and $\Delta T > 10\,\mathrm{K}$ for nighttime observations.

The window starts as a 3×3 pixel square ring around the potential fire pixel. Due to the triangular along-scan response of the MODIS instrument [Kaufman et al., 1998b], the two along-scan pixels adjacent to the potential fire pixel are deemed unreliable and excluded from the background characterization. The ring is increased to a maximum of 21×21 pixels, as necessary, until at least 25% of the pixels within the window have been deemed valid, and the number of valid pixels is at least eight. During this step, an optimized nearest-neighbor search is used to correct for the "bowtie" effect, or overlap between MODIS scans [Nishihama et al., 1997]. The 21×21 pixel maximum size, though arbitrary, ensures that the background is sampled within $\sim 10\,\mathrm{km}$ of the potential fire pixel, a scale found empirically to be appropriate for preventing false alarms induced by an unrepresentative selection of background pixels.

The number of valid pixels within the background window is denoted by N_{v}. During the characterization process, counts are also made and noted of the number of neighboring pixels rejected as background fires (N_{f}), and the number of neighboring pixels excluded as water (N_{w}).

If a sufficient number of valid neighboring pixels can be identified, several statistical measures are computed. These are: $\overline{T}_4$ and δ_4, the respective mean and mean absolute deviation of T_4 for the valid neighboring pixels; $\overline{T}_{11}$ and δ_{11}, the respective mean and mean absolute deviation of T_{11} for the valid neighboring pixels; and $\overline{\Delta T}$ and $\delta_{\Delta \mathrm{T}}$, the respective mean and mean absolute deviation of ΔT for the valid neighboring pixels. The 4 μm brightness temperature mean and mean absolute deviation of those neighboring pixels that were rejected as background fires are also computed, and are denoted by $\overline{T}_4'$ and δ_4', respectively. These last two quantities will prove useful for rejecting certain types of false alarms. As suggested by Giglio et al. [1999], we employ the mean absolute deviation as a measure of dispersion, rather than the standard deviation, since it is more resistant to outliers [Huber, 1981]. For contextual fire detection algorithms this is highly desirable since contamination of the background window by undetected clouds, water, fires, and other sources is not uncommon.

2.2.2.4 Contextual tests

If the background characterization was successful, a series of contextual threshold tests are used to perform a relative fire detection. These look for the characteristic signature of an active fire in which both the 4 μm brightness temperature (T_4) and the 4 and

11 μm brightness temperature difference (ΔT) depart substantially from that of the non-fire background. Relative thresholds are adjusted based on the natural variability of the background. The tests are:

$$\Delta T > \overline{\Delta T} + 3.5\,\delta_{\Delta \mathrm{T}} \tag{2.2}$$

$$\Delta T > \overline{\Delta T} + 6\,\mathrm{K} \tag{2.3}$$

$$T_4 > \overline{T_4} + 3\,\delta_4 \tag{2.4}$$

$$T_{11} > \overline{T}_{11} + \delta_{11} - 4\,\mathrm{K} \tag{2.5}$$

$$\delta_4' > 5\,\mathrm{K} \tag{2.6}$$

Of these conditions, the first three isolate fire pixels from the non-fire background. The factor of 3.5 appearing in test (2.2) is larger than the corresponding factor of 3 in test (2.4) to help adjust for partial correlation between the 4 and 11 μm observations. Condition (2.5), which is restricted to daytime pixels, is primarily used to reject small convective cloud pixels that can appear warm at 4 μm (due to reflected sunlight), yet cool in the 11 μm thermal channel. It can also help reduce coastal false alarms that sometimes occur when cooler water pixels are unknowingly included in the background window. Any test based on δ_{11}, however, risks rejecting very large fires since these will increase the 11 μm background variability substantially. For example, over a typical land surface $\delta_{11} \sim 1$ K, whereas for land pixels spanning a large forest fire δ_{11} will routinely exceed 20 K. For this reason, test (2.6) will be employed to disable test (2.5) when the background window appears to contain large fires. This situation is recognized by an elevated value of δ_4'; the presence of background fire

pixels (Section 2.2.2.3) increases this statistic considerably.

2.2.2.5 Tentative fire detection

We are now in the position to tentatively identify pixels containing active fires. For nighttime fires this will in fact be an unambiguous, final identification. For daytime pixels, three additional steps are used to help eliminate false alarms caused by sun-glint, hot desert surfaces, and coasts or shorelines. These will be described in subsequent sections.

A daytime pixel is tentatively classified as a fire pixel if:

{test (2.1) is true}

or

{tests (2.2) - (2.4) are true and [test (2.5) or test (2.6) is true]},

otherwise it is classified as *non-fire*.

A nighttime candidate fire pixel is definitively classified as *fire* if:

{test (2.1) is true}

or

{tests (2.2) - (2.4) are true},

otherwise it is classified as *non-fire*.

For those daytime and nighttime pixels for which the background characterization failed, i.e. an insufficient number of valid neighboring pixels were identified, only test

(2.1) is applied in this step. If not satisfied, the pixel is classified as *unknown*, indicating that the algorithm was not able to unambiguously render a decision.

2.2.2.6 Sun glint rejection

Sun glint over small bodies of water, wet soil, cirrus cloud and, in rare instances, bare soil can cause false alarms. Sun glint is rejected with a scheme based on that of Giglio et al. [2003b], using the angle θ_{g} between vectors pointing in the surface-to-satellite and specular reflection directions, where

$$\cos\theta_{\mathrm{g}} = \cos\theta_{\mathrm{v}}\cos\theta_{\mathrm{s}} - \sin\theta_{\mathrm{v}}\sin\theta_{\mathrm{s}}\cos\phi. \tag{2.7}$$

Here θ_{v} and θ_{s} are the view and solar zenith angles, respectively, and ϕ is the relative azimuth angle. A count is made of adjacent water pixels, i.e. the number of water pixels within the eight pixels surrounding the tentative fire pixel, and is denoted by N_{aw}. The following conditions are then evaluated:

$$\theta_{\mathrm{g}} < 2^{\circ} \tag{2.8}$$

$$\theta_{\mathrm{g}} < 8^{\circ} \quad \text{and} \quad \rho_{0.65} > 0.1 \quad \text{and} \quad \rho_{0.86} > 0.2 \quad \text{and} \quad \rho_{2.1} > 0.12 \tag{2.9}$$

$$\theta_{\mathrm{g}} < 12^{\circ} \quad \text{and} \quad (N_{\mathrm{aw}} + N_{\mathrm{w}}) > 0 \tag{2.10}$$

If one or more of these conditions are satisfied, the fire pixel is rejected as sun glint and classified as *non-fire*, otherwise it is classified as *fire*. Condition (2.8) rejects any fire pixel within the most intense region of glint; detection under this extreme condition is simply too unreliable as the specularly reflected sunlight can elevate T_4 well above

400 K, even over the land surface. Condition (2.9), which is less strict, looks for the consistently elevated reflectances across multiple bands that are characteristic of sun glint. Condition (2.10), which is less strict still, rejects fire pixels occurring near water pixels as too risky a prospect in and near regions of sun glint.

2.2.2.7 Desert boundary rejection

Any surface feature that produces a sharp radiometric transition, or edge, can potentially cause errors of omission or commission for any contextual detection algorithm. In the case of the former, a fire located along a boundary may remain undetected since the edge increases the background variability to the point that relative tests incorporating this variability will fail. The latter case can arise when non-fire pixels along the hotter (and/or more reflective) edge of a boundary are incorrectly rejected as background fires during the background characterization phase. This restricts the sample of valid background pixels to those within the cooler (and perhaps darker) side of the boundary, which skews the background statistics toward cooler values [Giglio et al., 1999, Martín et al., 1999]. In general, it is this second case, namely an error of commission, or “false alarm” along a boundary between hotter and cooler surfaces, that is a much more common problem for contextual fire detection algorithms.

Earlier AVHRR-based contextual algorithms were generally far more susceptible to this problem since they employed thresholds for rejecting background fire pixels that were much lower [e.g., Flasse and Ceccato, 1996, Justice et al., 1996]. Flasse and

Ceccato [1996], for example, rejected background pixels having $T_4 > 311\,\mathrm{K}$ and $\Delta T > 8\,\mathrm{K}$, conditions which are frequently satisfied over ordinary land areas; two examples include dry-season African savannas and most deserts. (For simplicity we have used our 4 μm channel notation in this example, when in fact the corresponding AVHRR channel has a central wavelength of 3.8 μm.) The background-fire rejection thresholds employed in our MODIS algorithm are so high, however, that inadvertent exclusion of non-fire background pixels is almost always restricted to desert areas. For the present MODIS algorithm, therefore, we refer to the problem of eliminating this type of false alarm as *desert boundary rejection*.

To reject false alarms along desert boundaries, one would like the algorithm to identify those cases in which the rejected background fire pixels are ordinary land pixels that happened to satisfy the somewhat arbitrary background-fire rejection thresholds. In this situation, the 4 μm statistics $\overline{T}_4'$ and δ_4' become useful indicators. Over typical daytime desert surfaces, $\overline{T}_4' \approx 335\,\mathrm{K}$ and $\delta_4' \approx 0.5\,\mathrm{K}$. For a background containing energetic fire pixels, however, δ_4' will be much larger (40 K and higher is routine), and $\overline{T}_4'$ will be somewhat larger, perhaps 350 K to 380 K. We therefore incorporate several heuristic tests exploiting these trends as a means of rejecting

daytime false alarms that can arise along desert boundaries. These are:

$$N_{\mathrm{f}} > 0.1\, N_{\mathrm{v}} \tag{2.11}$$

$$N_{\mathrm{f}} \geq 4 \tag{2.12}$$

$$\rho_{0.86} > 0.15 \tag{2.13}$$

$$\overline{T}'_4 < 345\,\mathrm{K} \tag{2.14}$$

$$\delta'_4 < 3\,\mathrm{K} \tag{2.15}$$

$$T_4 < \overline{T}'_4 + 6\,\delta'_4 \tag{2.16}$$

If all conditions are satisfied, the fire pixel is rejected as a hot desert-boundary surface and classified as *non-fire*, otherwise the pixel undergoes a final coastal false alarm test. Conditions (2.11) and (2.12) restrict rejection to cases in which a significant number of background pixels appear to contain background fires, a signature of desert boundary false alarms. Condition (2.13) simply restricts the remaining tests to bright regions characteristic of deserts. Test (2.16), which is satisfied only when a tentative fire pixel stands out very strongly against the rejected *background* fire pixels, isn't a false alarm rejection test *per se*. Rather, it permits detection of gas flares, which are frequently located in desert areas, that would otherwise be excluded due to the uniformity of the landscape.

2.2.2.8 Coastal false alarm rejection

Given the contextual nature of the algorithm, it is important to accurately exclude water and mixed water pixels during the background characterization phase. Such pixels are

usually cooler than adjacent land pixels during the day. Unknowingly including a sufficient number of water and mixed water pixels in the background window can therefore depress $\overline{T_4}$ and cause a coastal false alarm. Also contributing to this phenomenon is the fact that, compared to land, water pixels frequently have lower values of ΔT due to differences in emissivity. Those water and mixed water pixels contaminating the background can, therefore, decrease $\overline{\Delta T}$ and increase the likelihood that a false alarm will occur.

In many respects this is merely a special case of the edge problem discussed in the previous section. For the present algorithm, however, such coastal false alarms can occur almost anywhere and are usually not accompanied by the inadvertent rejection of neighboring non-fire pixels described in the previous section. We therefore treat these types of false alarms separately.

As indicated above, the current MODIS land/sea mask contains significant errors in some areas. The bulk of these errors consist of a 1-5 km discrepancy along coast and shoreline, and small rivers that are missed entirely. In some cases even much larger water bodies are not masked accurately. An example from eastern Africa is shown in Fig. 2.1; here hundreds of pixels are misclassified as land. We have therefore incorporated additional tests to identify cases in which the background window is contaminated with unmasked water pixels. We use a simple test based on the 0.86 and 2.1 μm reflectances, and the Normalized Difference Vegetation Index (NDVI) of the valid background pixels, where $\mathrm{NDVI} = (\rho_{0.86} - \rho_{0.65})/(\rho_{0.86} + \rho_{0.65})$. This particular combination was chosen to reduce the likelihood of confusing cloud shadows and burn

scars, which also have low reflectances, with water.

Valid background pixels having $\rho_{2.1} < 0.05$ and $\rho_{0.86} < 0.15$ and an $\mathrm{NDVI} < 0$ are considered to be unmasked water pixels, i.e. water pixels incorrectly classified as land in the MODIS land/sea mask. The number of such pixels is denoted as N_{uw}. If test (2.1) is not satisfied, and $N_{\mathrm{uw}} > 0$, the tentative fire pixel is rejected and classified as *non-fire*, otherwise it is classified as *fire*. This test will periodically reject smaller valid fires, but the much greater reduction in coastal false alarms generally make these errors of omission tolerable on a global basis. Future planned improvements in the MODIS land/sea mask may ultimately render these tests unnecessary.

2.2.3 Fire detection confidence

A measure of confidence for each detected fire pixel is now also produced based on the approach of Giglio et al. [2003b]. The measure employs T_4, N_{aw}, the number of cloud pixels adjacent to the fire pixel (N_{ac}), and the standardized variables z_4 and $z_{\Delta T}$, defined as

$$z_4 = \frac{T_4 - \overline{T_4}}{\delta_4} \tag{2.17}$$

$$z_{\Delta T} = \frac{\Delta T - \overline{\Delta T}}{\delta_{\Delta T}}. \tag{2.18}$$

These quantities represent the number of absolute deviations that T_4 and T_{11} lie above the background, and are analogous to the more commonly used Z-scores which are calculated using the standard deviation [e.g., Devore, 1987]. We further employ a ramp

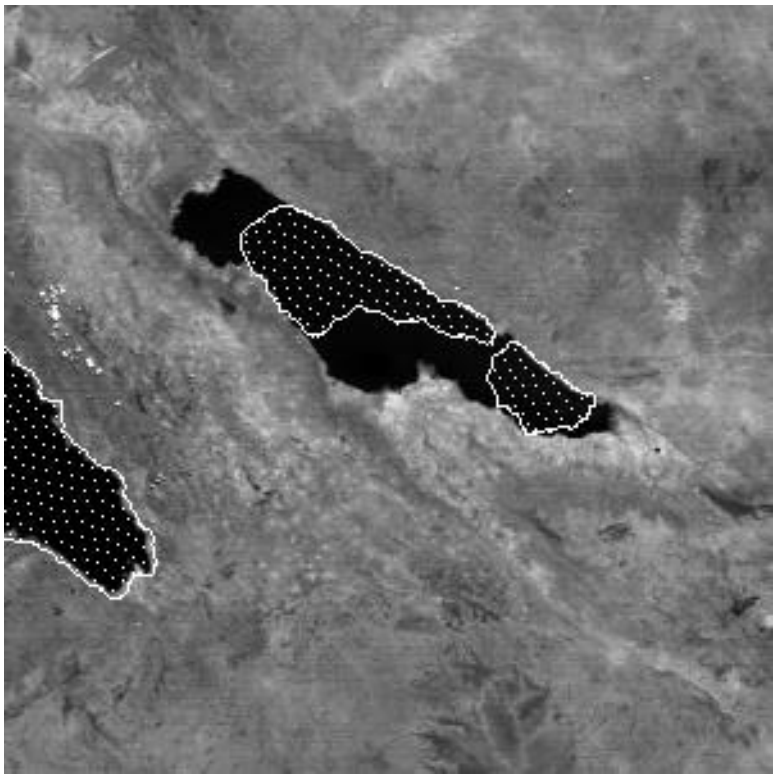

Figure 2.1: Example of the (here incorrect) MODIS water mask (dotted region outlined in white) superimposed on a 1-km aggregated 2.1 μm image of Lake Rukwa in western Tanzania acquired 1 September 2001. The southern tip of Lake Tanganyika appears on the left. Water appears black due to the extreme absorption at this wavelength, and the actual lake boundaries are clearly evident. The image spans an area approximately 300 $\times$ 300 km in size.

function, defined as

$$S(x;\alpha,\beta) = \begin{cases} 0; & x \leq \alpha \\ (x-\alpha)/(\beta-\alpha); & \alpha < x < \beta \\ 1; & x \geq \beta \end{cases} \tag{2.19}$$

The confidence assigned to each fire pixel is composed of a combination of five sub-confidences, labeled C_1 to C_5, each having a range of 0 (lowest confidence) to 1

(highest confidence). For daytime fire pixels these are defined as:

$$C_1 = S(T_4; 310\,\mathrm{K}, 340\,\mathrm{K}) \tag{2.20}$$

$$C_2 = S(z_4; 2.5, 6) \tag{2.21}$$

$$C_3 = S(z_{\Delta T}; 3, 6) \tag{2.22}$$

$$C_4 = 1 - S(N_{\mathrm{ac}}; 0, 6) \tag{2.23}$$

$$C_5 = 1 - S(N_{\mathrm{aw}}; 0, 6) \tag{2.24}$$

For C_1, 310 K represents the minimum brightness temperature required for a pixel to be considered a fire pixel (and is thus less obviously a fire), while, based on operational experience, 340 K represents a typical value for a reasonably obvious fire. For C_2, $z_4 = 2.5$ is the minimum value required of fire pixels by the detection algorithm, whereas $z_4 = 6$ represents a typical value (again based on operational experience) for an unambiguous fire. A similar rationale applies to the definition of C_3. C_4 reduces the detection confidence as the number of adjacent cloud pixels increases, accounting for the fact that fire pixels detected along cloud edges are more likely to suffer from cloud contamination, potentially triggering a false alarm via reflected sunlight. Finally, C_5 reduces the confidence as the number of adjacent water pixels increases, reflecting the greater likelihood that the detected fire pixel is instead a coastal false alarm.

Following Giglio et al. [2003b], the detection confidence C is then defined as the geometric mean of the sub-confidences, i.e.

$$C = \sqrt[5]{C_1 C_2 C_3 C_4 C_5} \tag{2.25}$$

For nighttime fire pixels, the thresholds of C_1 are altered appropriately so that

$$C_1 = S(T_4; 305\,\mathrm{K}, 320\,\mathrm{K}), \tag{2.26}$$

and the cloud- and water-related sub-confidences are not considered. The nighttime detection confidence is therefore simply the geometric mean of C_1, C_2, and C_3.

2.3 Algorithm performance

To date, four principal methods have been used to assess algorithm performance and evaluate the MODIS fire products. First, based on earlier work done by Dowty (1993) and Giglio et al. [1999], simulated MODIS imagery was used to quantify algorithm detection and false alarm rates under a wide range of environmental conditions within different biomes. Second, fire maps generated from high resolution scenes acquired with the Advanced Spaceborne Thermal Emission and Reflection Radiometer (ASTER) have been compared to fires identified by the version 3 and version 4 algorithms. Third, the US Forest Service Fire Sciences Laboratory, which has undertaken an independent validation of the MODIS fire product, has found good correspondence between MODIS fire locations and fire perimeters measured by the Forest Service. Finally, in a more qualitative approach, unambiguous fire pixels and obvious false alarm sources were identified through visual inspection of MODIS 250 m, 500 m, and 1 km imagery, permitting the output from the original and improved algorithms to be compared to “expert”-derived fire masks. Although this approach is,

in general, greatly inferior to the more rigorous approaches mentioned above, it does allow obvious problems to be diagnosed and corrected.

In Section 2.3.1, we will describe our simulation approach, and then discuss the theoretical algorithm performance established by way of the simulation. In Section 2.3.2 we will briefly report on the recent results of Morisette et al. [2005a], who have completed the first of many planned regional MODIS fire validation activities. (Ultimately the MODIS fire products will be validated globally through this process.) Finally, in Section 2.3.3, we will present two examples of obvious cases in which a simple visual analysis and comparison is appropriate.

2.3.1 Simulated fire scenes

2.3.1.1 Method

Simulated 25 km $\times$ 25 km images of MODIS channels 21, 22, and 31 were generated using MODIS-specific modifications of the method used by Giglio et al. [1999] in their evaluation of several AVHRR active fire detection algorithms. The scenes depicted in these images contained idealized fires of various sizes and temperatures in ten different biomes (desert, tropical rainforest, tropical deciduous forest, tropical savanna, temperate deciduous forest, temperate evergreen forest, temperate grassland, boreal evergreen forest, boreal deciduous forest, and tundra). Each biome was characterized by a range of seasonal average surface temperatures and seasonal average emissivities at 1 km spatial resolution. Following Giglio et al. [1999], the 1 km grid cells of each

25 km $\times$ 25 km scene were assigned individual 4 and 11 μm emissivities and a temperature by drawing random samples from normal distributions. In this manner, 100 model surfaces were generated for each biome and season. The MODTRAN atmospheric model (Berk et al., 1989) was used to calculate atmospheric transmission and thermal contributions with an appropriate seasonal tropical, temperate, mid-latitude, or sub-Arctic atmospheric model. A sensor view was then computed taking into account the shape and overlap of the MODIS pixels that fitted inside the 25 km surface grid.

The fire detection algorithm was applied to the synthetic MODIS imagery and, by repeating the process over a range of conditions, the algorithm's performance was characterized statistically in terms of probability of fire detection (P_{d}) and false alarm (P_{f}). Both probabilities are functions of fire temperature and area, solar and viewing geometry, visibility, season, and biome. The presence of fires in the background window also affects P_{d} and P_{f} [Giglio et al., 1999].

None of the reflective channels (channels 1, 2, and 7) are currently modeled in the simulation, so the tests involving these channels were omitted in the application of the algorithm to the simulated data. Since these tests prevent highly reflective and coastal pixels from being classified as fire, the effect of their omission was to potentially overestimate both P_{d} and P_{f}. This approach nevertheless yields useful upper bounds for both probabilities.

2.3.1.2 Results

Because the probability of detection is so strongly dependent upon the temperature and area of the fire being observed, P_{d} is summarized as a *detection matrix* in which fire temperature and area form the rows and columns of the matrix. Such matrices are shown graphically in Fig. 2.2.

Over all biomes considered, the size of the smallest flaming fire having at least a 50% chance of being detected under both ideal daytime and nighttime conditions was $\sim 100\ \mathrm{m}^2$. For the version 3 algorithm, this value was more than two times larger. We define ideal conditions to mean that the fire is observed at or near nadir on a fairly homogeneous surface, the background window contains no fires, and the scene is free of clouds, heavy smoke, and sun glint. For nighttime cases in the coldest biomes, this minimum area tended to be somewhat larger, typically by a factor of two, since the "universal" thresholds used to identify potential fire pixels (Section 2.2.2.1) become much less appropriate under these conditions. Purely smoldering fires generally had to be 10 to 20 times larger to achieve a similar probability of detection.

For the improved algorithm, no false detections were observed under any circumstances. This is in contrast to the version 3 algorithm, which produced false alarms in daytime desert scenes at solar zenith angles below 20°. As mentioned previously, this difference is due to the fact that "risky" absolute threshold tests are not employed in the new algorithm.

An interesting case is the daytime dry-season tropical savanna (Fig. 2.2d). Earlier

work by Giglio et al. [1999] and Giglio et al. [2003b] showed that contextual algorithms using data from either the AVHRR or the VIRS instruments have almost no capability to detect fires at small or even moderate solar zenith angles, e.g. $\theta_{\mathrm{s}} < 40^{\circ}$. For both instruments this is caused by the relatively low saturation ($\sim 325\,\mathrm{K}$) of their mid-infrared channels; fires show little or no contrast against the hot, bright savanna surface which can saturate the mid-infrared channel even in the absence of a fire. The high saturation of the MODIS band 21, however, allows detection to proceed largely unhampered.

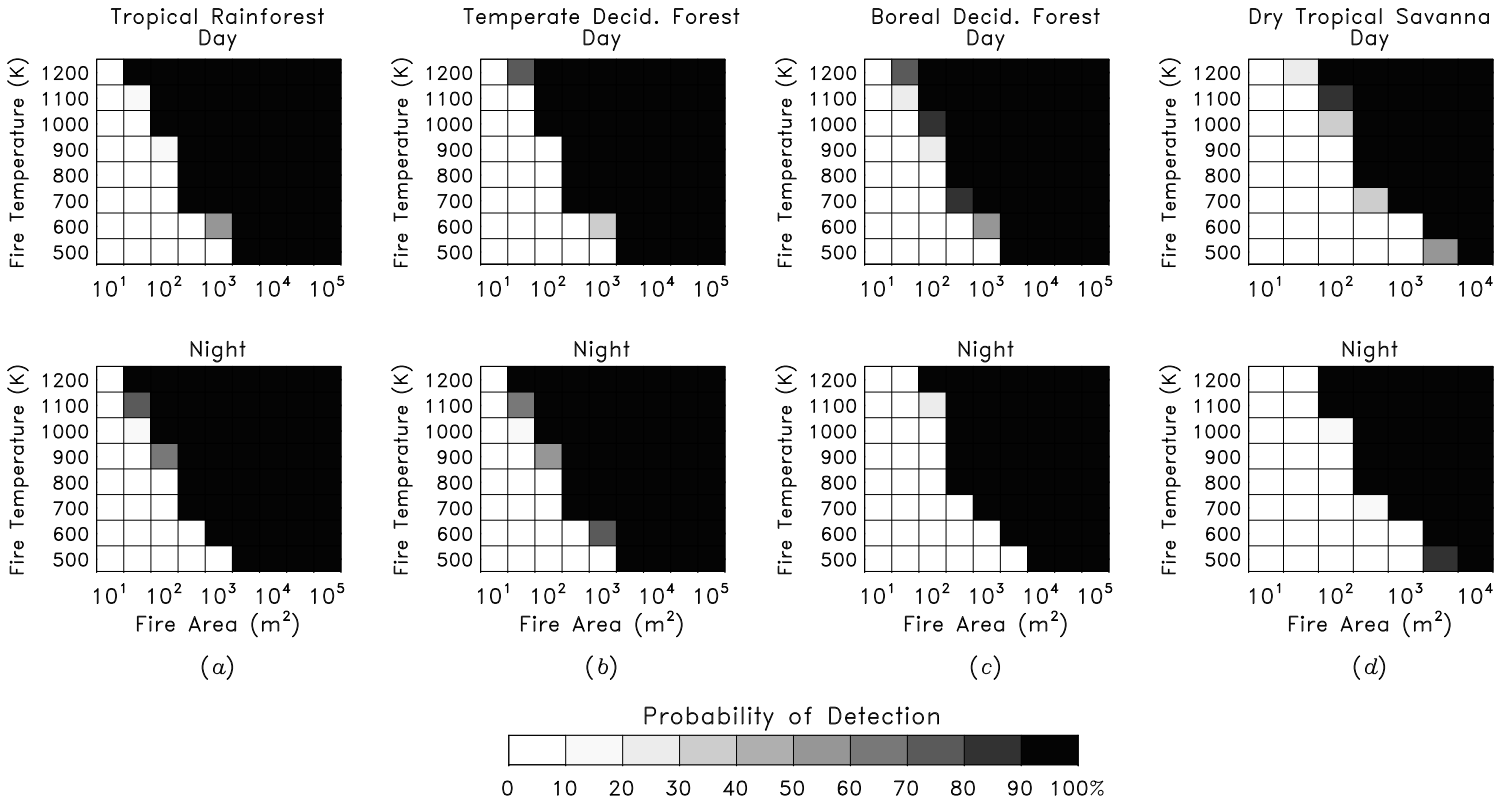

Figure 2.2: Nadir (0° scan angle) daytime (top row) and nighttime (bottom row) detection matrices for four different biomes. *(a)* tropical rainforest with 0° daytime solar zenith angle; *(b)* temperate deciduous forest (summer) with 0° daytime solar zenith angle; *(c)* boreal deciduous forest (summer) with 40° daytime solar zenith angle; *(d)* dry-season tropical savanna with 0° daytime solar zenith angle.

2.3.2 Validation using ASTER scenes

Recent work by Morisette et al. [2005a] used 18 high-resolution ASTER scenes to validate the MODIS fire product in southern Africa. The ASTER instrument is carried on-board the Terra satellite, allowing spatially and temporally coincident observations to be acquired with those of the Terra MODIS. This is ideal for fire validation since active fires can alter a scene significantly in a relatively short period of time (e.g. minutes). Although this first investigation was limited to southern Africa, additional work is ongoing to assess the MODIS fire product globally using a much larger collection of ASTER scenes.

Using the ASTER 2.4 μm channel, which has a spatial resolution of 30 m, Morisette et al. [2005a] were able to map the "true" distribution of active fires in each scene. The 30 m pixels of the resulting ASTER fire masks were then assigned to those MODIS pixels in which they fell; this was accomplished by performing a nearest-neighbor search through all MODIS pixels overlapping the region viewed within the particular ASTER scene. In this manner, ASTER fire masks were prepared for a total of 66,761 MODIS pixels. The probability of detection was then related to the absolute number of ASTER fire pixels (a proxy for instantaneous fire size) within a MODIS pixel. The spatial heterogeneity of the ASTER fire pixels was considered as well. The conditional number of ASTER fire pixels observed in a single MODIS pixel varied from 1 to more than 300. Cases in which no ASTER fire pixels were observed in the corresponding MODIS pixel were also included.

For the time period that was considered (5 August - 6 October 2001), Morisette et al. found that the minimum fire size to achieve $P_{\mathrm{d}} \geq 0.5$ was, in terms of number of ASTER pixels, approximately 30. In contrast, the original detection algorithm required a minimum of 48 ASTER fire pixels regardless of the statistical model. Using the paired ASTER-MODIS data prepared by Morisette et al. [2005a], which were available to us, we performed a subsequent analysis of each algorithm. With respect to false alarms, the algorithms detected 4 (version 3) and 12 (version 4) fire pixels for which the corresponding ASTER fire mask showed zero. We do not, however, consider these to be true false alarms. In each case, ASTER fire pixels were present in at least one adjacent along-scan or along-track MODIS pixel, suggesting that these apparent false alarms might be caused by limitations in the 2 km rectangular model of the MODIS pixel footprint employed by Morisette et al. In addition, Terra MODIS channel 21 exhibits residual instrument artifacts, including minor "blooming" near large or very hot fires [Justice et al., 2002], which could induce false alarms in the immediate vicinity of fires. A better instrument characterization is needed to quantify the extent of these residual artifacts. A third possibility is that the algorithm is simply labeling hot, adjacent, recently-burned patches as fires. The corresponding ASTER scenes showed little or no signs of burn scars in these MODIS pixels, however, and we therefore view this explanation as unlikely.

2.3.3 Visual comparison

An example of the improved ability of the version 4 algorithm to detect small fires is shown in Fig. 2.3. In this example from the northern part of the Democratic Republic of the Congo, the version 4 algorithm detected more than twice the number of fire pixels detected with version 3. A detailed visual analysis of the MODIS visible, mid-infrared, and long wave infrared bands for this scene indicates that the hundreds of additional fire pixels – most of which are accompanied by distinct smoke plumes – are in fact true fires rather than false alarms.

As mentioned in Section 2.1, the original detection algorithm suffered from persistent false detections in deserts and other sparsely vegetated land surfaces. An example over Pakistan is shown in Fig. 2.4. Here the version 3 algorithm yielded nearly 4800 false fire pixels. These pixels were deemed false based on an examination of MODIS 250 m, 500 m, and 1 km imagery and the fact that the large cluster persisted over long periods of time (e.g. weeks). All fire pixels were located in areas of sparsely vegetated soil, and none of the fire pixels have sufficiently high 4 μm brightness temperatures to definitively suggest that true fires might be present. In addition, the top-of-atmosphere visible channel reflectances reveal a complete absence of smoke. This suggests that the majority (if not the entirety) of the fire pixels within this scene are indeed false alarms. The corresponding output from the version 4 algorithm, which yielded no false detections, is shown for comparison. Although the difference in algorithm output is enormous in this particular example, the average reduction in false

alarm rate at the global scale is generally not this dramatic. Test runs using almost a year of MODIS data indicated that the number of obvious false fire pixels generated with the version 4 algorithm is generally 10 to 100 times smaller than the number generated with version 3.

Figure 2.3: Example of small fires detected by original (version 3) algorithm (*top*) and version 4 algorithm described in this chapter (*bottom*) acquired over the northern portion of the Democratic Republic of the Congo at 09:30 on 16 December 2000. Fire pixels are shown in black, rivers in dark grey, clouds in light gray, and non-fire areas in white. The original algorithm detected 267 fire pixels, whereas the new algorithm detected 568. The image spans a region approximately 400 km along each side. Note that for the version 3 algorithm, shorelines were expanded to reduce coastal false alarms; this step is unnecessary for the improved detection algorithm.

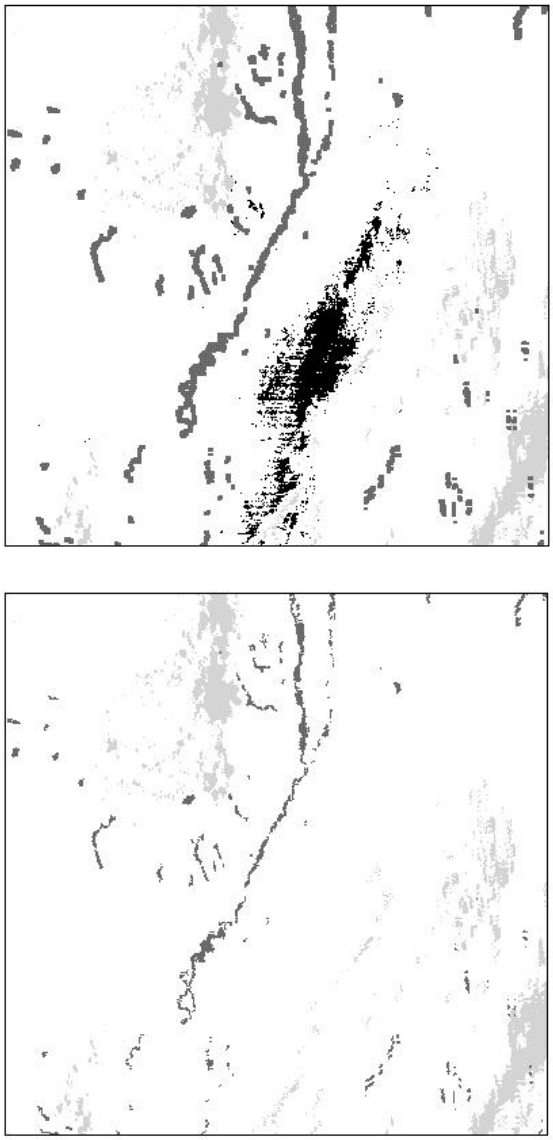

Figure 2.4: Example of blatant false fire pixels detected by original (version 3) algorithm (*top*) in Pakistan on 13 June 2001, 06:30 UTC. Version 4 algorithm output is shown in the bottom figure. Fire pixels are shown in black, rivers in dark grey, clouds in light gray, and non-fire areas in white. Version 3 algorithm detected 4759 false fire pixels; version 4 algorithm detected zero. The image spans a region approximately 400 km along each side.

2.4 Conclusion

We have described an improved contextual active fire detection algorithm for the MODIS instrument. This algorithm, known as version 4, offers considerable improvement over previous versions. The version 4 algorithm is run as part of the MODIS land forward processing stream, as well as within the MODIS Rapid Response System (Justice et al., 2002b) It is also being run as part of the MODIS "Collection 4" reprocessing stream to reprocess all MODIS data starting from March 2000, the beginning of the Terra MODIS data archive. It should be noted that the Terra instrument performance prior to November 2000 render the active fire data for this period of limited utility. Consistent time series of fire data from MODIS should be started no earlier than November 2000. The same version 4 algorithm applies to both Terra and Aqua MODIS data.

Although additional algorithm enhancements may be made in the future based on validation results or changes in instrument performance, the immediate focus must now be given to improving the ancillary water mask used in the algorithm. This is currently the greatest source of error in the version 4 product. Commission errors in the current water mask cause some persistent false alarms along the banks of (and islands within) some rivers. Improvements in the land-water mask derived either directly from MODIS, for example by using the 250 m bands, or from an external data source, such as the emerging data sets from the Shuttle Radar Topography Mission, can be envisioned.

Ongoing efforts are being made to assess the detection algorithm performance and determine product accuracy under different conditions. For the Terra fire product, validation with ASTER is actively being pursued and globally representative validation is underway. Improvements are also being made to the fire simulation to model all bands and add greater realism to the simulation data set. There is also a need to better model some of the idiosyncrasies of the MODIS band 21 and 22 detectors.

Iterative improvements to the MODIS land algorithms, followed by strategic data reprocessing will lead to the long term science quality data products needed for global change research. During the first two years of MODIS data we have gained considerable experience and understanding of the fire algorithm and the Terra MODIS instrument performance, which has resulted in the significant improvements to the algorithm presented in this chapter.

Chapter 3

Active Fire Detection with the Advanced Spaceborne Thermal Emission and Reflection Radiometer

3.1 Introduction

At present a number of satellite-based active fire, or “hot spot”, data products are available for operational and experimental use. The number of sensors from which these data sets are derived has grown considerably over the past decade, and now includes the Advanced Very High Resolution Radiometer (AVHRR), the Moderate Resolution Imaging Spectroradiometer (MODIS), the Along-Track Scanning Radiometer (ATSR) and Advanced Along-Track Scanning Radiometer (AATSR), the Visible and Infrared Scanner (VIRS), the Geostationary Operational Environmental Satellite (GOES) Imager, and the Operational Linescan System (OLS) [Arino and Rosaz, 1999, Elvidge et al., 1996, Giglio et al., 2000, Justice et al., 1996, 2002, Prins

et al., 2001, Stroppiana et al., 2000b] While a variety of intercomparisons between satellite-based active fire data sets (or between the fire detection approach associated with each) have been performed [Li et al., 2001, Ichoku et al., 2003], there has been little rigorous product validation. The reason for this, of course, arises from the dynamic nature of fire and the short time scales over which it interacts with, and moves across, the landscape. Continued interest exists, therefore, in using high resolution sensors on board aircraft or satellites to provide spatially and temporally coincident fire imagery. The resulting fire "snapshots" could then be used to derive detailed, instantaneous maps of fire extent (and perhaps properties) to support validation.

A high-resolution sensor beginning to facilitate fire validation is the Advanced Spaceborne Thermal Emission and Reflection Radiometer (ASTER), a 14-channel imaging radiometer on board NASA's Terra satellite. Since ASTER co-resides with the Terra MODIS instrument, high resolution ASTER fire masks have become an important tool in the ongoing validation of the 1-km Terra MODIS active fire products initiated by Morisette et al. [2005a] and Morisette et al. [2005b]. Since manual production of fire masks is time consuming, and simple fixed threshold methods do not scale well (both spatially and temporally), a consistent, automated source of ASTER fire masks is desirable. Here, we present a fire detection algorithm that uses ASTER observations to provide binary "yes/no" fire masks at 30-m spatial resolution.

The use of ASTER fire masks for the validation of other fire monitoring sensors is also possible provided the sensor resides on a satellite having at least an occasional overpass coincident with Terra. Sensors meeting this criterion include the Tropical

Rainfall Measuring Mission (TRMM) VIRS, the GOES Imager, and the Meteosat-8 Spinning Enhanced Visible and Infrared Imager (SEVIRI).

3.2 The ASTER Instrument

The ASTER is a 14-channel imaging radiometer with separate visible and near-infrared (VNIR), short wave infrared (SWIR), and thermal infrared (TIR) optical subsystems [Yamaguchi et al., 1998]. The individual subsystems contain four (VNIR), six (SWIR), and five (TIR) spectral bands at 15, 30, and 90 m spatial resolution, respectively. The ASTER band numbering and spectral locations are listed in Table 3.1. The VNIR and SWIR bands have three and four individually-selectable gain settings, respectively, referred to as *high*, *normal*, *low-1*, and *low-2* (SWIR only). The imaging swath for all bands spans 60 km. Due to various hardware, power, and data storage and download rate constraints, ASTER does not continuously acquire data, but is instead operated on a prioritized acquisition schedule [Yamaguchi et al., 1998].

3.3 Data

For this study we used 196 radiometrically calibrated and geometrically coregistered Level 1B ASTER scenes acquired between early 2001 and late 2003 for algorithm testing and evaluation. Scene locations and acquisition dates were selected based on current knowledge of the global distribution of fire activity. The locations of all scenes

Table 3.1: ASTER channel characteristics.

Band Number	Central Wavelength (μm)	Spatial Resolution (m)
1	0.56	15
2	0.66	15
3N	0.82	15
3B	0.82	15
4	1.65	30
5	2.17	30
6	2.21	30
7	2.26	30
8	2.33	30
9	2.40	30
10	8.30	90
11	8.65	90
12	9.10	90
13	10.60	90
14	11.30	90

are shown in Fig. 3.1.

3.4 Fire Detection

3.4.1 Band Selection

Satellite-based fire detection has traditionally relied upon bands located near 4 μm to exploit the high levels of black-body radiation emitted at typical fire temperatures in this region of the electromagnetic spectrum. This region is, in fact, near-optimal for satellite-based fire detection in daytime imagery. This can be seen by considering the ratio R of black-body radiation emitted by a fire (L_{fire}) to the radiance of the ambient

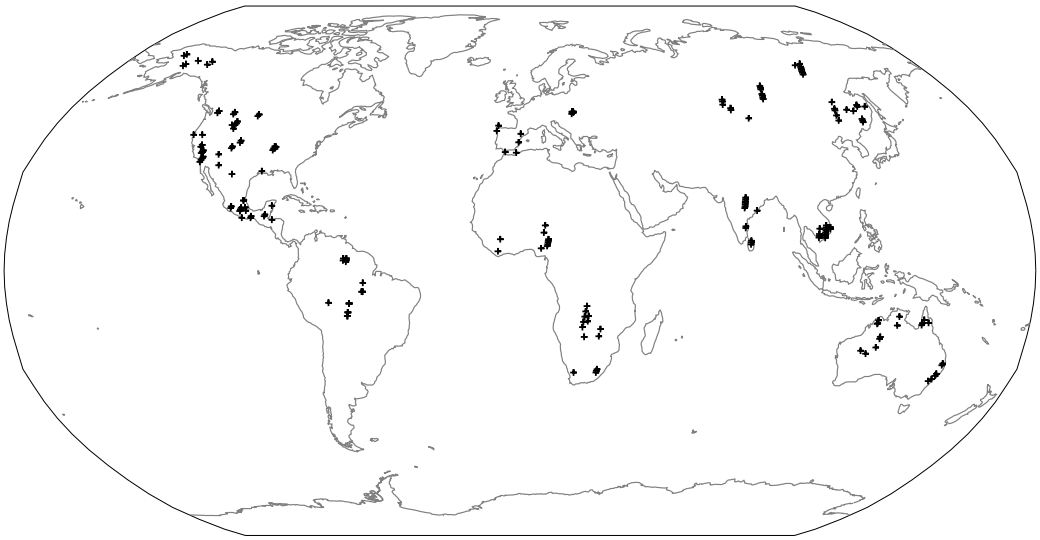

Figure 3.1: Locations of the 196 ASTER scenes used in this study.

non-fire land surface (L_{land}):

$$R = L_{\mathrm{fire}}/L_{\mathrm{land}} \tag{3.1}$$

The land radiance is composed of reflected solar radiation and thermal black-body radiation. For now we consider a simplified case of a Lambertian grey-body surface, unit fire emissivity, and no atmosphere. With the Sun located directly overhead, the ratio in Eq. (3.1) is given by

$$R(\lambda) = \frac{B(\lambda, T_{\mathrm{fire}})}{\rho B(\lambda, T_{\mathrm{sun}})\Omega_{\mathrm{sun}}/\pi + (1-\rho)B(\lambda, T_{\mathrm{land}})}, \tag{3.2}$$

where $B(\lambda, T)$ is the Planck function, ρ is the land surface reflectance, T_{land} is the land surface temperature, and Ω_{sun} is the solid angle subtended by the Sun. The Planck function, which describes the spectral radiance emitted at wavelength λ by a

black-body at temperature T, is given by

$$B(\lambda, T) = c_1 \lambda^{-5} \left[\exp\left(\frac{c_2}{\lambda T} \right) - 1 \right]^{-1}, \tag{3.3}$$

where c_1 and c_2 are constants. In Fig. 3.2, the ratio $R(\lambda)$ is shown for representative flaming ($\sim$1000 K) and smoldering ($\sim$600 K) fires. Sensitivity peaks near 4 μm for both cases.

Among the most egregious of the simplifications we have made is the assumption of a grey body surface. In reality, of course, surface reflectance varies considerably with wavelength, and the constant ρ appearing in Eq. (3.2) should be replaced with the function $\rho(\lambda)$. If we were to substitute the reflectance spectrum of most natural terrestrial components into Eq. (3.2), the general shape of the curve in Fig. 3.2 would still resemble that of the ideal case, and peak sensitivity would remain near 4 μm. In contrast, including the atmosphere introduces severe constraints on band selection that arise from the absorption characteristics of different atmospheric constituents (Fig. 3.3). Water vapor absorption, for example, renders the spectral region from 5.5 to 7 μm completely useless for observing the terrestrial surface. Conveniently, an atmospheric window exists between 3.6 and 4.1 μm, leaving a band located at approximately 4 μm optimal for daytime fire detection. The locations of atmospheric windows are indicated in Fig. 3.2 as the solid portions of the curves; the broken portions indicate those spectral regions not usable for surface observation.

Since ASTER lacks a 4 μm band, the next best choice would normally be band 9 (2.40 μm). This was the band used by Morisette et al. [2005a] to validate the MODIS

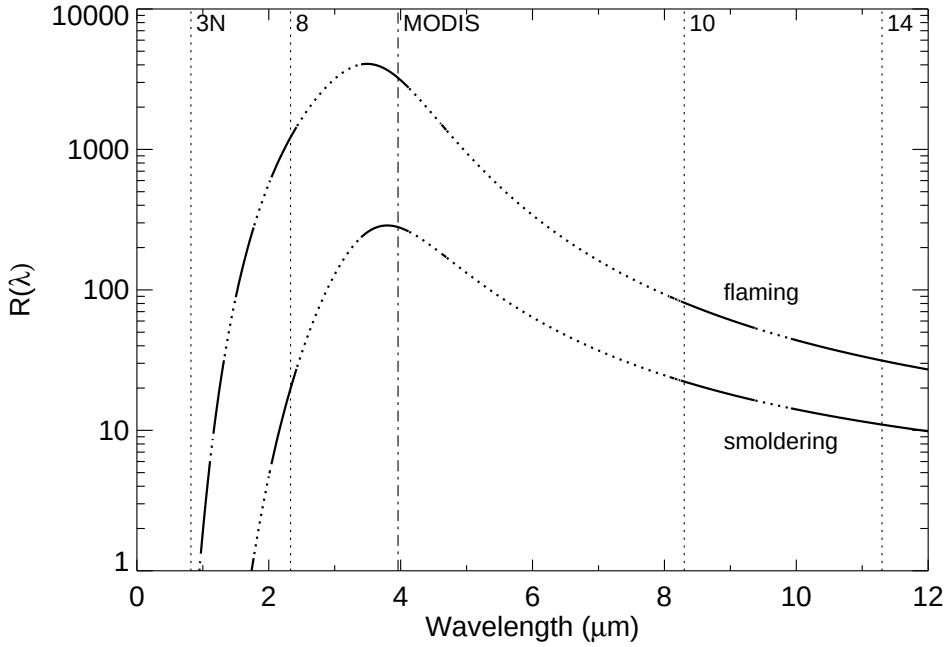

Figure 3.2: Ratio R of typical fire radiance to typical land surface radiance, as a function of wavelength, for 1000 K flaming and 600 K smoldering fires. The solid portions of both curves denote the locations of atmospheric windows. This is a highly idealized case with the land surface assumed to be a grey body of 15% reflectance, and no atmospheric extinction. Vertical dotted lines indicate locations of ASTER bands 3N, 8, 10, and 14. Vertical dot-dashed line indicates location of MODIS middle infrared fire bands for comparison.

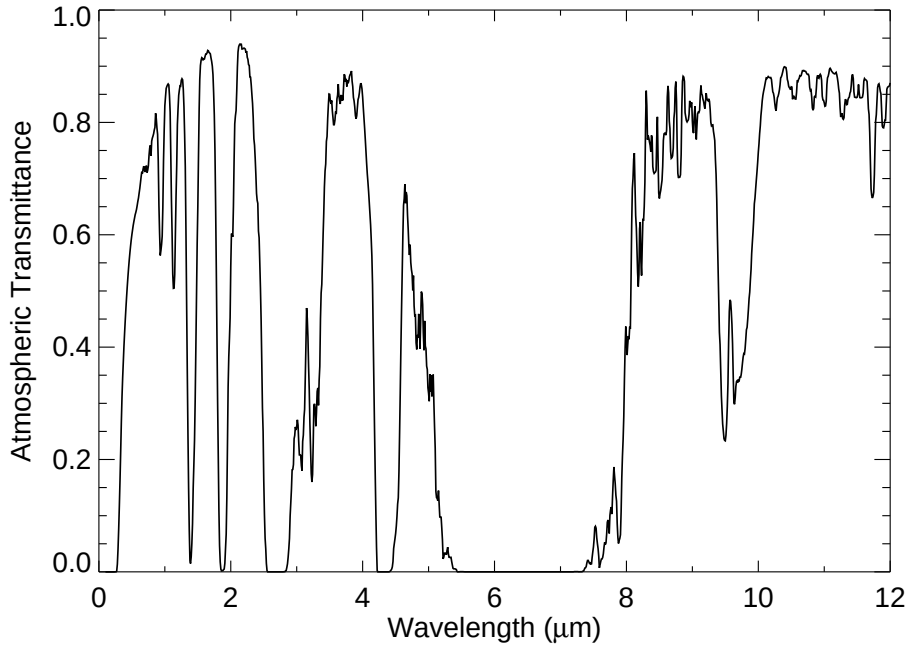

Figure 3.3: Upward atmospheric transmittance as function of wavelength, computed using MODTRAN 4 atmospheric model for the U.S. 1976 standard atmosphere (rural 23 km visibility).

fire product in southern Africa, where it was found to work well. Active fires were detected within ASTER scenes by means of a fixed 6.33 $\mathrm{W\,m^{-2}\,sr^{-1}\,\mu m^{-1}}$ threshold criterion applied to band 9 radiance imagery. The authors include a qualitative discussion on the merits of using this particular band in the context of fire detection. There are several issues, however, which complicate the use of band 9 for routine use. In general, all of the ASTER SWIR bands, particularly band 9, can exhibit blooming when "pushed" to the point of saturation, making it difficult to demarcate actual fire front boundaries. Second, a small number of "dead" pixels having a digital count near zero tend to occur along an edge (or sometimes within) clusters of saturated SWIR pixels, and occurs most often in band 9. These issues were first noted by Morisette et al. [2005a]. A third complication is that crosstalk from band 4 spills primarily into bands 5 and 9. While the magnitude of this effect is small [Iwasaki et al., 2002], it is possible that fire boundaries might bleed into neighboring non-fire pixels, particularly near bodies of water. Finally, we observed that, for the ASTER scenes used in this study, band 9 appears to be affected by a major signal bias when acquired at the lowest gain setting (*low-2*). In terms of reflectance, the magnitude of this apparent bias varies between 0.3 and 0.7. At present we do not know whether this problem is confined to band 9, or affects all of the SWIR bands since, of the scenes used in this study, no other bands were acquired at the *low-2* gain setting.

Using Fig. 3.2 it might be argued that band 10 (8.30 μm) would actually be a superior choice for detecting smoldering fires. While true for pixels that are comparable in size to ASTER's 30-m SWIR bands, the lower 90-m spatial resolution

of the TIR bands leaves them significantly less sensitive to fires. A good example of this may be found in Morisette et al. [2005a].

For the reasons discussed above we have selected band 8 (2.33 μm) as the most useful for fire detection. Our approach for daytime scenes in fact uses two ASTER bands, one of which is sensitive to the black-body radiation emitted by fires (band 8), and another which is insensitive to such radiation but that provides a highly-correlated reflectance over "normal" (non-fire) components of terrestrial scenes, which includes soil, vegetation, clouds, and urban areas. The only viable candidate is band 3N (0.82 μm) which, of the four VNIR bands, is the least susceptible to scattering by smoke and other aerosols. Fig. 3.4 shows a false color band 1, band 3N, and band 8 image of an active fire in eastern Cambodia. In this color scheme active fires appear bright red, burn scars appear brown, clouds appear white, and cloud shadows appear black. In Fig. 3.5 we show the relationship between band 3N and band 8 reflectance for the same scene. Several broad features are evident. First, there is a central cluster in which the band 3N and band 8 reflectances are largely uncorrelated but well constrained. This corresponds to vegetation, some soils, and burn scars. Next, there is an elongated cluster in which the reflectances are very highly correlated, corresponding to clouds and, to a lesser extent, brighter soils. The third, vertically oriented cluster corresponds to pixels containing active fires. The apparent band 8 reflectance of these pixels is anomalously high due to the substantial emissive SWIR contribution from combustion. Overall, the reflectances of non-fire pixels are linearly related, and this relationship is sufficiently strong that the ratio of band 8 reflectance to band 3N

reflectance is nearly constant (Fig. 3.6). We will exploit this characteristic in developing a daytime fire detection algorithm for ASTER. Nighttime scenes, being devoid of reflected sunlight (barring a very small contribution from the Moon), are much less ambiguous, and active fires can be identified with thresholds applied to band 8 imagery.

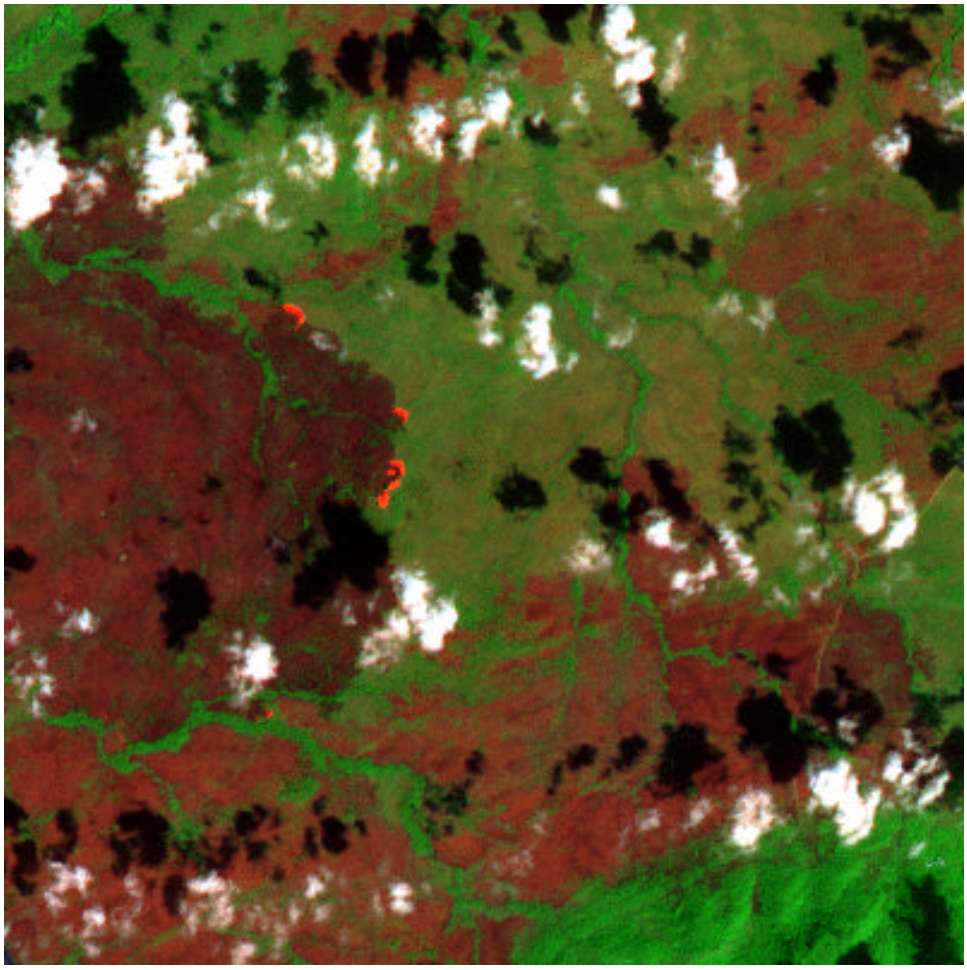

Figure 3.4: False color ASTER image of an active fire in eastern Cambodia, acquired 15 January 2003, 03:31 UTC, with band 8 shown as red, band 3N shown as green, and band 1 shown as blue. With this color scheme active fires appear bright red, burn scars appear brown, clouds appear white, and cloud shadows appear black. Approximate location of this fire is 13.2°N, 107.7°E. Image spans an area 12 km × 12 km in size.

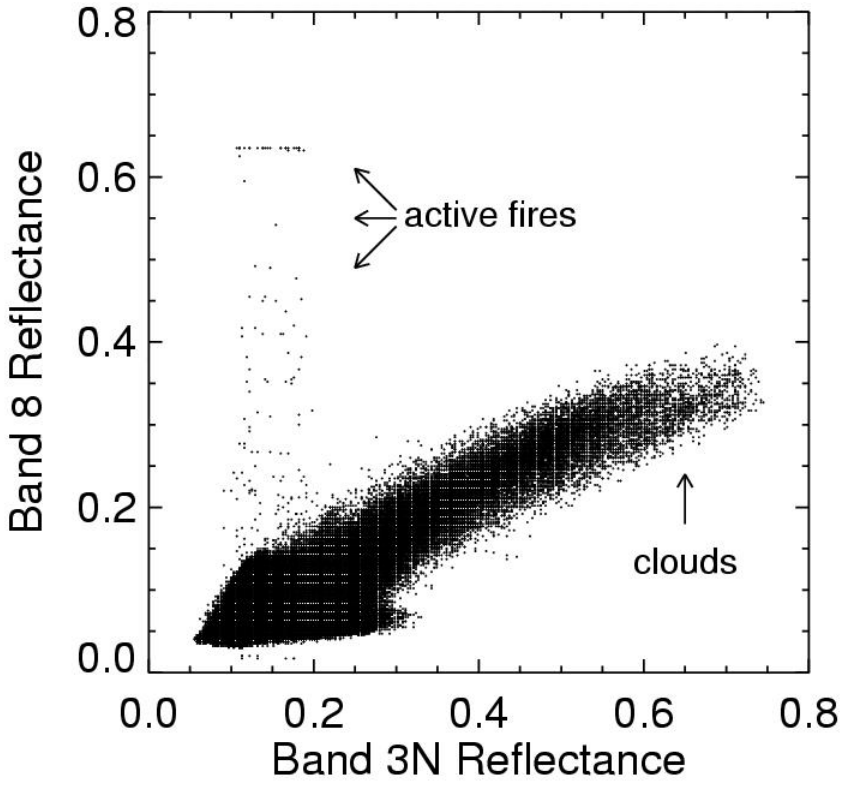

Figure 3.5: Relationship between band 3N and band 8 top-of-atmosphere reflectance for all pixels comprising the scene shown in Fig. 3.4. For this particular scene, band 8 saturates at a reflectance of about 0.64.

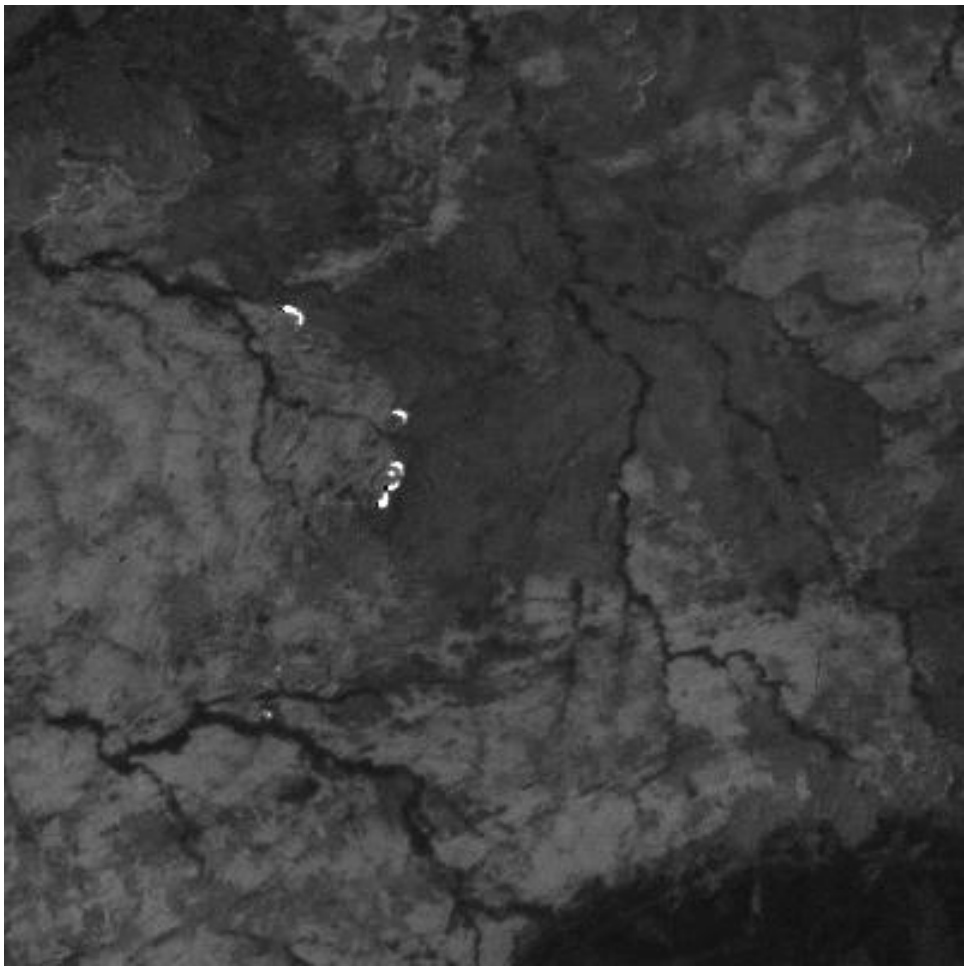

Figure 3.6: Ratio of ASTER band 8 and band 3N for scene in Fig. 3.4.

3.4.2 Detection Algorithm

For daytime scenes we use top-of-atmosphere reflectances computed for ASTER bands 3N and 8, denoted by ρ_3 and ρ_8, respectively. To produce compatible spatial resolutions, band 3N pixels are aggregated to 30 m spatial resolution by averaging. For nighttime scenes our approach requires the ASTER band 8 top-of-atmosphere radiance (L_8) only.

3.4.2.1 Daytime algorithm

In the following discussion we refer to the ratio (r) and the difference ($\Delta\rho$) of the band 3N and band 8 reflectances, where $r = \rho_8/\rho_3$ and $\Delta\rho = \rho_8 - \rho_3$.

Step 1: Mask obvious water pixels. Because our approach includes a contextual component in which local spatial statistics are computed, it is desirable to exclude water pixels during this process. Since ancillary water masks are currently unavailable at the scale of an ASTER pixel, we apply a simple band 8 threshold test on a per-pixel basis: all pixels for which $\rho_8 < 0.04$ are flagged as water and are excluded from further processing. While this value provided reasonably good identification of water pixels in our test scenes, it may need to be adjusted regionally.

Step 2: Identify obvious fire pixels. Pixels for which $r > 2$ and $\Delta\rho > 0.2$ are considered to be obvious fire pixels and are immediately flagged as containing an active fire.

Step 3: Identify candidate fire pixels. Pixels for which $r > 1$ and $\Delta\rho > 0.1$ that were not flagged as obvious fire pixels in the previous step are flagged as candidate fire pixels.

Step 4: Background characterization. Neighboring pixels in a square window centered on the candidate fire pixel are used to estimate the mean non-fire "background" values of the reflectance ratio and band 8 reflectance. Pixels identified as obvious fire pixels in Step 2 are excluded from this window. Unlike the variable background windows used in contextual algorithms developed for coarser resolution ($\sim$1-km) sensors [e.g., Flasse and Ceccato, 1996, Giglio et al., 1999], the size of the background window is fixed at 61 $\times$ 61 pixels (1830 m $\times$ 1830 m) in size. This scale, which was determined empirically, is reasonable given the much higher spatial resolution of ASTER. For small and moderate size fires, the majority of the 30-m pixels within a window of this size will be fire-free and usable for background characterization. On the other hand, the problematic case of the background window spanning a very large fire, and consequently leaving an insufficient number of non-fire pixels available for background characterization, will virtually never occur: most pixels within a very large fire will have already been identified as obvious fire pixels in Step 2, thus obviating the need for background characterization to be performed.

Four statistics are computed for pixels within the background window: the mean ($\overline{r}$) and standard deviation (σ_r) of the reflectance ratio, and the mean ($\overline{\rho_8}$) and standard deviation (σ_8) of the band 8 reflectance.

Step 5: Contextual tests. For all candidate fire pixels evaluate the conditions

$$r > \overline{r} + \max(3\sigma_r,\, 0.5) \tag{3.4}$$

$$\rho_8 > \overline{\rho_8} + \max(3\sigma_8,\, 0.05) \tag{3.5}$$

are evaluated, where $\max(u, v)$ denotes the larger of u and v. If both conditions are satisfied, the pixel is flagged as containing an active fire. Condition (3.4) is used to identify pixels exhibiting the anomalously high SWIR to VNIR ratio expected when an active fire is present in an ASTER pixel. Condition (3.5) is used to identify pixels having the anomalously high apparent SWIR reflectance caused by the presence of fires. It also prevents false alarms in pixels having an exceptionally low near-infrared reflectance but otherwise modest SWIR reflectance. This condition can occur, for example, within shallow, silt-laden water bodies. The minimum difference thresholds of 0.5 and 0.05 in (3.4) and (3.5), respectively, prevent false alarms in unusually homogeneous regions.

3.4.2.2 Nighttime algorithm

The simplicity of nighttime scenes permit the use of a single band 8 radiance threshold. Pixels for which $L_8 > 1\,\mathrm{Wm^{-2}sr^{-1}}\mu\mathrm{m}^{-1}$ are classified as fire pixels. This particular threshold value is roughly a factor of ten larger than the typical nighttime land surface radiance at 2.33 μm.

3.4.3 Expected Performance

Although the daytime detection algorithm does not require saturation of band 8 to detect a fire, saturation is nevertheless a useful criterion for gauging the approximate fire detection capability of the instrument. As will be shown in Section 3.6, the majority of detected fires saturate band 8. Figure 3.7 shows the minimum fire size that will reach the band-8 saturation level of 10.55 $\mathrm{Wm^{-2}sr^{-1}\mu m^{-1}}$ (gain setting *normal*), indicating that ASTER can in principle detect flaming fires $\sim$1 $\mathrm{m^2}$ in size, and smoldering fires approximately 100 times larger.

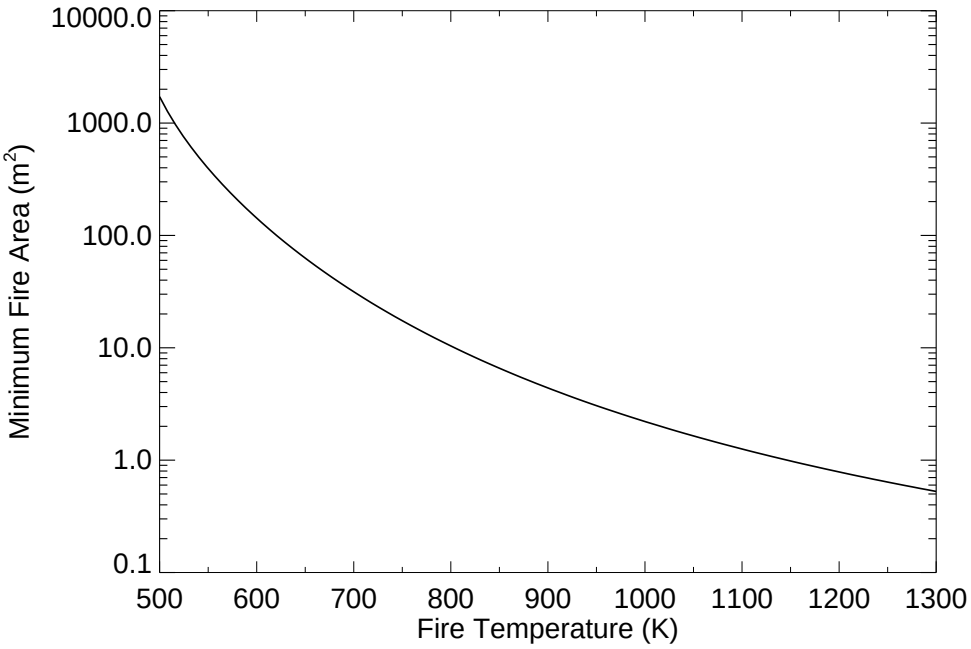

Figure 3.7: Minimum fire size required to saturate ASTER band 8 (at normal gain) as a function of fire temperature under typical daytime conditions. A surface reflectance of 15% was assumed.

3.5 Algorithm Evaluation

Of the 196 ASTER scenes used in this study, 96 were used for testing during algorithm development and the remaining 100 were set aside for algorithm evaluation. The evaluation scenes were partitioned into nine different regions (Africa, Asia, Australia, India, Europe, Mexico, Russia, South America, and USA/Canada) and are listed in Table 3.2.

For each evaluation scene, manually identified fire pixels were stored in an "expert" fire mask. These masks were then compared to the fire masks generated by the detection algorithm, allowing the construction of error matrices which summarized algorithm performance for each region.[1] The elements of the error matrix are shown in Table 3.3.

[1]Error matrices are also referred to as *contingency tables*, *truth tables*, and *confusion matrices* in the literature.

Table 3.2: ASTER scenes used in algorithm evaluation.

Scene Number	Acquistition Date (UTC)	Center Latitude (°)	Center Longitude (°)	Region
1	2003-01-30 11:04	9.6	-6.9	Africa
2	2003-01-30 11:05	5.9	-7.7	
3	2003-01-31 10:07	13.8	8.9	
4	2003-01-31 10:07	11.6	8.4	
5	2003-01-31 10:09	6.8	7.4	
6	2002-12-16 09:56	9.6	10.0	
7	2002-12-16 09:56	9.1	9.9	
8	2002-12-16 09:56	8.6	9.8	
9	2002-12-16 09:56	8.0	9.7	
10	2002-12-16 09:57	7.5	9.5	
11	2003-09-01 08:51	-10.8	23.5	
12	2003-09-03 08:40	-13.8	24.2	
13	2003-09-03 08:42	-20.2	22.8	
14	2003-09-05 08:29	-17.8	28.5	
15	2003-09-05 08:29	-20.0	28.0	
16	2003-01-26 08:21	-30.0	27.9	
17	2003-01-26 08:22	-30.5	27.7	
18	2003-01-26 08:22	-31.0	27.6	
19	2002-11-26 08:53	-31.0	19.5	
20	2003-01-06 03:37	12.8	105.4	Southeast Asia
21	2003-01-06 03:38	11.2	105.1	
22	2003-01-06 03:38	10.6	105.0	
23	2003-01-15 03:32	10.0	107.0	
24	2003-01-06 03:38	10.1	104.8	
25	2003-01-15 03:31	13.8	107.8	
26	2003-01-15 03:31	13.2	107.7	
27	2003-01-15 03:32	10.6	107.1	
28	2003-01-24 03:25	13.2	109.2	
29	2003-01-24 03:25	12.7	109.1	
30	2003-05-07 01:59	-15.1	126.4	Australia
31	2003-05-07 02:00	-16.2	126.1	
32	2004-09-30 02:01	-24.4	122.0	
33	2004-10-03 00:51	-16.0	142.0	
34	2000-09-23 00:15	-32.0	151.6	
35	2002-10-22 00:08	-33.6	150.1	
36	2002-10-31 00:02	-33.0	151.0	
37	2002-12-18 00:01	-28.3	152.6	
38	2001-12-27 02:05	-25.3	124.0	

continued...

Table 3.2: continued...

Scene Number	Acquistition Date (UTC)	Center Latitude (°)	Center Longitude (°)	Region
39	2003-06-03 09:38	48.6	20.7	Europe
40	2005-09-03 09:43	48.4	20.7	
41	2005-09-03 09:43	47.9	20.5	
42	2002-02-15 09:45	48.3	21.2	
43	2002-07-02 09:39	48.6	21.2	
44	2002-09-20 11:21	36.1	-5.5	
45	2002-09-09 11:38	44.2	-8.3	
46	2002-09-09 11:38	42.6	-8.9	
47	2002-09-24 10:55	41.7	0.3	
48	2002-09-24 10:56	39.1	-0.5	
49	2002-09-24 10:57	35.9	-1.4	
50	2003-02-23 05:16	13.5	79.5	India
51	2003-02-23 05:16	13.0	79.4	
52	2003-02-25 05:02	18.3	84.0	
53	2003-03-04 05:11	9.1	81.1	
54	2003-03-04 05:11	8.6	81.0	
55	2003-03-04 05:11	8.0	80.9	
56	2003-03-09 05:26	21.2	80.2	
57	2003-03-09 05:26	20.2	80.0	
58	2003-03-09 05:27	19.6	79.9	
59	2003-03-09 05:27	19.1	79.7	
60	2004-04-17 17:16	21.4	-98.4	Mexico
61	2004-04-20 17:45	29.4	-104.2	
62	2004-05-08 17:35	19.1	-102.6	
63	2004-05-12 17:12	16.1	-98.2	
64	2004-05-14 16:59	16.6	-95.0	
65	2004-05-14 16:59	16.1	-95.1	
66	2004-05-18 16:33	19.8	-88.1	
67	2004-05-25 16:40	17.1	-90.2	
68	2004-05-25 16:41	16.6	-90.4	
69	2004-05-27 16:28	15.5	-87.5	
70	2002-04-26 05:49	52.4	82.7	Russia
71	2002-04-26 05:49	51.8	82.5	
72	2002-05-09 02:01	50.7	136.0	
73	2002-05-09 02:01	50.2	135.8	
74	2002-07-23 03:18	63.2	126.5	
75	2002-07-23 03:18	62.7	126.1	
76	2002-07-23 03:18	62.2	125.6	

continued...

Table 3.2: continued...

Scene Number	Acquistition Date (UTC)	Center Latitude (°)	Center Longitude (°)	Region
77	2002-07-23 03:19	60.6	124.4	Russia (cont.)
78	2002-08-01 03:12	63.7	124.7	
79	2001-08-05 05:08	46.5	89.9	
80	2004-02-07 14:41	3.7	-61.7	South America
81	2004-02-07 14:41	3.1	-61.8	
82	2003-08-29 14:56	-9.8	-67.1	
83	2003-10-08 14:05	-3.7	-54.9	
84	2003-01-28 14:35	3.7	-60.6	
85	2003-01-28 14:35	3.2	-60.7	
86	2003-01-28 14:36	2.7	-60.8	
87	2003-09-06 14:05	-6.4	-55.0	
88	2003-09-20 14:19	-10.0	-59.9	
89	2003-09-22 14:06	-6.4	-55.4	
90	2004-06-21 21:05	64.9	-141.1	USA/Canada
91	2004-06-21 21:05	63.9	-142.0	
92	2004-07-17 21:42	65.2	-148.1	
93	2003-09-22 18:50	36.6	-118.0	
94	2003-09-22 18:51	36.1	-118.1	
95	2003-09-29 18:56	38.3	-119.4	
96	2003-09-29 18:56	37.7	-119.6	
97	2003-10-26 18:39	34.7	-117.1	
98	2003-10-26 18:39	34.2	-117.2	
99	2003-10-26 18:39	33.7	-117.4	
100	2003-10-26 18:39	33.1	-117.5	

Table 3.3: Elements of error matrix used to calculate accuracy measures. The first subscript denotes the class assigned to a pixel by the algorithm, and the second denotes the class assigned by the expert.

	Expert Class	
Algorithm Class	Fire	Non-fire
Fire	M_{ff}	M_{fn}
Non-fire	M_{nf}	M_{nn}

A common measure of accuracy known as the *overall accuracy* is simply the ratio of the number of correctly classified pixels to the total number of pixels evaluated. In terms of the elements of the error matrix, the overall accuracy A is given by

$$A = \frac{M_{\mathrm{ff}} + M_{\mathrm{nn}}}{M_{\mathrm{ff}} + M_{\mathrm{fn}} + M_{\mathrm{nf}} + M_{\mathrm{nn}}}. \tag{3.6}$$

In the present work this metric is not particularly useful since the number of correctly classified non-fire pixels (M_{nn}) will generally dwarf all other elements of the error matrix. Eq. (3.6) will consequently nearly always uninformatively tell us that $A \approx$ 100%. Of more utility here is the *probability of detection* (P_{d}) and the *probability of false alarm* (P_{f}), where

$$P_{\mathrm{d}} = \frac{M_{\mathrm{ff}}}{M_{\mathrm{ff}} + M_{\mathrm{nf}}}. \tag{3.7}$$

and

$$P_{\mathrm{f}} = \frac{M_{\mathrm{fn}}}{M_{\mathrm{fn}} + M_{\mathrm{nn}}}. \tag{3.8}$$

The resulting probabilities computed using Eqs. (3.7) and (3.8) are presented in Table 3.5.

In most regions, P_{d} varied between 0.8 and 0.9, with a somewhat lower probability

in Mexico (P_{d} = 0.71). An unusually low probability of detection (P_{d} = 0.45) was found for India. To help explain the poor performance in this region, we linked adjacent fire pixels within each expert fire mask into independent clusters, where each cluster was surrounded completely by either non-fire pixels or a scene edge. We next computed the median size of all fire-pixel clusters within each region (Table 3.5), and found that the smallest median cluster size occurred in India, where half of all fires identified were three 30-m ASTER pixels or less in size. This suggests that the fires in our Indian scenes are simply too small for reliable detection, a finding consistent with the fact that small agricultural-waste fires are abundant in this region.

Probabilities of false alarm varied between 9×10^{-8} (India) and 2×10^{-5} (USA/Canada). For a typical ASTER scene of ∼5,000,000 30-m pixels, these extremes correspond to between less than 1 and 100 false fire pixels per scene. More representative intermediate false alarms rates ($P_{\mathrm{f}} \sim 5\times10^{-6}$) yield ∼25 false fire pixels per scene. In an extension of our fire-pixel cluster analysis, we determined the fraction of false fire pixels connected to clusters of true fire-pixel clusters, f_{con}, and show this fraction in Table 3.5. In most regions the majority of false fire pixels were linked to clusters of true fire pixels, suggesting that most false fire pixels occur along the ambiguous fire boundaries.

Table 3.4: Elements of error matrix for each region.

Region	Scenes	M_{ff}	M_{nf}	M_{fn}	M_{nn}
Africa	19	4816	845	217	82193491
Australia	9	14255	2846	255	39044478
South America	10	4172	616	175	42996551
Mexico	10	1631	684	8	42931999
Europe	11	1372	147	282	47401479
India	10	2070	2507	4	43240339
USA/Canada	11	35160	8415	765	47473810
Russia	10	13548	2311	172	43891622
Southeast Asia	10	921	92	94	43603099

Table 3.5: Regional accuracy measures for ASTER fire detection algorithm.

Region	P_{d}	P_{f}	Median Cluster Size	f_{con}
Africa	0.85	3×10^{-6}	4.0	0.83
Australia	0.84	8×10^{-6}	6.0	0.93
South America	0.87	4×10^{-6}	4.0	0.92
Mexico	0.71	2×10^{-7}	4.0	0.25
Europe	0.90	6×10^{-6}	4.0	0.82
India	0.45	9×10^{-8}	3.0	1.0
USA/Canada	0.81	2×10^{-5}	5.0	0.64
Russia	0.85	4×10^{-6}	5.0	0.92
Southeast Asia	0.91	2×10^{-6}	3.5	0.76

3.6 Fire Characterization

3.6.1 Instantaneous Fire Temperature and Area

A more extensive fire-product validation could be achieved if sub-pixel average fire temperatures and instantaneous fire areas were estimated using ASTER observations. Temperature and area statistics would also allow more realistic fire scenes to be used in simulation-based approaches to fire validation [e.g., Dowty, 1996, Giglio et al., 1999, 2003b]. One approach is to use the bispectral method developed by Dozier [1981], which permits the retrieval of the temperature and area of a sub-pixel fire within an otherwise homogeneous pixel. Using slight modifications suggested by Giglio and Kendall [2001], we may write the total radiance L_i reaching the sensor in the i'th band ($i = 1, 2$) as

$$L_i = \tau_i \, p \, B_i(T_\mathrm{f}) + (1 - p) L_{\mathrm{b},i}, \tag{3.9}$$

where T_f is the fire temperature, and p is the relative fraction of the pixel containing the fire. The factor τ_i is the band-averaged atmospheric transmittance

$$\tau_i = \frac{\int_0^\infty S_i(\lambda) \, \tau_i(\lambda) \, \mathrm{d}\lambda}{\int_0^\infty S_i(\lambda) \, \mathrm{d}\lambda}, \tag{3.10}$$

where $S_i(\lambda)$ is the spectral response of the i'th channel, and $B_i(T_\mathrm{f})$ is the band-averaged Planck function:

$$B_i(T_\mathrm{f}) = \frac{\int_0^\infty S_i(\lambda) \, B(\lambda, T_\mathrm{f}) \, \mathrm{d}\lambda}{\int_0^\infty S_i(\lambda) \, \mathrm{d}\lambda} \tag{3.11}$$

The quantities $L_{\mathrm{b},1}$ and $L_{\mathrm{b},2}$ are independent estimates of the radiance contributions from the non-fire portion (or background) of the target pixel, usually taken as the

radiances of a neighboring, non-fire pixel, or the average radiances of several neighboring, non-fire pixels. Given these estimates, Eqs. (3.9) may be solved numerically for p and T_{f}. An important assumption built into Eq. (3.9) is that the fire radiates as a true black body, and thus has unit emissivity. The impact of a grey-body fire fraction is considered by Giglio and Kendall [2001].

There are numerous well documented limitations of the bispectral approach for fire characterization [e.g., Langaas, 1993b, Giglio and Kendall, 2001, Shephard and Kennelly, 2003]. With respect to the ASTER instrument, there are several limitations of particular significance. First, it is difficult to obtain a good estimate of the background radiance ($L_{\mathrm{b},i}$) within a fire pixel since the non-fire fraction contains hot, recently-burned areas having a unique temperature and area distribution not matched in neighboring non-fire pixels. This is especially true at the scale of an ASTER pixel: fire heterogeneity is more pronounced compared to sensors with $\gtrsim$1 km spatial resolution most often used for operational fire monitoring. Second, only a tiny fraction of ASTER scenes have been acquired with even a subset of the SWIR bands in either of the low gain modes, making saturation of these bands fairly common when observing fires. Since the bispectral method cannot be applied when one or both bands saturate, one might potentially appeal to "band hopping", where the band-pair used to solve Eq. (3.9) is independently chosen from the pool of unsaturated channels for each fire pixel. However, except for the case of of homogeneous fires, solving Eq. (3.9) with different band combinations can yield dramatically different solutions for p and T_{f}. As discussed by Giglio and Justice [2003], this phenomenon arises because the bispectral

method models fires as having a single, homogeneous temperature, when in fact they have a more complicated temperature distribution. In general, a fire model should allow at least a hotter flaming and a cooler smoldering component. While such models have been used successfully with hyperspectral instruments [e.g., Green, 1996], a two-fire-temperature model would require a minimum of four unsaturated ASTER channels, a feat bordering on the miraculous for nearly all of the ASTER scenes that have been acquired to date. Finally, band-to-band coregistration must meet fairly stringent requirements for the retrieved fire parameters to be accurate for fires occupying a small fraction of the pixel [Shephard and Kennelly, 2003]. A practical method of reducing the impact of misregistration (at the cost of spatial resolution) is to apply the bispectral method to clusters of adjacent fire pixels [Oertel et al., 2003], where the radiances L_1 and L_2 in Eq. (3.9) become averages of all pixels within the cluster.

To explore the potential of ASTER for fire characterization, we applied the bispectral technique to two nighttime scenes of western Zambia acquired on 3 September 2003, 20:54 UTC. (Use of nighttime imagery provided significantly fewer saturated pixels for processing.) We applied the technique to clusters of fire pixels, as described above, with radiances from band 4 (1.65 μm) and band 9 (2.40 μm) to achieve sufficient spectral separation. A total of 93 fire-pixel clusters were identified in the two scenes. Of these, one cluster could not be processed due to saturation of the 2.40 μm band, 15 clusters yielded inconsistent equations for which no solution could be found, and 11 clusters produced physically meaningless solutions (e.g., negative fire

area). For an additional 28 clusters the 1.65 μm radiance was below the band-4 detector quantization of 0.217 $\mathrm{W\,m^{-2}\,sr^{-1}\,\mu m^{-1}}$ (*normal* gain setting), effectively setting $L_1 = 0$ and preventing the solution of Eq. (3.9). The areas and mean fire temperatures of the remaining 38 clusters are shown in Fig. 3.8. The results are not encouraging. The majority of the retrieved fire temperatures are somewhat high for savanna fires, which typically burn at $\sim$900 K. More problematic are the unrealistically small fire areas, especially given that the retrieval was performed for clusters of fire pixels rather than on a per-pixel basis. Assuming a 1-m wide fire front typical of savanna fires, these results would unreasonably require that the most fronts be less than 1 m in length (indeed, less than 10 cm in nearly one third of the cases!). It is most likely that these results reflect a poor estimate of the 1.65 μm background radiance, which, for small fires, can lead to substantial retrieval bias errors analogous to those reported by Giglio and Kendall [2001] for the 4 and 11 μm band combination most often used for fire monitoring. Based on these results, the prospect of producing fire temperature and area statistics through the application of the bispectral technique to large number of ASTER scenes seems unlikely. More detailed analyses are required to fully address this issue.

3.6.2 Fire Radiative Power

The MODIS active fire product includes an estimate of the fire radiative power (FRP) emitted within each MODIS pixel [Kaufman et al., 1998b]. Among other applications, the FRP, when integrated over time, can be used to estimate combusted biomass, and is

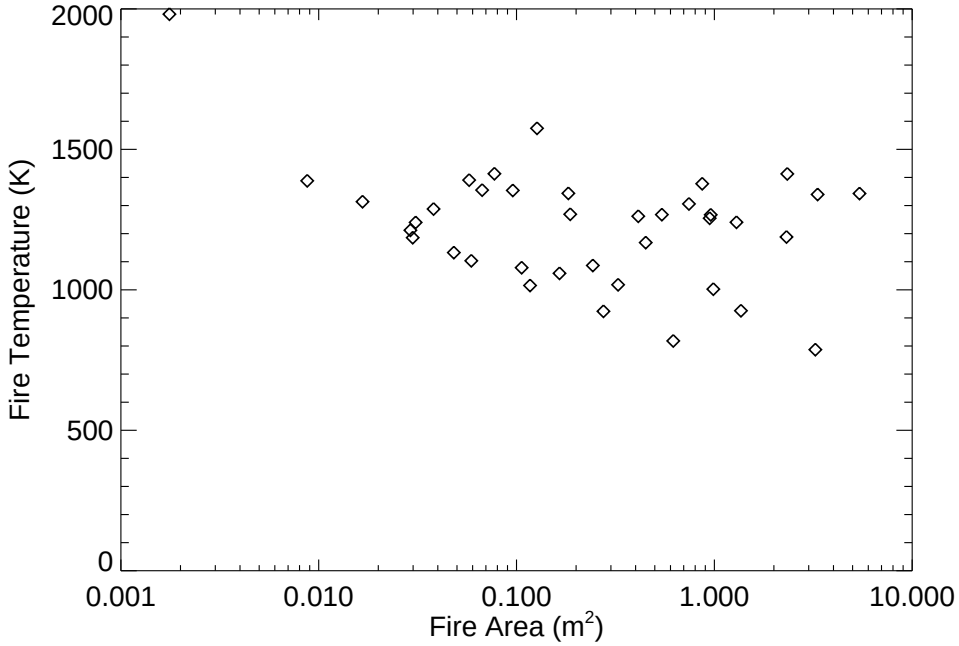

Figure 3.8: Retrieved mean fire temperature versus retrieved fire area for 38 fire-pixel clusters from two nighttime ASTER scenes of western Zambia.

thus a topic of current research for its potential in quantifying pyrogenic greenhouse-gas emissions. Although some validation of the MODIS FRP has already taken place [Wooster, 2002, Wooster et al., 2003], such cases are few in number and not yet globally representative. There is interest, therefore, in validating the MODIS FRP using comparatively large samples of ASTER fire scenes. Here we briefly consider the feasibility of such a task.

The FRP for N different fire components within a pixel, each having its own temperature and area, is defined as [Wooster et al., 2003]

$$\mathrm{FRP} = A_{\mathrm{pix}} \epsilon \sigma \sum_{i=1}^{N} p_i T_i^4, \tag{3.12}$$

where p_i is the fraction of the pixel occupied by the i'th fire component with

temperature T_i, A_{pix} is the area of the pixel, ϵ is the weighted mean emissivity of the fire components, and σ is the Stefan-Boltzmann constant.

As shown by Wooster et al. [2003], the Planck function may be approximated over a limited temperature range as

$$B(\lambda, T) \approx aT^b, \tag{3.13}$$

where a and b are empirical constants dependent upon both λ and the temperature range of interest. For wavelengths near 4 μm, choosing b = 4 yields a good approximation to the Planck function over a range of temperatures encompassing most flaming and many smoldering vegetation fires. Wooster et al. [2003] subsequently showed that this property could be exploited to estimate the FRP using a single middle-infrared band via the relationship[2]

$$\mathrm{FRP} \approx \frac{A_{\mathrm{pix}}\epsilon\sigma}{a\,\epsilon_{\mathrm{MIR}}}(L - L_{\mathrm{b}}), \tag{3.14}$$

where L is the 4 μm radiance of a fire pixel, L_{b} is an independent estimate of the radiance contributed by the non-fire portion of the pixel, and ϵ_{MIR} is the middle-infrared fire emissivity (usually assumed to be one).

For the bands available on ASTER, no useful approximation can be made over the range of fire temperatures with b = 4 in Eq. (3.13), and it is not possible to derive an analogous relationship in the form of Eq. (3.14) for ASTER. Our only recourse, therefore, is to use the instantaneous fire temperature and sub-pixel area estimates

[2]Appendix A contains a detailed derivation of this result, and corrects several comparatively minor errors in the process.

obtained from Eq. (3.9) to calculate the FRP directly, i.e.,

$$\mathrm{FRP} = A_{\mathrm{pix}} \epsilon \sigma p T_{\mathrm{f}}. \tag{3.15}$$

Use of Eq. (3.15) brings with it all of the limitations inherent in the bispectral technique, and we consequently did not attempt to apply such an approach to the ASTER scenes used in our analysis.

3.7 Conclusion

We have presented an automated fire detection algorithm for the ASTER sensor capable of mapping actively burning fires at 30-m spatial resolution. For daytime scenes, our approach uses band 8 (2.33 μm) and band 3N (0.82 μm) reflectance imagery. The former is sensitive to black-body radiation emitted by fires, while the latter is insensitive to such radiation but that provides a highly-correlated reflectance over "normal" (non-fire) components of terrestrial scenes. For nighttime scenes a simple 2.33-μm radiance threshold is applied.

Based on a statistical analysis of 100 ASTER scenes, we established omission and commission error rates for nine different regions. In most regions, P_{d} varied between 0.8 and 0.9, with a somewhat lower probability in Mexico (P_{d} = 0.71). An unusually low probability of detection (P_{d} = 0.45) was found for India, most likely because that the fires in our Indian scenes are simply too small for reliable detection, a finding consistent with the fact that small agricultural-waste fires are abundant in this region. Probabilities of false alarm varied between 9×10^{-8} (India) and 2×10^{-5}

(USA/Canada). In most regions, the majority of false fire pixels were linked to clusters of true fire pixels, suggesting that most false fire pixels occur along the ambiguous fire boundaries.

Despite occasional difficulty precisely demarcating the boundaries of large fire fronts due to saturation-induced pixel blooming, fire maps derived from ASTER are an important tool for the validation of the Terra MODIS active fire products. Validation of fire monitoring sensors on any satellite having at least an occasional overpass coincident with Terra is also possible. This includes the TRMM VIRS and the Meteosat-8 SEVIRI. Validation is perhaps the most important application of ASTER in the context of fire monitoring as the sensor's spatial coverage and revisit frequency limit its utility for routine fire monitoring. Other applications include studies of the fine structure of fire fronts, and the spatial structure of burn scars and the associated combustion completeness.

Our preliminary attempt to retrieve sub-pixel temperature and area information by applying Dozier's bispectral method to nighttime ASTER scenes was relatively unsuccessful. Retrieved temperatures and areas for savanna fires appeared to be too high in temperature and much too low in area.

Chapter 4

Global Distribution and Seasonality of Active Fires as Observed with the Terra and Aqua MODIS Sensors

4.1 Introduction

Biomass burning associated with human land-use activities, as well as naturally occurring wildfire, has come to be recognized as having an important role in regional and global climate change [Andreae, 1991]. More recently, biomass burning has been found to affect weather on much shorter time scales [Rosenfeld, 1999] and has even been implicated in the death of coral reefs [Abram et al., 2003]. With a more variable and changing climate fire distributions and regimes are likely to change [Kasischke et al., 1995, Weber and Flannigan, 1997]. There is consequently a considerable need for long-term global fire information. At present the only practical way to monitor fire activity at a continental or global scale is with sensors residing on terrestrial satellites

(Justice and Korontzi, 2001).

The launch of NASA's Terra satellite in late 1999 marked a significant step forward in the ability to monitor fires from space. The satellite's sensor payload includes the Moderate Resolution Imaging Spectroradiometer (MODIS), an instrument having 1-km middle- and long-wave infrared bands designed specifically for the observation of actively burning fires [Kaufman et al., 1998b]. In addition to offering enhanced fire detection these bands permit, for example, low intensity surface fires to be distinguished from higher intensity crown forest fires [Kaufman et al., 2003, Wooster and Zhang, 2004]. The Terra satellite occupies a sun-synchronous polar orbit with local equatorial crossing times of 10:30 (descending) and 22:30 (ascending). A second MODIS instrument on NASA's Aqua satellite, launched in mid-2002, provides an additional pair of observations at 01:30 (descending) and 13:30 (ascending) local time.

After nearly six years of data collection, there is now a sufficiently long observational record to begin meaningful time-series analyses of fire activity with MODIS data. While some longer time-series fire data sets produced with other satellite sensors are available, their application to the study of global fire activity is more limited for various reasons. The combined Along Track Scanning Radiometer (ATSR) and Advanced Along Track Scanning Radiometer (AATSR) World Fire Atlas [Arino and Rosaz, 1999], for example, currently available from July 1996 through the present, is composed exclusively of nighttime fire observations; this can skew the apparent distribution of fire activity in those regions having a strong diurnal fire cycle. The Tropical Rainfall Measuring Mission (TRMM) Visible and Infrared Scanner (VIRS)

monthly fire product [Giglio et al., 2003b], which currently spans January 1998 through the present, is restricted to tropical and subtropical latitudes by the highly inclined orbit of the TRMM satellite. Although fire data sets are routinely generated for some regions using NOAA Advanced Very High Resolution Radiometer (AVHRR) 1-km data, global data sets are only available for a limited period [Stroppiana et al., 2000b]. A further limitation common to these data sets arises from the fact that the sensors from which they were derived were not intended for monitoring fires. As such, their optical and radiometric specifications – most importantly, the levels at which the bands useful for fire monitoring saturate – generally preclude fire characterization beyond simply flagging the existence of one or more active fires within a pixel.

In this chapter, we examine global fire activity using observations made with the MODIS instruments on board NASA's Terra and Aqua satellites. As part of our analysis we present, for the first time, a global picture of the middle-infrared fire radiative power (FRP), a relatively new remotely sensed quantity proposed by Kaufman et al. [1998b]. Our work complements earlier global fire studies based solely on fire count information by Dwyer et al. [1999] and Dwyer et al. [2000a] using the AVHRR Global Fire Product [Stroppiana et al., 2000b] from April 1992 through March 1993, and by Csiszar et al. [2005] who used the first two years of MODIS fire observations. In Section 4.2 we describe the remotely sensed data used in this study, and include a detailed description of the new MODIS Climate Modeling Grid (CMG) active fire products. These summary products are generated from the full resolution, orbital data to facilitate global analyses. Next, in Section 4.3, we describe the spatial

and temporal metrics used to extract summary information from the time series of MODIS fire observations. We then use the metrics to examine the global distribution of biomass burning (Section 4.4), and perform a preliminary examination of the diurnal fire cycle using combined Terra and Aqua MODIS observations (Section 4.5). In Section 4.6, we quantify the extent to which the Terra and Aqua MODIS fire data records are in agreement with respect to the seasonality of fire activity. Finally, in Section 4.7, we examine the sensitivity of our results to seasonal and interannual variations in cloud cover.

4.2 Data

4.2.1 MODIS Climate Modeling Grid (CMG) Fire Products

The MODIS Climate Modeling Grid (CMG) fire products have recently been developed and are primarily intended to facilitate the incorporation of the MODIS active fire data into global emissions and chemical transport models [Justice et al., 2002]. Recent applications include work by Edwards et al. [2004, 2006] and Giglio et al. [2006b]. Currently, the Terra and Aqua CMG fire products are generated on a monthly basis at 0.5° spatial resolution to maintain compatibility with the AVHRR Global Fire Product, and an earlier multi-year fire data set derived from TRMM VIRS data [Giglio et al., 2003b]. Higher spatial and temporal resolution MODIS CMG fire products (8 days, 0.25°) are presently being generated on an experimental basis. In this

study we used the Collection 4 Terra and Aqua MODIS monthly CMG fire product at 0.5° spatial resolution ("MOD14CMH" and "MYD14CMH"), from November 2000 (Terra) and July 2002 (Aqua) through October 2005. Here we briefly describe the individual data layers of the current CMG fire product suite.

Overpass-corrected fire pixel counts. As discussed by Giglio et al. [2003b], the traditional "gridded fire counts" obtained from polar orbiting satellites are biased at high latitudes due to non-uniform spatial and temporal sampling. The total number of fire pixels observed in each grid cell is therefore corrected for multiple satellite overpasses and missing observations. This is accomplished by normalizing the raw fire pixel counts by the expected equatorial coverage in a complete calendar month containing no missing observations. The overpass-corrected fire pixel count in the grid cell located at row i and column j, denoted as $N'_{\mathrm{fire}}(i,j,t)$, is given by

$$N'_{\mathrm{fire}}(i,j,t) = \frac{N_{\mathrm{fire}}(i,j,t)\, N_{\mathrm{days}}(t)\, A(i)\, N_{\mathrm{eq}}}{N_{\mathrm{total}}(i,j,t)\, A_{\mathrm{eq}}} \tag{4.1}$$

where $N_{\mathrm{fire}}(i,j,t)$ is the number of active fire pixels detected in the grid cell over a given calendar month indexed by t, $N_{\mathrm{total}}(i,j,t)$ is the total number of MODIS pixels that fell within the grid cell during the calendar month, $N_{\mathrm{days}}(t)$ is the number of days in the calendar month, $A(i)$ is the area of the grid cell (solely a function of i due to the equal-angle grid used to composite pixels), A_{eq} is the area of a grid cell along the Equator, and N_{eq} is the expected number of MODIS pixels within a grid cell located along the Equator during a full 24-h day of no missing observations. The value of this last quantity was determined empirically using one year of observations from 2001.

Mean cloud fraction. The average fraction of each grid cell obscured by cloud during a given calendar month, $\overline{f}_{\text{cloud}}$, defined as

$$\overline{f}_{\text{cloud}}(i,j,t) = \frac{N_{\text{cloud}}(i,j,t)}{N_{\text{total}}(i,j,t)} \tag{4.2}$$

where $N_{\text{cloud}}(i,j,t)$ is the total number of cloud pixels within the grid cell during calendar month t.

Cloud-and-overpass-corrected fire pixels. The number of fire pixels observed in each grid cell, corrected for multiple satellite overpasses, missing observations, and variable cloud cover. The cloud-and-overpass-corrected fire pixel count, denoted as $N'_{\text{fire}}(i,j,t)$, is given by

$$N''_{\text{fire}}(i,j,t) = \frac{N'_{\text{fire}}(i,j,t)}{1 - \overline{f}_{\text{cloud}}(i,j,t)} \tag{4.3}$$

Grid cells for which the mean cloud fraction is 1 are assigned a cloud-and-overpass-corrected fire pixel count of zero. This correction is based upon the assumption that the number of fire pixels per unit area within both clear and cloud-obscured areas is identical, an assumption which is not always reasonable [Eva and Lambin, 1998]. In the future we will incorporate a more realistic cloud correction that distinguishes between raining and non-raining clouds. Figure 4.1 illustrates the effects of the overpass-correction and the cloud-and-overpass-correction for the July 2002 Terra CMG product.

Mean fire radiative power. The mean fire radiative power (FRP) of all fire pixels in each grid cell during a calendar month. The FRP retrieval [Kaufman et al., 1998b] requires an estimate of the background, middle infrared non-fire radiance (or

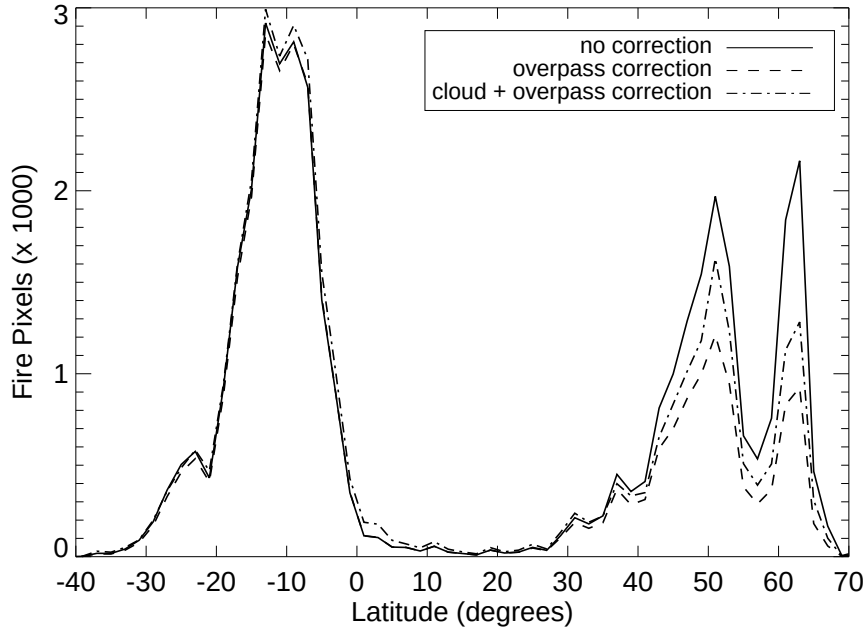

Figure 4.1: Zonal profile of fire-pixel counts from the July 2002 Terra CMG product illustrating the typical effect of the overpass- and cloud-and-overpass corrections (broken lines) on the uncorrected (raw) fire-pixel counts (solid line). Boreal fire activity this particular month was unusually high.

brightness temperature) in the immediate vicinity of the fire. This quantity, which is computed as part of the background characterization phase of the fire detection algorithm [Giglio et al., 2003a], is sometimes unavailable in the neighborhood of heavy cloud cover, very large fires, and small islands or peninsulas. Fire pixels for which this is the case are not included in the calculation of the mean. Fire pixels detected at scan angles above 40° are also excluded as they are affected by a significant off-nadir bias.

The utility of the FRP for estimating combusted biomass was first proposed by Kaufman et al. [1998b] and subsequently refined by Wooster et al. [2003]. In short, the remotely sensed FRP is, to a good approximation, equivalent to the total radiative

power of the fire as described by the Stefan-Boltzmann law. By integrating the FRP over the duration of a fire, one obtains the fire radiative energy (FRE). To the extent this latter quantity is proportional to the total energy released during combustion, one can calculate the mass of fuel consumed given the heat of combustion for that fuel. For vegetation there is fortunately relatively little variation in the latter quantity, and a constant value can usually be assumed everywhere [Johnson, 1992]. Although the original goal in developing the FRP was to improve estimates of pyrogenic emissions, the mean FRP can also provide useful information about fire behavior. This will be discussed in Section 4.4.3.

Land cover statistics. For emissions modeling, land cover information is often used to determine fuel loads and emission factors [e.g., Streets et al., 2003]. Within the CMG product we have therefore included the mean percent tree cover, percent herbaceous vegetation cover, and percent bare ground from the global MODIS Vegetation Continuous Fields (VCF) products [Hansen et al., 2003] for all fire pixels within each grid cell during a given calendar month.

Mean detection confidence. The mean detection confidence of all fire pixels detected within each grid cell, included primarily for quality assurance. The detection confidence, which varies between 0 and 100%, is a heuristic measure of the radiometric contrast between a fire pixel and its immediate non-fire neighborhood, with extra penalties imposed near potential false alarm sources such as cloud edges and coastline [Giglio et al., 2003a].

Additional data layers. Additional layers containing simple counts of missing data,

unknown and total pixels are included to assist quality assurance and simplify the production of experimental high-level datasets.

In generating the above data layers, fire pixels associated with persistent static fire sources were excluded. These were identified on a 1-km global grid as follows: any 1-km grid cell in which fire pixels were detected on 50 or more unique calendar days per year was deemed a persistent source not representing a vegetation fire. The locations of such sources are shown in Figure 4.2. The majority represent static gas flares associated with oil drilling. Though small in size, gas flares usually burn at comparatively high temperatures, typically between 1000 K and 1900 K (SEPA, 2002), and are readily detected by satellite sensors. They have been mapped extensively by Elvidge et al. [1997] using the Defense Meteorological Satellite Program Operational Linescan System, and occur primarily in North Africa, the Middle East, Gabon, Russia, and Ukraine. Persistent fire pixels are also associated with active volcanoes and a smaller number of unknown sources (possibly power stations) located within urban areas. Sources in this last category may represent recurring false alarms near industrial sites and are being investigated as part of our ongoing validation activities.

4.2.2 Agricultural Data

We used the Ramankutty and Foley [1998] version 1.1 global croplands data set, at 0.5° spatial resolution, to supply agricultural land-use distributions.

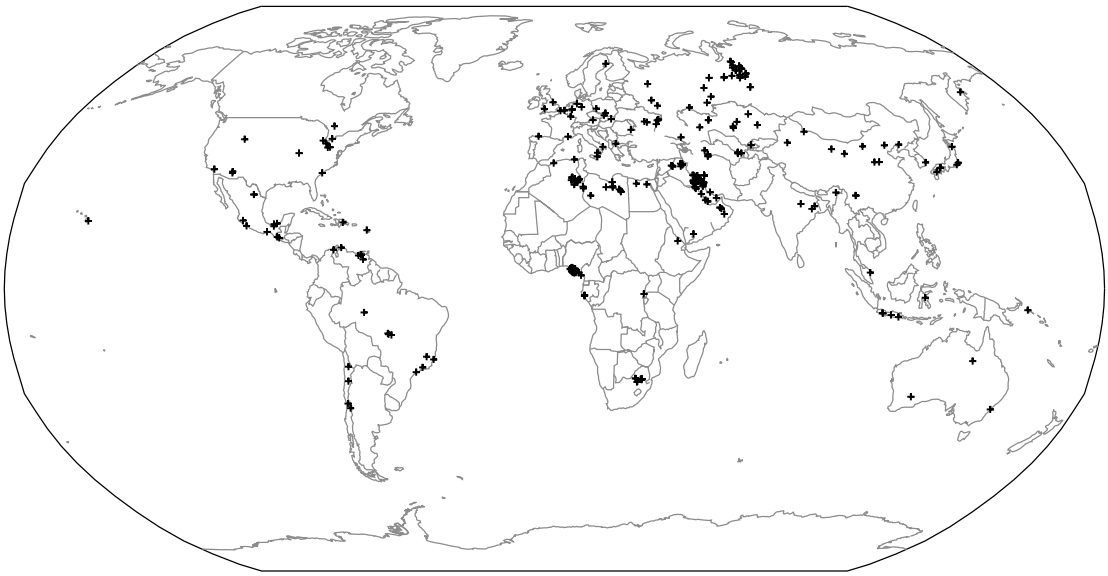

Figure 4.2: Locations of persistent static fire sources identified using five years of MODIS active fire observations, and subsequently filtered from the Terra and Aqua MODIS CMG fire products.

4.3 Analysis Approach

Our analysis is similar to that used by Dwyer et al. [1999, 2000a] with the 21-month AVHRR Global Fire Product [Stroppiana et al., 2000b]. We generated a "climatological" Terra MODIS monthly data set by independently averaging the overpass-corrected fire pixel counts for each calendar month from November 2000 through October 2005. We then extracted multiple spatial and temporal metrics from this climatological data set, as well as the full monthly Terra time series. Within these metrics we next identified patterns and trends, which we interpreted with respect to different biophysical variables and current knowledge of regional burning practices. Our goal was to describe and, in part, explain the global spatial and temporal distribution of fire activity as observed by MODIS.

4.3.1 Spatial Metrics

We calculated the average annual overpass-corrected fire pixel density for MODIS by summing the average monthly overpass-corrected fire counts and dividing by grid cell area. The latter step was necessary to compensate for the non-equal area of the equal-angle grid cells used to bin the data. We also averaged the November 2000–October 2005 Terra MODIS monthly fire radiative power (FRP), weighted by the number of overpass-corrected fire pixels for each month, to produce a climatological map of mean annual FRP. Grid cells containing fewer than five fire pixels per year were deemed as having little real signal and were excluded from the subsequent analysis.

4.3.2 Spatio-temporal Metrics

Global fire activity exhibits a strong seasonality that can be characterized using any number of parameters in both the time and frequency domain. Here, we have selected three different temporal metrics, computed independently for each grid cell, that are intuitive and readily understood. First, we define the peak in fire activity as the calendar month during which the maximum number of average monthly overpass- corrected fire counts was detected. Second, we define the duration of the fire season as the number of months during which the average monthly overpass-corrected fire counts was at least 10% of the average annual overpass-corrected fire counts. Third, we employ the 12-month lagged autocorrelation of the full five-year monthly time series to provide a measure of the interannual variability and periodicity of fire activity. Grid cells having

very similar annual cycles of fire activity will have a 12-month lagged autocorrelation approaching +1, while those grid cells exhibiting significant interannual variability have positive or negative values much closer to zero. (An autocorrelation approaching -1 would indicate a significant biannual fire cycle. This might happen as a result of specific agricultural practices, but is otherwise not expected.) We expect the 12-month lagged autocorrelation to provide a combined measure of anthropogenic (versus natural) fire activity and climatic constraints. Specifically, regions of high anthropogenic fire activity and low interannual rainfall variability should exhibit a very high temporal autocorrelation. Conversely, regions of low anthropogenic fire activity and high interannual rainfall variability should exhibit a very low temporal autocorrelation. The remaining cases, high anthropogenic fire activity/high rainfall variability and low anthropogenic fire activity/low rainfall variability, should exhibit moderately high and moderately low temporal autocorrelation, respectively.

4.4 Results

4.4.1 Fire Counts

The average annual overpass-corrected fire pixel density for the Terra MODIS is shown in Figure 4.3a. The overall pattern is largely consistent with that found by Dwyer et al. [2000b] using one year of the AVHRR Global Fire Product (GFP). There are some substantial differences, however, in the distribution of areas containing little or no fire

activity. With respect to those areas in which the MODIS fire product shows significant fire activity while the GFP shows none, this is explained by the static desert mask used in the production of the AVHRR data set. This mask was used to identify, a priori, those regions in which fires should not occur and thereby remove false detections over hot desert surfaces which are problematic for the GFP algorithm [Stroppiana et al., 2000b]. Within some of these regions, however, fires do in fact occur, most notably in northwest Australia. Possible explanations for the complimentary case in which the GFP shows significant fire activity in locations where the MODIS fire product shows little or no fire activity are most likely due to interannual variability and a much higher incidence of false detections in the GFP [Giglio et al., 1999, Ichoku et al., 2003, Csiszar et al., 2005]. With respect to the latter point, the GFP shows widespread burning across the entire continental United States, for example, which does not actually occur.

The location of greatest annual fire activity occurs within the so-called Arc of Deforestation in Brazil at approximately 13°S, 55°W. Barring static gas flares, the density of fire pixels detected at this location is more than a factor of two higher than anywhere else in the world. This is a region of intense land-cover conversion in which rainforest is rapidly being transformed into pasture, with subsequent burning of the forest slash and repeated burning for pasture maintenance.

4.4.2 Seasonality

The peak month of Terra MODIS fire activity is shown in Figure 4.3b. At the global scale, July, August, and September are the peak months of fire occurrence, with fires in both the northern and southern hemispheres, while February is least often the month of peak fire occurrence. The most striking feature is perhaps the six-month difference in the timing of greatest fire activity in Africa north and south of the Equator, as a consequence of the opposite phase in the timing of the African dry season in these regions. Global patterns in the seasonality of fire counts have previously been described by Dwyer et al. [1999], Dwyer et al. [2000b], van der Werf et al. [2003], and Csiszar et al. [2005], and will not be repeated here, but it is worth reiterating that both the peak month and the duration of the fire season are coupled to the seasonal cycle of precipitation, particularly in the tropics. (Note that Dwyer et al. [1999, 2000b] used a somewhat different criterion for identifying the "central time" of fire activity, namely the calendar month during which 50% of the cumulative monthly fire pixels from April 1992 through March 1993 were detected.)

Fire season duration is shown in Figure 4.3c. Globally, the duration of the annual fire season usually varies between 2 and 6 months and is, in the tropics, highly constrained by the duration of the dry season. Exceptionally long fire seasons of $\sim$10 months occur in central and southern Brazil and the southeastern United States. A similarly long fire season occurs in a small area in eastern Australia (approximately 28°S, 149°E) and might be associated with sugarcane residue burning that takes place

throughout the comparatively long (∼8 month) harvesting season. An analysis at higher spatial resolution is ultimately needed to verify this hypothesis. The duration of the fire season at boreal latitudes is uniformly short at 1-3 months, and is constrained by the seasonality of circulation patterns [Johnson, 1992].

The highest 12-month lagged temporal autocorrelation (Figure 4.4a) occurs in the savannas of Africa, both in the sudanian and sahelian zones north of the Equator and in central and southern Africa between 5°S and 20°S, reflecting the extremely periodic seasonal cycle of fire activity in these regions, and also indicating that they experience less interannual variability. This characteristically strong annual periodicity is caused by a combination of widespread human-induced burning for land maintenance purposes and low interannual variability in rainfall during the study period. The areas to the north and south of these two regions respectively show decreasing annual autocorrelation associated with greater interannual variability in rainfall and grass (fuel) production. Other regions of very high temporal autocorrelation occur in the tropics, e.g. Thailand, Cambodia and Laos in Southeast Asia, Mexico and Central America, and the Llanos, Mato Grosso, and Brazilian Highlands of South America. The small spot of high periodicity in northern India (31°S, 75°E) reflects seasonal agricultural waste burning at the beginning and end of the growing season in May and October.

Regions of significant interannual variability (and significantly less periodicity) include the United States, southwest China, Siberia, Canada, and virtually the entire Australian continent, reflecting the much more sporadic nature of fire in these

locations. In both Siberia and boreal North America large fires occur in areas of extensive forest cover, which require very long time periods for regrowth, making it unusual for a given patch of vegetation to burn in successive years.

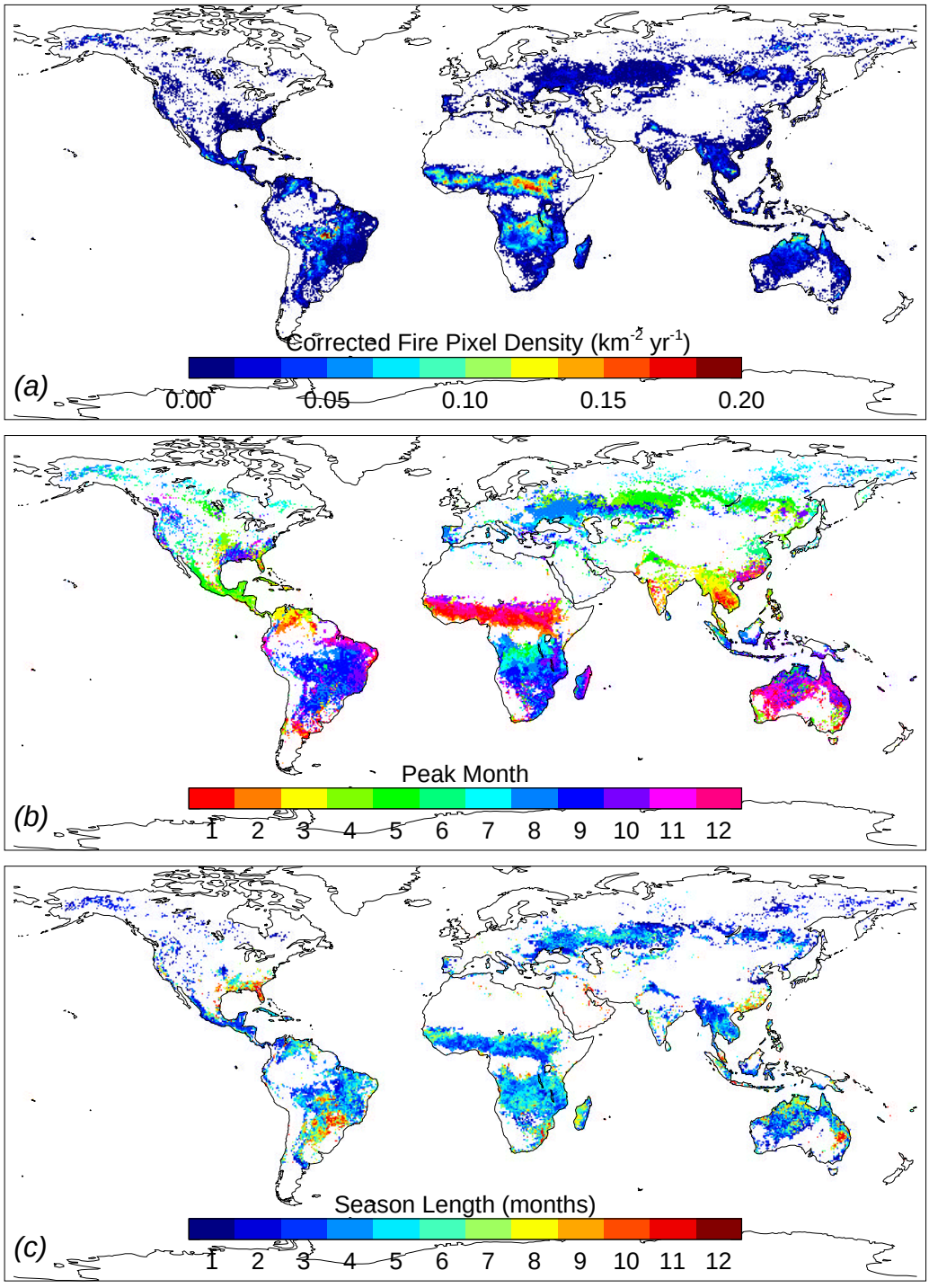

Figure 4.3: Climatological fields derived from the first five years of Terra MODIS fire observations (November 2000–October 2005). (a) Mean annual overpass-corrected fire pixel density; (b) month of maximum climatological fire activity; (c) fire season length.

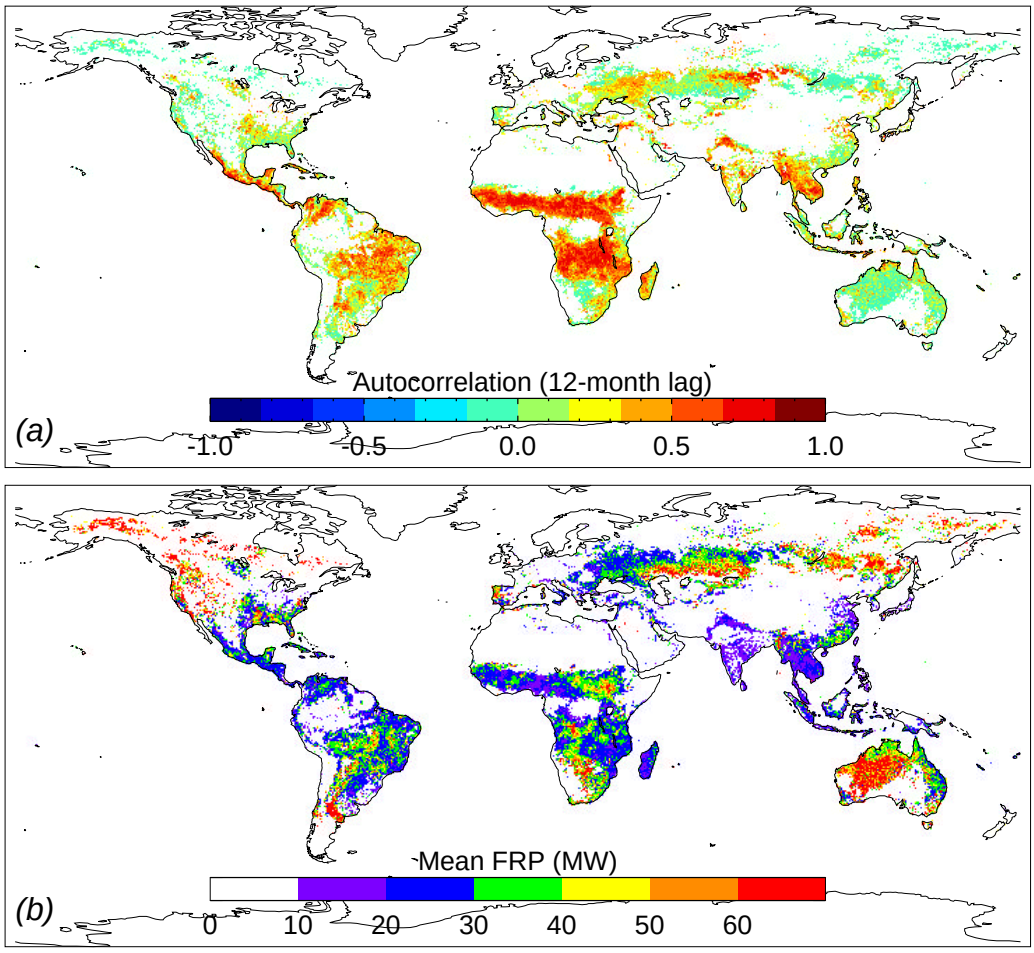

Figure 4.4: Additional climatological fields derived from the first five years of Terra MODIS fire observations (November 2000–October 2005). (a) 12-month lagged autocorrelation of the overpass-corrected fire count time series within each grid cell; (b) mean annual fire radiative power (FRP).

4.4.3 Fire Radiative Power

The climatological fire radiative power for the Terra MODIS is shown in Figure 4.4b. In general, low FRP (∼15 MW) tends to be associated with areas of extensive cropland, regardless of location, reflecting the fact that agricultural fires are usually controlled and remain small. In the tropics and much of the sub-tropics, low FRP is also associated with more heavily forested areas, while higher FRP (∼40 MW) tends to occur in grassland areas. In the absence of cutting trees and a subsequent drying period, fuel moisture in tropical forests is usually too high to permit large (or intense) fires; fires that do manage to burn are more likely to consist of cooler, smoldering combustion. Lighter herbaceous fuels, however, dry out much more quickly and are consumed via hotter flaming combustion. The hotter, flaming fires of the grasslands of northern and western Australia show the largest area of high FRP. These fires are more energetic than the savanna fires in Africa and Brazil. In boreal forests a very different trend is observed. Here, very high FRP (∼80 MW) occurs in areas having greater tree cover and less herbaceous vegetation, reflecting the very large fuel loads available in boreal forest.

Several smaller-scale features stand out in the spatial distribution of the fire radiative power. First, the band of anomalously high FRP (∼60 MW) in the Rio Negro Province of Argentina is confined to a relatively narrow swath of xeromorphic shrubland [Soares, 1990]. Second, the highest values of FRP (up to 600 MW) occur in the boreal zones of Siberia, Canada, and Alaska. In these regions, which are

predominantly forested, dry-weather fuel loads are extremely high, and the size of the actively burning areas can grow to be very large. Higher radiative power is to be expected from the more energetic crown fires in these regions, and the FRP could potentially allow crown vs. surface fires to be distinguished remotely. Wooster and Zhang [2004] used MODIS FRP to demonstrate that North American boreal forest fires are dominated by crown fires, whereas Siberian forest fires are less intense and most likely burn at the surface. We found a five-year mean FRP of 81.2 MW in boreal North America vs. 53.7 MW in boreal Russia, a result consistent with their findings. Lastly, the prominent latitudinal FRP gradient in Ukraine, Russia, and Kazakhstan very closely matches the land cover transition from cropland to grassland. This pattern is consistent with the corresponding latitudinal gradient in temporal autocorrelation seen in Figure 4.4a.

The latitudinal distributions of mean fire pixel density and mean FRP in 5° zones are shown in Figure 4.5. The most notable feature is the general increase in FRP with increasing latitude, which is opposite the trend of higher fire pixel densities at lower latitudes on either side of the Equator. Both trends are entirely consistent with the general decrease in temporal autocorrelation towards higher latitudes. Taken as a whole, the trends in all three quantities are indicative of a general shift from more-controlled seasonal burning in the tropics and sub-tropics (with lower fuel loads), to less-controlled episodic fires at higher latitudes (with higher fuel loads). A second feature evident in Figure 4.5 is the asymmetry of zonal FRP with respect to the Equator. This asymmetry arises from the different distributions of land and fire regimes

within the northern and southern hemispheres, in particular the combination of the relatively low FRP contributed by India and Southeast Asia with the relatively high FRP contributed by Australia and Argentina.

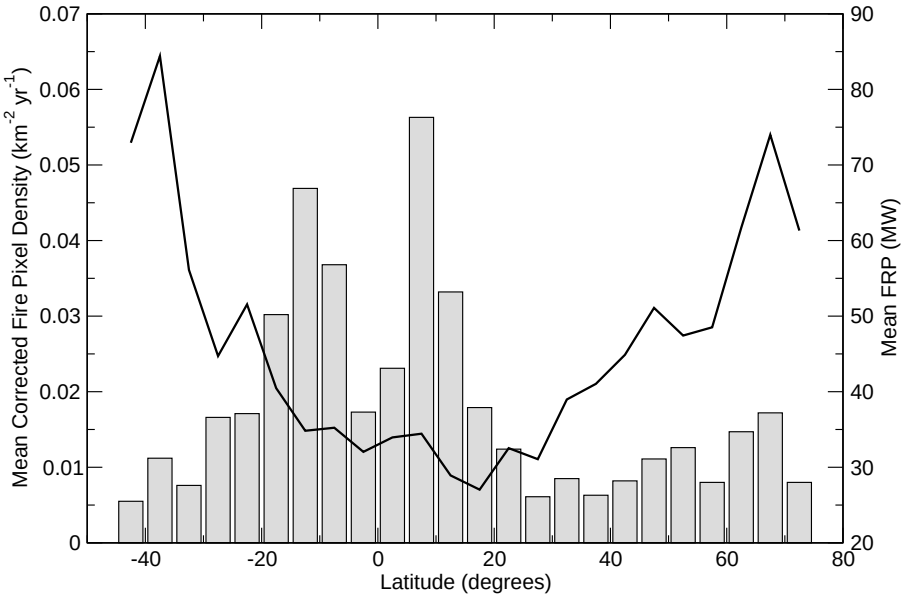

Figure 4.5: Mean density of overpass-corrected fire pixels (grey bars) and mean fire radiative power (black line) within 5° latitude zones from the first five years of Terra MODIS observations.

4.5 Diurnal Fire Cycle

The Terra and Aqua satellites lie in polar orbits with local equatorial crossing times of 10:30/22:30 and 01:30/13:30, respectively. This offers the opportunity to examine different points of the diurnal fire cycle. Previous work by Prins and Menzel [1992], Eva and Lambin [1998], Pack et al. [2000], Justice et al. [2002], and Giglio et al.

[2003c] has shown that such a cycle exists in Africa, Brazil, and parts of Indonesia, but both the extent and magnitude if this cycle have yet to be established over most of the globe.

A separate analysis (not shown) revealed that the majority (∼90%) of Terra and Aqua MODIS fire pixels in the tropics and subtropics were detected during the daytime overpasses. Therefore, a comparison of all (i.e., both daytime and nighttime) Terra MODIS fire pixels to all Aqua MODIS fire pixels primarily reflects a difference in the diurnal fire cycle between mid-morning and early afternoon. To this end, we show the fraction of all (Terra + Aqua) overpass-corrected fire pixels detected by the Aqua MODIS instrument within each 0.5° grid cell in Figure 4.6. Based on this figure one may, to first order, divide the globe into three classes: 1) areas of negligible morning fire activity, with nearly 100% of all fire pixels detected by the Aqua MODIS; 2) areas of predominantly early afternoon fire activity, with about 75% of all fire pixels detected by the Aqua MODIS; and 3) areas where early afternoon and mid-morning fire activity are about evenly matched. The first category tends to occur in the broadleaf forests of West Africa, Central Africa, Borneo, and Brazil, and cropland in southeast Australia. The second category occurs primarily in southern and sub-Saharan Africa (with notable exceptions in Sudan and Ethiopia), Southeast Asia, Indonesia, southwest Australian cropland, and a large crescent-shaped swath in eastern Brazil of comparatively heterogeneous vegetation cover. The final category is found primarily in northern and western Australia, central Eurasia, and the boreal forests of Siberia and North America. Within this last category are fires that, once ignited, typically burn for

at least several days and up to many weeks.

A complication that we have touched on in the previous discussion is that the MODIS instruments make multiple daytime and nighttime observations at high latitudes each day since the Terra and Aqua satellites reside in sun-synchronous polar orbits. This means that, at high latitudes, each instrument samples more than two local times (one daytime plus one nighttime) of the diurnal cycle each day. (The extreme case occurs at the poles with nearly 15 observations each day.) As a result, the local time windows sampled at boreal latitudes by each of the MODIS instruments overlap, and the ratio we show in Figure 4.6 is in fact not a consistent measure of the degree to which a diurnal fire cycle might exist. At boreal latitudes the simple fire-count ratio can potentially mute the apparent magnitude of the diurnal fire cycle due to the overlap in local observation times. Nevertheless, Figure 4.6 does illustrate the minimum spatial extent of regions having a pronounced diurnal fire cycle.

4.6 Terra/Aqua MODIS Comparison

4.6.1 Time series comparison

The previous analysis of the diurnal fire cycle raises the practical issue of the consistency of the fire time series recorded by the two MODIS instruments. Clearly there will be differences in the absolute numbers of fire pixels detected with each (cf. Figure 4.6), but of equal concern are potential differences in the seasonality of fire

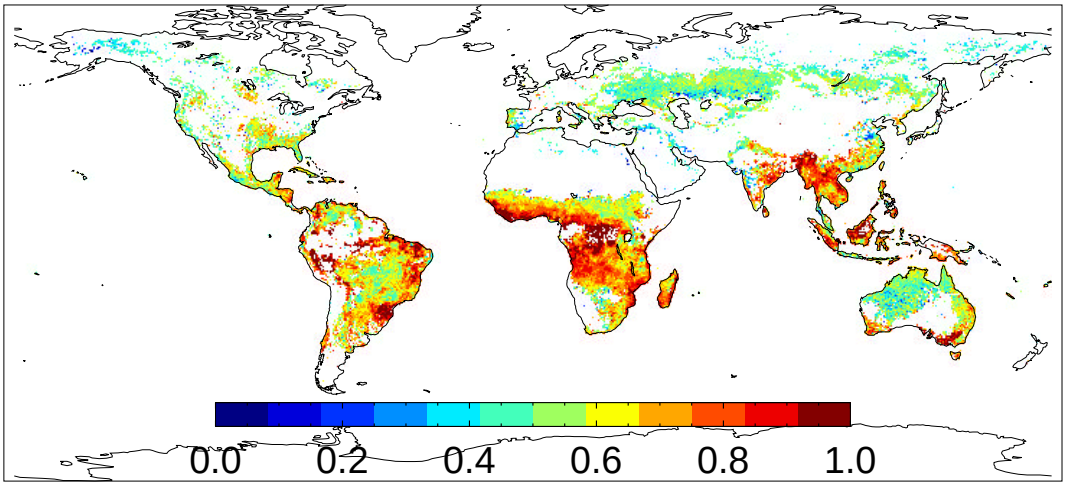

Figure 4.6: Ratio of overpass-corrected Aqua fire pixel counts to total (Aqua + Terra) overpass-corrected fire pixel counts from July 2002 through June 2005. Red and orange colors indicate regions in which a significant diurnal fire cycle exists.

activity. To quantify the consistency in seasonality, we calculated the cross-correlation of the Terra and Aqua overpass-corrected fire-pixel time series for each grid cell from July 2002 through October 2005 (Figure 4.7). The cross-correlation is sensitive to differences in the timing of fire activity (fire season length, location and number of peaks), but relatively insensitive to differences in the magnitude of the time series.

In general, the cross-correlation of the two time series was high ($\sim$0.9) in most areas of the world, indicating that the two MODIS instruments generally show good agreement with respect to the peak month of fire activity and the length of the fire season. Exceptions occur in the Southeastern United States, Eastern South America, Liberia, Central Africa, Eastern China, Borneo, and Southeast Australia. To help understand these "anomalous" cases we examined the individual monthly time series in spatial windows located within each region (Table 4.1). Six examples are shown in

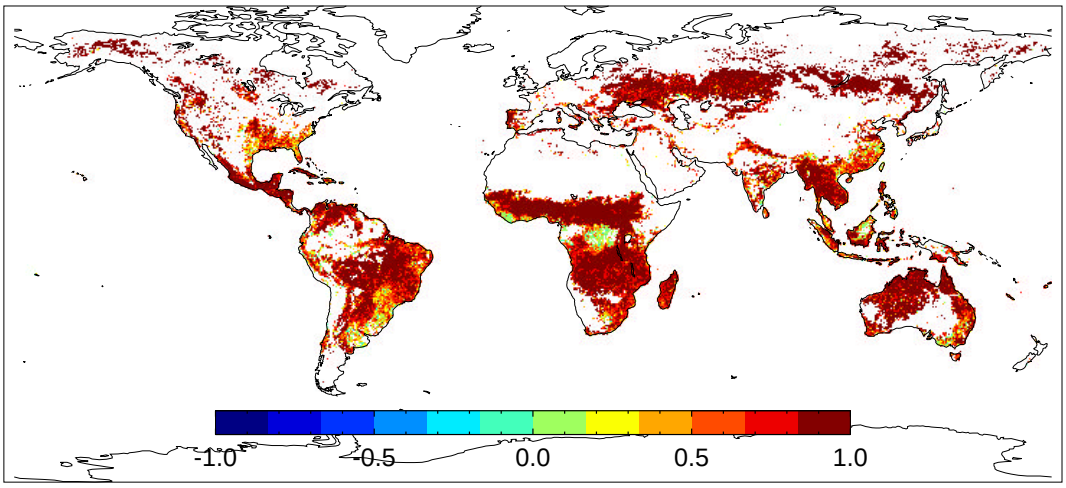

Figure 4.7: Cross correlation of Terra vs. Aqua overpass-corrected monthly fire pixel counts from July 2002–October 2005.

Figure 4.8 (a-f). For comparison, we also show the time series for four regions having a high cross correlation (Figure 4.8g–4.8j).

The largest discrepancies in seasonality uniformly occurred in the tropical rainforests of Liberia, Borneo, Central Africa, and the Amazon Basin. Here, Aqua yields fire seasons five to ten times longer than those derived from Terra observations (Figures 4.8c and 4.8d). The time series as well as Figure 4.6 show that an extremely strong diurnal fire cycle exists in tropical rainforest, rendering the Terra MODIS virtually blind to fires in this ecosystem. To a slightly lesser extent this observation also applies to the dry forests of Southeast Australia (Figure 4.8f). Southeast USA, Eastern Argentina, and Eastern China (Figures 4.8a, 4.8b, and 4.8e, respectively) are characterized by a relatively weak diurnal fire cycle and show some notable discrepancies in the months during which peaks occurred. In these regions, the poorer consistency of the Terra and Aqua time series likely stems from the more

Table 4.1: Regions considered in Terra/Aqua time series comparison, with cross-correlation coefficients for the overlapping portion of the time series (July 2002 – October 2005) shown in Figure 4.8.

Name	Latitude	Longitude	BLAH
Southeast USA	27.5°N - 33°N	84°W - 80.5°W	0.77
Eastern Argentina	32°N - 38.5°N	64°W - 58.5°W	0.87
Liberia	4°N - 7.5°N	11°W - 7°W	0.26
Central Africa	3°S - 1.5°N	20.5°E - 29°E	0.61
Eastern China	28.5°N - 32°N	116°E - 122°E	0.62
Southeast Australia	34°S - 38°S	140°E - 145.5°E	0.54
Pacific Northwest USA	42°N - 52°N	125°W - 115°W	0.99
Southeast Russia	49°N - 54°N	110°E - 135°E	0.99
Southern Africa	6°S - 14°S	15°E - 30°E	0.98
Northern Australia	12°S - 21°S	126°E - 137°E	0.96

heterogeneous types of fires within each, including managed prescribed fires, burning of agricultural waste, and arson. Each fire category is likely to follow different seasonal and diurnal cycles. In combination, one would expect a less coherent time series that is not necessarily consistent between the two platforms.

We note that the time series for Southeast Australia, Pacific Northwest USA, and Southeast Russia (Figures 4.8f–4.8h) illustrate the importance of using long-term time series to capture interannual variability in biomass burning. Climatologies based on one or two years of active fire observations can greatly misrepresent “normal” levels of fire activity over large areas of the globe. Indeed, nearly 40% of all fire-affected grid cells in our five-year Terra MODIS fire climatology have a temporal autocorrelation (Figure 2d) less than 0.1 (i.e., these cells exhibit very significant interannual variability). We recognize that this fraction does not include grid cells for which even a five-year time series is insufficient to capture the episodic fires characteristic of some

regions (e.g., boreal forest).

In the above analysis, we have ascribed differences in the Terra and Aqua time series to the different sampling of the diurnal fire cycle, but there are at least two additional mechanisms by which differences can arise. First, the performance of the detection algorithm, both in terms of the probability of detecting a fire as well as the likelihood of yielding a false detection, is dependent upon environmental conditions that vary with respect to time of day, including surface temperature and solar zenith angle. Second, intrinsic differences in the Terra and Aqua MODIS instruments (or their calibration) could potentially contribute to a difference in observed fire activity.

To estimate the magnitude of these effects relative to that of the diurnal fire cycle, we examined the fire time series in three different regions containing high-temperature sources that were not expected to show a significant diurnal cycle: the Kilauea volcano on the southern-most island of Hawaii, and gas flares associated with oil fields in southern Iraq and the Niger Delta. The July 2002 – December 2004 time series for each region is shown in Figure 4.9. For Kilauea and the Niger Delta, the magnitude of the discrepancies in the Terra and Aqua fire-pixel time series are well within the uncertainties entailed by cloud obscuration. In southern Iraq, Terra fire counts are consistently higher ($\approx$16%) than those of Aqua. This is most likely caused by the near-infrared minimum-reflectance test used in the detection algorithm, which is preventing detection of some gas flares at the time of the Aqua overpass when the top-of-atmosphere reflectance is slightly higher. While a 16% discrepancy is not negligible, this case probably illustrates the effect at its largest due to the abundance of

bright soil in this region.

4.6.2 FRP Comparison

We also compared the July 2002–October 2005 global distribution of mean FRP derived from Aqua observations with that derived from Terra observations for the same time period. The Aqua FRP distribution was very similar to that of Terra, but approximately 10% larger in magnitude. This difference may be explained by Aqua's afternoon sampling of the diurnal fire cycle, at which time fires tend to be burning in larger numbers and with greater intensity.

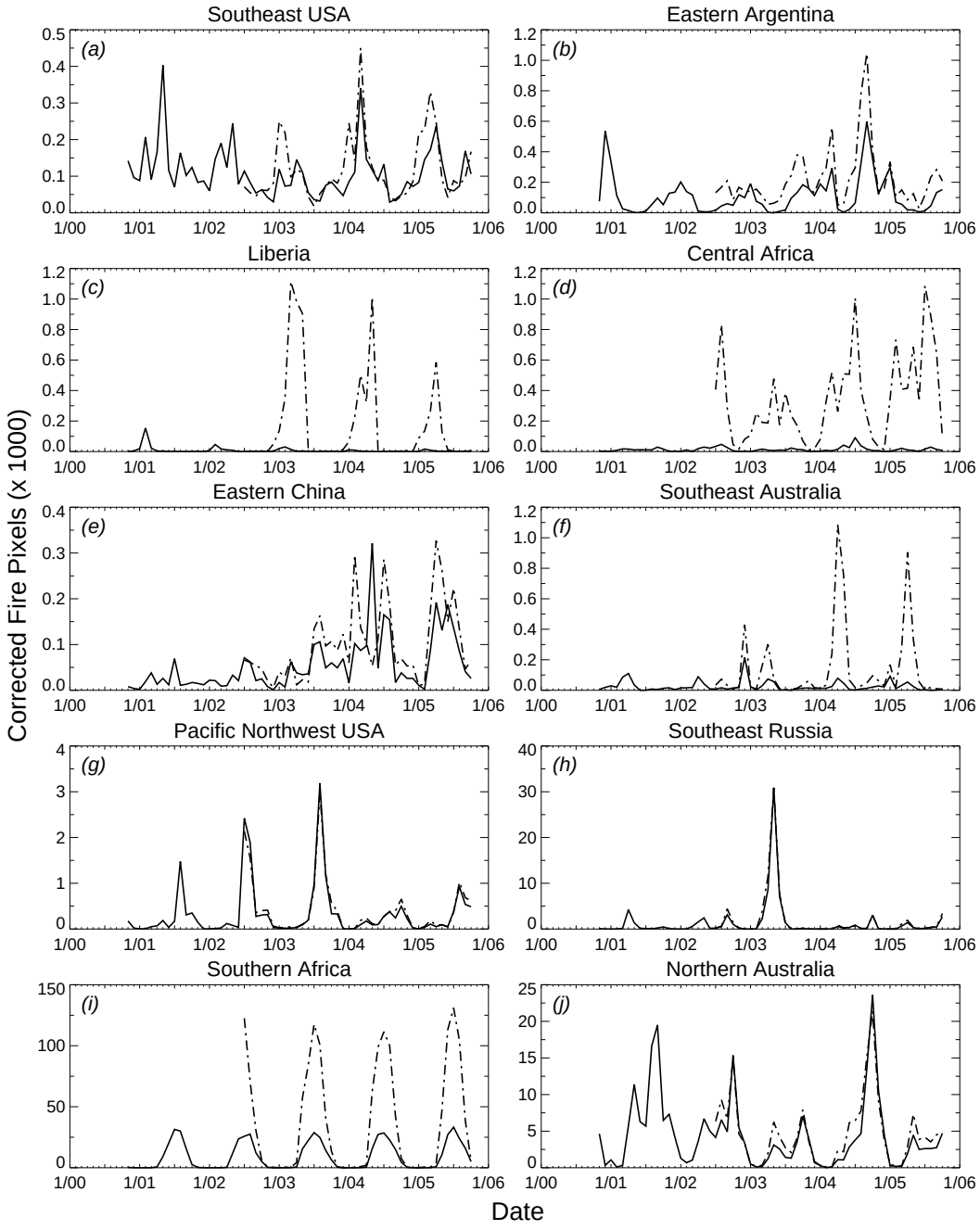

Figure 4.8: Time series of Terra (solid line) and Aqua (dashed line) overpass-corrected fire pixel counts for ten different regions. Top six panels (a-f) are from regions in which the time series have a low cross-correlation, while bottom four panels (g-j) are from regions in which the time series have a very high cross-correlation. Geographic boundaries of the different regions are listed in Table 4.1. The horizontal axis spans the time period from January 2000 through January 2006 (1/00 = January 2000, 1/01 = January 2001, etc.).

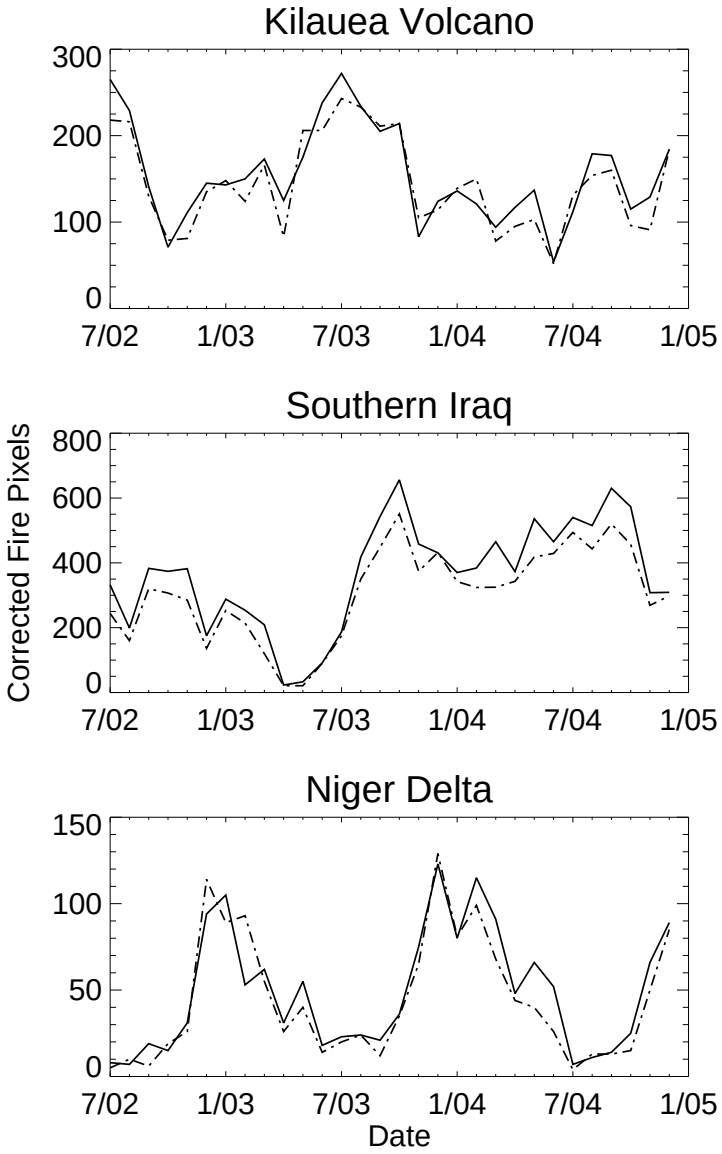

Figure 4.9: July 2002 – October 2005 time series of Terra (solid line) and Aqua (dashed line) overpass-corrected fire pixel counts for three different regions containing persistent, non-vegetation-fire hot spots. Top panel: Kilauea volcano, Hawaii (approx. 19.4°N, 155.1°W). Middle panel: gas flares in southern Iraq (approx. 30.5°N, 47.4°E). Bottom panel: gas flares in oil fields of the Niger Delta, Nigeria (approx. 4.8°N, 5.7°E). (Note that the time series shown here are shorter than those in Figure 4.8. This is because we used a slightly older version of the CMG product, which did not have persistent hot spots removed, for this part of the analysis. The overpass-corrected fire pixel counts were otherwise identical.)

4.7 Impact of Cloud Correction

As mentioned in Section 4.2.1, the additional cloud correction applied to the overpass-corrected monthly fire pixel counts is based on the assumption that the number of fire pixels per unit area within both clear and cloud-obscured areas is identical. Beneath raining clouds this assumption is unreasonable, and the correction in Equation 4.3 is likely to overestimate the true extent of fire activity. In the absence of a correction for variable cloud cover, however, the monthly fire-count time series could potentially contain significant artificial drops during periods of increased cloudiness. To test the sensitivity of the results in Sections 4.4 and 4.6 to variations in cloud cover, we repeated our analyses with overpass-corrected fire-pixel counts containing the additional cloud correction (i.e., N''_{fire} vs. N'_{fire}). At the 0.5° monthly spatial and temporal scales used in this study, we found no significant differences in fire seasonality (peak month and season length) following application of the cloud correction. While the correction did noticeably increase the absolute number of fire pixels in each grid cell (by about 20%), the relative distribution of fire activity was essentially unchanged.

4.8 Conclusion

In this study we have used the 0.5° monthly Terra MODIS CMG fire product from November 2000 through October 2005 to analyze the global distribution of biomass burning. Using these data, we derived five different metrics characterizing different

aspects of large-scale fire behavior. Among these metrics we considered the mean fire radiative power (FRP) for the first time at a global scale. Low FRP was associated with areas of extensive cropland regardless of location. In the tropics and much of the sub-tropics, low FRP was also associated with more heavily forested areas, while higher FRP was associated with areas having more herbaceous vegetation. In boreal regions this trend was reversed, with higher FRP occurring in areas having more tree cover and less herbaceous vegetation. Although not explored in the present work, the FRP is an important potential link to producing pyrogenic emissions estimates.

At the global scale, July, August, and September are the peak months of fire occurrence, with fires in both the northern and southern hemispheres, while February is least often the month of peak fire occurrence. For every month there is fire activity somewhere on the planet.

Globally, the duration of the annual fire season usually varies between 2 and 6 months and is, in the tropics, highly constrained by the duration of the dry season. Exceptionally long fire seasons of $\sim$10 months occur in central and southern Brazil and the southeastern United States. The duration of the fire season at boreal latitudes is uniformly short at 1-3 months.

The lowest interannual variability, as indicated by the highest 12-month lagged temporal autocorrelation, was observed in the savannas of Africa, both in the sudanian and sahelian zones north of the Equator and in central and southern Africa between 5°S and 20°S. This characteristically strong annual periodicity is caused by a combination of widespread human-induced burning for land maintenance purposes and low

interannual variability in rainfall during the study period. Regions of significant interannual variability (and significantly less periodicity) include the United States, southwest China, Siberia, Canada, and most of Australia.

By combining three years of Terra and Aqua MODIS observations we were able to identify regions having a pronounced diurnal fire cycle. We found that this cycle is extremely strong, at least between the mid-morning and early afternoon Terra and Aqua overpass, in the broadleaf forests of West Africa, Central Africa, Borneo, and Brazil, and cropland in southeast Australia. In these regions virtually all fires are detected exclusively during the afternoon Aqua overpass. The diurnal fire cycle was weaker but still significant in southern and sub-Saharan Africa (with exceptions in Sudan and Ethiopia), Southeast Asia, Indonesia, and parts of southwest Australia and Brazil. The cycle appears to be insignificant in northern and western Australia, central Eurasia, and the boreal forests of Siberia and North America, but of course we have sampled only a few points on a curve that might change substantially between satellite overpasses. Further work with data from the VIRS, on board the precessing TRMM satellite, and the newer generation of geostationary satellites is desirable to more fully understand this cycle. Implicit in any approach using satellite data is the need for a better understanding of the fire monitoring capabilities of specific sensors which result from the physical characteristics of the sensor itself, the fire detection (and characterization) algorithms used with each sensor, and the orbital characteristics of the satellite platform on which the sensor resides.

We examined the consistency of the fire time series recorded by the Terra and Aqua

MODIS instruments and found that, in most areas, the month of peak burning and fire season length observed by each were in good agreement. The largest discrepancies in seasonality uniformly occurred in tropical rainforests, and are the result of an extremely strong diurnal fire cycle that exists in this ecosystem.

The individual spatial and temporal metrics used in our analysis quantify different aspects of fire behavior at the global scale. Together they can be used to quantitatively monitor changes in fire behavior at a global scale . Additional insight could potentially be afforded by combining these metrics into unique classes of distinct fire characteristics. In many respects, the set of such classes would be the "satellite analog" of the ecological concept of *fire regime*, a semi-quantitative summary of fire seasonality, fire type (e.g. surface, crown), and fire return interval [Whelan, 1995]. The satellite data record, in this case five years, is clearly too short to address the full range of global fire return intervals. A more pragmatic application of such a classification would be to stratify the land surface into regions of homogeneous fire behavior, and thus simplify the parameterization of fire-related variables in global emissions, transport, and biogeophysical models [e.g., Streets et al., 2003, Arellano et al., 2004]. Earlier attempts to identify satellite-based fire regimes have been made by Dwyer et al. [1999] and Clerici et al. [2004]. using comparatively short records (= 1 yr) of fire observations. Future work with the full MODIS time series, including the fire radiative power, should contribute to these efforts.

While the MODIS CMG fire product provides useful information about the spatial and temporal dynamics of global fire activity, the distribution of fire activity within

different land cover types, and fire intensity (via the FRP), it is important to keep the inherent limitations of this data set in mind. First, the fundamental unit of observation – the "fire pixel" – doesn't necessarily correspond to a single fire, but indicates instead that one or more fires, or portions of larger fires, are contained within the pixel at the time of the satellite overpass. Second, the data set captures only a subset of fires since not every fire is detected, generally because of limitations in the instrument and detection algorithm, obscuration by clouds, or the limited diurnal sampling afforded by the satellite orbit. Third, the number of fire pixels observed within a grid cell is not necessarily indicative of the total area burned within the grid cell. While it is not uncommon to assume that burned area is proportional to counts of fire pixels, this can lead to unreliable estimates of burned area [Eva and Lambin, 1998, Kasischke et al., 2003]. Use of additional fire-pixel clustering information and ancillary vegetation data can, however, improve the quality of such estimates (see Chapter 6).

Chapter 5

Characterization of the Tropical Diurnal Fire Cycle

5.1 Introduction

The demand for improved information on regional and global fire activity in the context of land use and land cover change, ecosystem disturbance, climate modeling, and natural hazards has generated considerable interest in obtaining reliable fire-related information from spaceborne sensors. A number of satellite-based fire data sets have consequently been produced over the past decade. These include the Advanced Very High Resolution Radiometer (AVHRR) global fire product [Stroppiana et al., 2000b], the Along-Track Scanning Radiometer (ATSR) nighttime fire product [Arino and Rosaz, 1999], the Visible and Infrared Scanner (VIRS) monthly fire product [Giglio et al., 2003b], the Moderate Resolution Imaging Spectroradiometer (MODIS) global fire product [Justice et al., 2002], the Geostationary Operational Environmental Satellite (GOES) Wildfire Automated Biomass Burning Algorithm (WF_ABBA) fire

product [Prins et al., 1998], and the Defense Meteorological Satellite Program (DMSP) Operational Linescan System (OLS) fire product [Elvidge et al., 1996]. An important difference among these sensors is that each provides a different sampling of the *diurnal fire cycle*, i.e. the variation in fire activity with respect to the local time of day. The ATSR and OLS, for example, are restricted to nighttime fire detection, while the Terra and Aqua MODIS instruments sample morning and early afternoon fires, respectively. Any meaningful intercomparison of fire activity across sensors must take these sampling differences into consideration. Similarly, any fusion of active fire observations from multiple sensors requires consideration of the diurnal fire cycle.

Knowledge of the diurnal fire cycle should also help improve our understanding of land use and land cover change. Different types of burning (agricultural waste, lightning-induced, land use, prescribed burns, etc.) are thought to have different diurnal fire signatures. A more utilitarian application would be to facilitate the use of historical AVHRR active fire data sets. The local overpass time of each of the NOAA platforms gradually drifted following their launch [Csiszar et al., 2003], and is likely to have introduced significant biases in the long-term AVHRR fire record. Knowledge of the diurnal fire cycle might allow the normalization of different AVHRR active fire data sets to a consistent point in this cycle.

In this chapter, I characterize the diurnal fire cycle in the tropics and sub-tropics using observations made with the Tropical Rainfall Measuring Mission (TRMM) VIRS sensor, supplemented with fire data from the Terra MODIS instrument. In Section 5.2, I briefly survey previous remote-sensing-based studies of the diurnal fire cycle.

Section 5.3 contains a description of the input data used in this study. A brief discussion of the sampling characteristics of the VIRS instrument is provided in Section 5.4. In Section 5.5, I describe a methodology for extracting the diurnal fire cycle, with an emphasis placed on bias sources and the mitigation of these biases. Results are presented, on a regional basis, in Section 5.6. Finally, in Section 5.8, I discuss the implications of these findings within the larger context of long-term global fire monitoring.

5.2 Previous work

Both anecdotal evidence and regional satellite-based studies have established that a diurnal burning cycle exists in Africa and South America. Primary examples include the following.

(1) Prins and Menzel [1992] used observations from the Geostationary Operational Environmental Satellite (GOES) Visible Infrared Spin Scan Radiometer Atmospheric Sounder (VAS) to monitor biomass burning in South America. The VAS has two channels of primary importance to fire detection: a 3.9 μm channel having 13.8 km $\times$ 13.8 km spatial resolution, and an 11.2 μm channel having 6.9 km $\times$ 6.9 km spatial resolution at the subsatellite point. The authors examined the diurnal variation in fire activity as measured by the absolute number of fire pixels detected in VAS imagery acquired on 14 August 1983 at 12:31, 15:31, 18:31, and 21:31 UTC, and note a strong diurnal variation in detected fire pixels, with the maximum occurring at 15:31 UTC

(12:31 local time) and the minimum at 21:31 UTC (18:31 local time).

(2) Langaas [1992] used a field study employing 26 foresters in The Gambia to survey local fire activity at the four NOAA-9 and NOAA-11 overpass times (02:30, 08:30, 14:30, and 20:30 local time) each day over a two week period from 7-20 March 1988. The peak in number of active fires occurred at 14:30, with 8.5 times the number of fires that were observed at the 02:30 minimum. Langaas also used NOAA-10 and NOAA-11 AVHRR data acquired at 20:30 and 02:30, respectively, to identify active fires in Senegal and The Gambia for eight dates in December 1989 and March 1990. He reported that $\sim$2.7 times as many fire pixels were recorded during the 20:30 overpass.

(3) Cahoon et al. [1992] examined the temporal and spatial distribution of fires in Africa during 1986 and 1987 with nighttime OLS data. They concluded, contrary to their expectations, that a strong diurnal burning cycle did not exist because so many fires were detected in the nighttime imagery. In a subsequent letter, Langaas [1993a] questioned this conclusion based on earlier work using satellite imagery and field observations [Langaas, 1992].

(4) Prins and Menzel [1994] used five days of GOES-7 VAS observations acquired between 31 August and 7 September 1983 at 12:30, 15:30, and 18:30 UTC to examine the diurnal fire cycle in South America. In addition to using the VAS to detect active fires, Prins and Menzel estimated the average temperature and instantaneous sub-pixel area within each fire pixel using the technique of Dozier [1981] and Matson and Dozier [1981]. By summing these sub-pixel areas within each VAS image, Prins and Menzel found the peak in total instantaneous fire area occurred at 15:30 UTC, corresponding to

a local time of approximately 12:30. Note that each of the VAS images spanned more than 30° degrees in longitude, meaning that the local solar time varied by more than two hours across each image.

(5) Menzel and Prins [1996] used observations from the GOES-8 Imager to quantify the diurnal fire cycle during the week of 5-11 September 1994. This instrument, called simply Imager, was a successor to the VAS with an improved spatial resolution of 4 km for both its 3.9 and 10.7 μm channels. Using observations spaced three hours apart at 12:00, 15:00, 18:00, and 21:00 UTC, Menzel and Prins found the peak of burning to occur at 18:00 UTC. The authors note that this result differs from their earlier findings obtained with the lower-resolution GOES-7 VAS for the 1983 burning season [Prins and Menzel, 1994].

(6) Eva and Lambin [1998] examined the diurnal burning cycle in the Central African Republic (CAR) using one month of AVHRR LAC data acquired between 22 December 1993 and 27 January 1994. The authors exploited the fact that the width of the AVHRR swath caused significant overlap to occur between consecutive orbits, allowing a portion of the diurnal cycle to be sampled. They considered two land cover classes within CAR, open savanna and woodland/agriculture, and found that the peak in burning took place in the early afternoon for both classes. Early morning fires were confined to open savanna. The authors note that restricting fire observations to nighttime satellite overpasses can severely underestimate fire activity, and that, within their region of study, nighttime fires exhibit a different spatial distribution than daytime fires.

(7) Pack et al. [2000] used data from the constellation of geosynchronous Defense Support Program (DSP) infrared surveillance satellites to monitor biomass burning in southern Africa. These satellites, which were designed to detect rocket launches and nuclear explosions, image almost the entire terrestrial surface at the astounding rate of once every ten seconds. Using one day of observations acquired on 3 July 1992, Pack et al. found a strong southern African diurnal fire cycle having a peak in total fire intensity around 12:00 UTC, corresponding to 14:00 local time.

5.3 Data

We used the Giglio et al. [2003b] gridded daily VIRS fire product, which contains information about individual VIRS swaths, on a daily basis, at 0.5° spatial resolution. This information includes counts of fire pixels, cloud pixels, missing data pixels, etc., acquisition time, and fraction of the VIRS swath overlapping each grid cell for each overpass. This data set spans more than eight continuous years from late December 1997 to December 2005. A matching data set consisting of 0.5° gridded daily VIRS reflectance, brightness temperature, and sun angle statistics was prepared for the same time period.

The source of MODIS fire data was the “Collection 4” 8-day Terra MODIS Climate Modeling Grid (CMG) fire product having 0.5° spatial resolution (“MOD14C8H”). The MOD14C8H archive of high quality data begins in November 2000. The 8-day product provides sufficient temporal resolution for the present work while avoiding artifacts

present in the daily MODIS time series arising from biases in viewing geometry.

Additional MODIS products were used as a source of information about global land cover. The Level 3 MODIS Vegetation Continuous Fields (VCF) products [Hansen et al., 2003] provided tree, herbaceous, and bare ground fractions at 500-m spatial resolution. Land cover types based on the Hansen et al. [2000] classification scheme were obtained from the Level 3, 96-day Land Cover product ("MOD12Q1") at 1-km resolution [Friedl et al., 2002].

5.4 VIRS and MODIS sampling characteristics

5.4.1 VIRS

The TRMM satellite was originally placed in a 350-km circular precessing orbit to permit observation of the well-documented diurnal rainfall cycle [e.g., Wallace, 1975, Hamilton, 1981, Desbois et al., 1989]. The TRMM orbit, combined with the original 720 km VIRS swath, yields roughly two VIRS observations (spaced about 12 h apart) every other day at equatorial latitudes, and two VIRS observations each day at temperate latitudes. The pattern of the local overpass times is dependent on latitude. Representative examples at three different locations are shown in Fig. 5.1. In August 2001 the TRMM orbit was boosted to 402.5 km, increasing the VIRS swath width to 830 km. This change did not significantly alter the general sampling trends described for the pre-boost orbit.

5.4.2 MODIS

The polar orbiting, sun-synchronous Terra satellite provides daily MODIS overpasses at 10:30 and 22:30 local time at each point along the Equator. MODIS fire observations are used in this study to provide a time series of fire activity sampled at comparatively fixed times within the diurnal fire cycle.

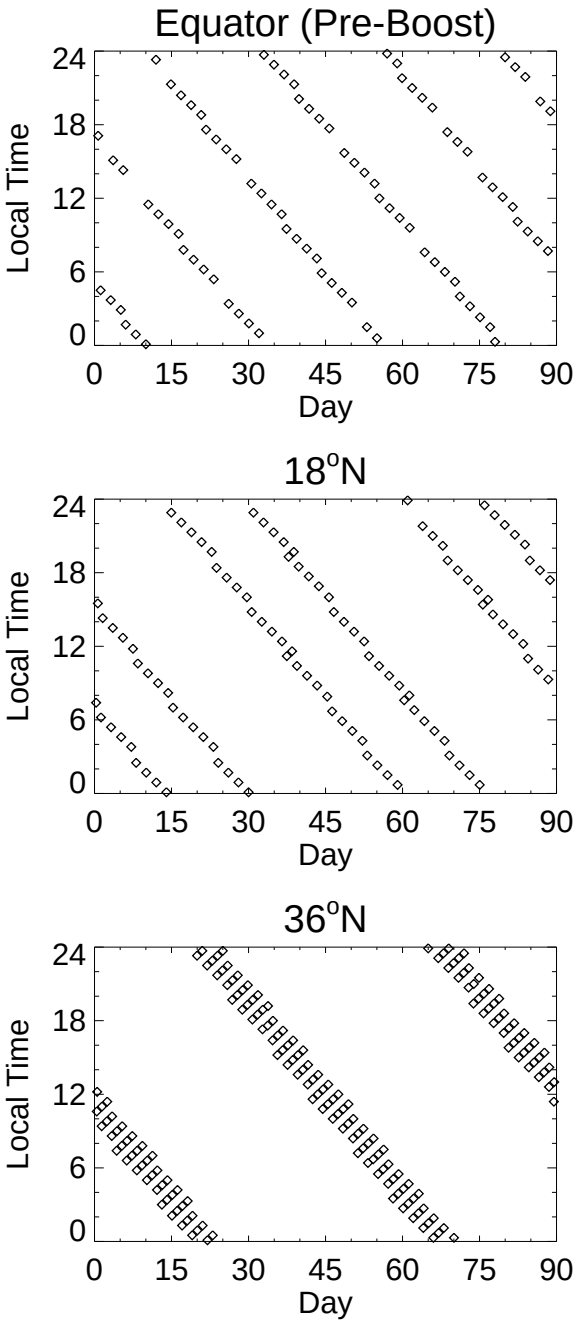

Figure 5.1: Local time of VIRS overpass during a three-month period (January-March 1998) at three different latitudes, prior to the TRMM orbit boost: Equator (top), 18°N (center), and 36°N (bottom).

5.5 Method

An obvious approach for detecting a diurnal fire cycle would be to count active fires in VIRS imagery, and assign each fire pixel into the particular local hour bin during which it was observed. After repeating this process over a specified time period to achieve a larger statistical sample, one would have an estimate of the mean diurnal fire cycle. In practice, however, one must take considerable care to avoid multiple error sources that will contaminate diurnal cycles derived in this fashion. These include both systematic and random error sources. The former category includes *detection bias*, *false alarm bias*, *cloud bias*, and *seasonal bias*, and the latter category consists of *sampling error*.

5.5.1 Error sources

5.5.1.1 Detection bias

The probability of detecting a given fire varies with time of day. Most significantly, the probability is greatly reduced when the Sun is directly, or almost directly, overhead in some biomes [Giglio et al., 1999, 2003b]. Failure to account for this bias can cause artificial “dips” in the resulting diurnal fire cycle located near local noon, the time of day at which fire detection capability is usually at a minimum for the AVHRR and VIRS instruments.

5.5.1.2 False alarm bias

In addition to detecting fires, fire detection algorithms produce false alarms. The rate at which these false alarms occur is a function of different environmental variables, many of which are related to time of day. Although the exact rate is dependent upon the particular algorithm and sensor, the general trend is that false alarms are more likely over hot, reflective surfaces at small solar zenith angles [Giglio et al., 1999].

5.5.1.3 Cloud bias

The presence of thick clouds within a scene will prevent VIRS from imaging the actual land surface. Those active fires obscured by clouds will therefore not be detected. The amount of cloud cover itself exhibits a diurnal cycle [e.g., Desbois et al., 1989, Thiao and Turpeinen, 1992], and the effect of this independent cycle should be considered when extracting the diurnal fire cycle. Cloud bias is of course not restricted to the VIRS, and in fact impacts any spaceborne optical sensor used for fire monitoring.

5.5.1.4 Sampling error and seasonal bias

Setting aside for a moment the fact that VIRS overpasses are irregularly spaced in time, the average VIRS equatorial sampling rate is one sample per day. This corresponds to a Nyquist critical frequency of $\nu_{\mathrm{N}} = 0.5$ cycles/day, which is below the 1-cycle/day fundamental frequency of any periodic diurnal signal and all higher frequency harmonics. This could introduce aliasing into diurnal cycles derived from VIRS observations. However, if one can assume that the diurnal fire cycle does not change

substantially over the course of the fire season, we can accumulate VIRS observations over multiple satellite precession periods, thereby sampling different local hours of the diurnal cycle at a much higher effective sampling rate. Indeed, such a sampling strategy has been a common approach for exploiting observations from precessing satellites [Salby and Callaghan, 1997] such as the Upper Atmospheric Research Satellite (UARS) and the Earth Radiation Budget Satellite (ERBS).

There are, however, complications in using such an approach. First, the number of samples for some of the local time "bins" (e.g., 1-hour intervals) might be very small or even zero, thus failing to adequately sample the natural variability of the diurnal signal [Salby and Callaghan, 1997]. To increase the number of observations available at each local hour, it therefore becomes necessary to accumulate observations over a larger number of precession periods, but this can introduce biases if the seasonal signal is not stationary. Using an example in the context of the present work, those local hours that happen to have been observed during time periods of greater *seasonal* fire activity will be contaminated with a surplus of fires that are unrelated to the diurnal fire cycle. Secondly, the spatial sampling of the VIRS instrument is also tightly coupled to the orbital characteristics of the TRMM satellite, and care must be taken to avoid potential biases arising from spatially inconsistent sampling. This issue was examined by Lin et al. [2002] and Negri et al. [2002] for the Precipitation Radar (PR), TRMM Microwave Imager (TMI), and VIRS sensors resident on the TRMM satellite.

5.5.2 Overview

Characterization of the diurnal fire cycle with any satellite-based imaging sensor will, by necessity, involve counting or averaging pixels within spatial patches, or regions, of finite extent. In defining the locations and extent of these regions, several important, and sometimes conflicting, constraints must be met. Recognition of these constraints is especially important in the case of VIRS since its diurnal sampling characteristics, which arise from the interplay of the precessing TRMM orbit and the $\sim$800 km VIRS swath, operate independently of the spatial and temporal scales over which tropical fire activity should be monitored to provide meaningful results. Ultimately a combination of spatial and temporal averaging of VIRS observations will be necessary; the constraints dictating the scales over which this averaging must be performed are discussed in Section 5.5.3.

5.5.3 Selection of regions and time periods

The first constraint in the selection of spatial patches is that they must be sufficiently large to accumulate valid statistical samples of fire observations during the time period being considered. If the patches are made too small, sampling errors can become too large because an insufficient number of observations are available. Within the present study we simultaneously have the critical temporal requirement to adequately sample the different local times of the diurnal cycle. This issue was examined by Lin et al. [2002], who found that TRMM sampling of the seasonal-mean diurnal cycles of

precipitation and outgoing long-wave radiation was inadequate with $2.25^\circ \times 2.25^\circ$ grid cells. By averaging over larger areas (assuming the diurnal cycle is fairly uniform), or using longer time series of observations, however, the authors found that satisfactory sampling could be achieved. Subsequent work by Negri et al. [2002] demonstrated that sampling errors in diurnal rain-rate estimates derived from PR observations (and, to a lesser extent, TMI observations) remained significant even in larger 5° grid cells averaged over several years.

A second but conflicting constraint is that the extent of the spatial patches be kept relatively small to allow regional differences in diurnal fire activity to be captured. Large spatial patches can potentially lead to the oversight of important regional differences by smearing together different regional diurnal cycles. In particular, one should avoid encompassing multiple fire regimes within a region since differences in the diurnal fire cycle are expected across different fire regimes [Eva and Lambin, 1998].

The above constraints were satisfied in two ways. First, in conjunction with global land cover maps, climatological maps of five different spatial and temporal variables derived from five years of Terra active fire observations Giglio et al. [2006a] were used to stratify the tropics and sub-tropics into regions of comparatively homogeneous fire behavior. These variables were available at 0.5° spatial resolution and consisted of: mean annual fire-pixel density, calendar month of maximum fire activity, fire season duration, one-year lagged temporal autocorrelation of fire counts, and mean fire radiative power (FRP) within each 0.5° grid cell. Ultimately fifteen representative regions in the tropics and sub-tropics were selected in this manner (Fig. 5.2).

Summaries of the relevant land cover characteristics for each region are provided in Table 5.1.

The second manner in which the above constraints were satisfied was by accumulating observations from 86 months (7.2 years) of the current eight-year VIRS data archive. Observations acquired during the first eleven months of operation (December 1997 through October 1998) were excluded to prevent potential contamination from anomalous diurnal cycles that might be associated with the strong 1997-1998 El-Niño Southern Oscillation event. To avoid potential seasonal bias (Section 5.5.1.4), the 8-day Terra MODIS CMG fire product was used to demarcate an approximately stationary subset of the fire season while accumulating observations within each region. VIRS observations falling outside these periods of relative stationarity were not included in the subsequent analysis.

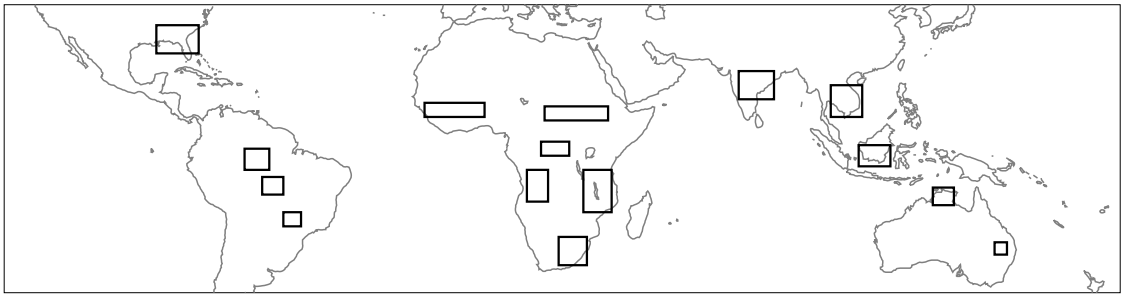

Figure 5.2: Regions for which the mean diurnal fire cycle was extracted in this study.

Table 5.1: Predominant Hansen et al. [2000] land cover types in which VIRS fire pixels were detected for the 15 regions used in this study. For each region these are listed in order of decreasing frequency.

Region	Characteristics
Brazil: Rainforest	Evergreen broadleaf forest.
Brazil: Deforestation	Evergreen broadleaf forest, savannas.
Brazil: Cropland	Croplands, savannas, woody savannas.
Eastern Sahel	Savannas, woody savannas, grasslands.
Western Sahel	Woody savannas, savannas.
Central Africa	Evergreen broadleaf forest.
Southern Africa West	Woody savannas, savannas, deciduous broadleaf forest, evergreen broadleaf forest.
Southern Africa East	Woody savannas, savannas.
South Africa	Savannas, open shrublands, woody savannas, croplands, grasslands.
India	Woody savannas, croplands, evergreen broadleaf forest.
Southeast Asia	Evergreen broadleaf forest, croplands, woody savannas, savannas.
Southern Borneo	Evergreen broadleaf forest.
Northern Australia	Woody savannas, savannas, open shrublands.
Eastern Australia	Open shrublands, woody savannas.
Southeast USA	Heterogeneous mixture of croplands, woody savannas, mixed forests, deciduous broadleaf forest, and evergreen broadleaf forest.

5.5.4 Extraction of the diurnal cycle

As mentioned in Section 5.3, the basic observations from which the diurnal fire cycle will be extracted are individual VIRS overpasses distributed into 0.5° grid cells. For the observation of a grid cell at UTC time t and location (i, j), denote the number of fire pixels within the grid cell as $N_{\text{fire}}(i, j, t)$, the number of cloud pixels over land as $N_{\text{cloud}}(i, j, t)$, and the total number of land pixels as $N_{\text{land}}(i, j, t)$. Next we define the mean fire-pixel fraction f for individual observations:

$$f(i, j, t) = N_{\text{fire}}(i, j, t)/N_{\text{land}}(i, j, t). \tag{5.1}$$

Individual grid-cell observations are assigned to the local hour bin τ, where τ is simply the integer part of the local solar hour ($\tau = 0, 1, 2, \ldots, 23$). The subsequent discussion will make use of the following regional pixel totals accumulated for each local hour bin:

$$F_\tau = \sum_{i,j \in R} \sum_{t \in \tau} N_{\text{fire}}(i, j, t) \tag{5.2}$$

$$C_\tau = \sum_{i,j \in R} \sum_{t \in \tau} N_{\text{cloud}}(i, j, t) \tag{5.3}$$

$$L_\tau = \sum_{i,j \in R} \sum_{t \in \tau} N_{\text{land}}(i, j, t). \tag{5.4}$$

Here the notation $i, j \in R$ indicates that the first summation is restricted to only those grid cells comprising the R'th region, and the notation $t \in \tau$ indicates that the second summation is to be restricted to those observations acquired at UTC time t which fall within the τ'th local hour bin. Although not explicitly indicated, observations are selected from calendar dates spanning the fire season for each region, as discussed in

Section 5.5.3.

At this point it is straightforward to define the "naive" fraction of VIRS pixels containing fires in each local hour bin, f_τ, as the weighted average of fire pixel fractions from individual grid cells:

$$f_\tau = \frac{\sum\limits_{i,j \in R} \sum\limits_{t \in \tau} N_{\text{land}}(i,j,t) f(i,j,t)}{L_\tau} = \frac{F_\tau}{L_\tau}. \tag{5.5}$$

The weighting in Eq. (5.5) is needed to ensure that those observations overlapping a larger fraction of the grid cell are given proportionally greater importance than observations representative of only a small portion of the grid cell. The weighted variance in f_τ, which will be important in establishing uncertainties, is then given by

$$\sigma_\tau^2 = \frac{\sum\limits_{i,j \in R} \sum\limits_{t \in \tau} N_{\text{land}}(i,j,t) \left[f(i,j,t) - f_\tau \right]^2}{L_\tau - 1}. \tag{5.6}$$

Were it reasonable to neglect the remaining bias sources discussed in Section 5.5.1 (cloud bias, detection bias, and false alarm bias), Eq. (5.5) would directly represent the diurnal fire cycle. Such an assumption is generally not reasonable, however, at least not for all three of these potential bias-error sources, hence it is necessary to explicitly incorporate additional corrections into Eq. (5.5). We will denote the corrected form of f_τ as f_τ^*.

To correct for cloud bias, we assume that the fraction of cloud-obscured pixels containing a fire is the same as the fraction of cloud-free pixels in that were classified as fire pixels. While this assumption is generally invalid over large heterogeneous areas and arbitrary time periods, it is much more reasonable in this case since the regions

used here are comparatively small and homogeneous, and the time periods are restricted to each region's fire season. To affect the cloud correction, f_τ must be divided by the fraction of pixels within each local hour bin that were unobscured by cloud cover. This fraction is equivalent to the quantity $1 - \mathrm{MCF}_\tau$, where $\mathrm{MCF}_\tau = C_\tau / L_\tau$ is the mean cloud fraction within each local hour bin. The MCF represents the average probability that a VIRS observation will be obscured by cloud cover during the region R fire season.

Depending on the specific sensor and fire detection algorithm employed, the need to include corrections for detection bias and false alarm bias may be required. Here we introduce two factors to perform these corrections. The first, D_τ, where $D_\tau \geq 1$, corrects for detection bias by potentially increasing the apparent number of fire pixels detected during local hour bin τ, compensating for the variation in fire detectability as a function of local time. The second factor, Φ_τ, where $\Phi_\tau \leq 1$, potentially decreases the apparent number of fire pixels in local hour bin τ to compensate for potentially higher false alarm rates near mid-day.

It will prove convenient at this point to introduce an additional factor of β which is simply a normalization constant applied to all local times. This factor will simplify matters later when f_τ^* is cast in the form of a probability density function; it has no effect on the relative distribution of fires detected in each local hour bin. The corrected fraction of VIRS pixels containing one or more fires within the τ'th local hour bin is

then

$$f_\tau^* = \frac{\beta D_\tau \Phi_\tau f_\tau}{1 - \mathrm{MCF}_\tau}. \tag{5.7}$$

5.5.5 Detection and false alarm bias corrections

The approach described so far has included explicit procedures for avoiding seasonal bias, minimizing sampling error, and correcting for diurnal variations in cloud cover. It remains to develop explicit forms for the detection-related correction factors D and Φ.

5.5.5.1 Detection bias correction

In formulating a detection bias correction, one must consider the individual tests of the detection algorithm. For the sake of brevity only the relevant portions of the algorithm will be discussed here; a complete description can be found in Giglio et al. [2003b].

Among other quantities, the detection algorithm uses VIRS 3.8 μm (channel 3) and 10.8 μm (channel 4) top-of-atmosphere brightness temperatures, denoted by T_3 and T_4, respectively, the difference $T_{34} \equiv T_3 - T_4$, and the top-of-atmosphere 1.6 μm (channel 2) reflectance, denoted ρ_2. The algorithm applies a series of fixed threshold tests to each candidate fire pixel, followed by a series of relative threshold (or "contextual") tests. The relative thresholds are derived from statistics of neighboring pixels within a small window centered about the candidate fire pixel. These statistics include: $T_{34\mathrm{B}}$ and $\delta_{34\mathrm{B}}$, the respective mean and mean absolute deviation of $T_3 - T_4$ for the neighboring (or "background") pixels; and $T_{4\mathrm{B}}$ and $\delta_{4\mathrm{B}}$, the respective mean and mean absolute deviation of T_4 for the background pixels.

For daytime scenes, a pixel is identified as a fire pixel (i.e., contains one or more sub-pixel active fires) if the following conditions are satisfied:

$$T_3 > 310\,\mathrm{K} \tag{5.8}$$

$$T_{34} > 6\,\mathrm{K} \tag{5.9}$$

$$\rho_2 < 0.32 \tag{5.10}$$

$$T_{34} > T_{34\mathrm{B}} + 3.5\,\delta_{34\mathrm{B}} \tag{5.11}$$

$$T_{34} > T_{34\mathrm{B}} + 6\,\mathrm{K} \tag{5.12}$$

$$T_4 > T_{4\mathrm{B}} + \delta_{4\mathrm{B}} - 1.5\,\mathrm{K}. \tag{5.13}$$

If any condition is not satisfied, the pixel is classified as a non-fire pixel. In practice the absolute threshold tests (5.8)–(5.10) are performed before the contextual tests (5.11)–(5.13) to avoid needlessly computing the background statistics in the event the simpler (and computationally much faster) threshold tests are not unanimously satisfied.

The need for the detection bias qualitatively described in Section 5.5.1.1 arises because certain situations render it impossible to satisfy some of the above tests, no matter how large or intense a fire may be. This results in “blind spots” in which the algorithm (or instrument) is completely incapable of detecting fires. The most critical (and most frequent) mechanisms leading to this blindness are: 1) high channel 2 reflectance and 2) saturation of channel 3. In the context of the present study, it is necessary to know the relative degree to which this blindness occurs with respect to the time of day.

To proceed, we will estimate the likelihood of one or more of the above tests failing due to high reflectance or saturation. Of the three absolute threshold tests, only conditions (5.9) and (5.10) can lead to total blindness. For test (5.9) this can occur when T_3 saturates at 321.2 K, a routine occurrence for pixels containing active fires. If the surface is sufficiently warm during some period of the day, T_4 will exceed 315.2 K and it will become impossible to satisfy the 6 K minimum difference mandated by this test. Due to directional and atmospheric effects, ρ_2 also exhibits diurnal variation, with the maximum reflectance usually occurring when the Sun is highest in the sky. Consequently, test (5.10) will also fail at different rates throughout the day for higher-reflectance candidate fire pixels. Using the statistical reflectance and brightness temperature data set mentioned in Section 5.3, it is a simple matter to estimate the frequency with which the threshold tests (5.9) and (5.10) prevent fire detection.

It remains to estimate the likelihood of the contextual tests hindering fire detection as a result of channel 3 saturation. (Saturation of channel 4 is quite rare and makes no significant contribution to detection bias.) In this respect it is tests (5.11) and (5.12) that are important. Since the latter test is somewhat simpler to deal with, we will consider it first. Contextual test (5.12) can equivalently be written as

$$T_3 - T_4 > T_{3\mathrm{B}} - T_{4\mathrm{B}} + 6\,\mathrm{K}. \tag{5.14}$$

For most tropical fires the 11 μm brightness temperature (T_4) is not significantly elevated above that of the background; in the majority of cases $T_4 \approx T_{4\mathrm{B}} + 1\,\mathrm{K}$. To

good approximation, therefore, the inequality in (5.14) may be written

$$T_3 > T_{3\mathrm{B}} + 7\,\mathrm{K}. \tag{5.15}$$

The "blind spot" of condition (5.15) comes about when T_3 for the candidate fire pixel reaches saturation at 321.2 K over a warm and/or bright daytime surface. Under these conditions, $T_{3\mathrm{B}}$ also reaches (or nearly reaches) saturation, so that $T_3 \approx T_{3\mathrm{B}}$, i.e. no contrast exists between the fire pixel and the non-fire background, and inequality (5.15) cannot be satisfied. Given saturation of channel 3 for a candidate fire pixel, contextual test (5.12) will consequently always fail when

$$T_{3\mathrm{B}} \geq 314.2\,\mathrm{K}. \tag{5.16}$$

Applying a similar argument to the first contextual test (5.11), one finds that, given saturation of channel 3 for a candidate fire pixel, the blind spot for this test arises when

$$T_{3\mathrm{B}} \geq 320.2\,\mathrm{K} - 3.5\,\delta_{34\mathrm{B}}. \tag{5.17}$$

In practice, $\delta_{34\mathrm{B}}$ only rarely exceeds 1.5 K (Fig. 5.3), and condition (5.17) effectively becomes a redundant, weaker version of condition (5.16). This is particularly true in hot, arid environments, where saturation of channel 3 occurs often, since abrupt discontinuities in neither surface temperature nor surface emissivity (which would generally arise from abrupt discontinuities in vegetation cover or soil type) are common. A correction for the saturation-induced failure of contextual test (5.12), therefore, will generally obviate the need for a separate correction for the saturation-induced failure of contextual test (5.11).

The correction factor can be written in terms of the conditional probabilities that the relevant potential fire tests will unconditionally fail, given an observation that falls within local time bin τ:

$$\begin{aligned} D_\tau &= \frac{1}{P(T_4 \leq 315.2\,\mathrm{K};\tau)} \times \frac{1}{P(\rho_2 < 0.32;\tau)} \\ &\quad \times \frac{1}{1 - P(T_{3\mathrm{B}} \geq 314.2\ \mathrm{K}, T_3 \text{ saturated};\tau)}. \end{aligned} \tag{5.18}$$

Nominally, the denominators of the three factors on the right hand side of Eq. (5.18) will have a value of unity, and D_τ will have no effect on the corrected fire-pixel fraction calculated via Eq. (5.7). As the surface becomes hotter and/or brighter, one or more of the denominators will decrease, and D_τ will correspondingly boost the number of fire pixels accumulated in the τ'th local hour bin. An example detection bias correction is shown for the western Sahel region in Fig. 5.4.

5.5.5.2 False-alarm bias correction

The correction factor Φ_τ is the fraction of fire pixels observed during each local hour bin that are actually true fire pixels. Given independent estimates of $P(\text{fire}|\text{non-fire};\tau)$, the probability a non-fire clear land pixel will be falsely identified as a fire pixel during local hour τ, the false-alarm bias correction factor can be written as

$$\Phi_\tau = \frac{F_\tau - P(\text{fire}|\text{non-fire};\tau)L_\tau}{F_\tau}. \tag{5.19}$$

While there is presently insufficient data to estimate Φ_τ on a time dependent, regional basis, earlier results reported by Giglio et al. [2003b, Tables 2 and 3] based on

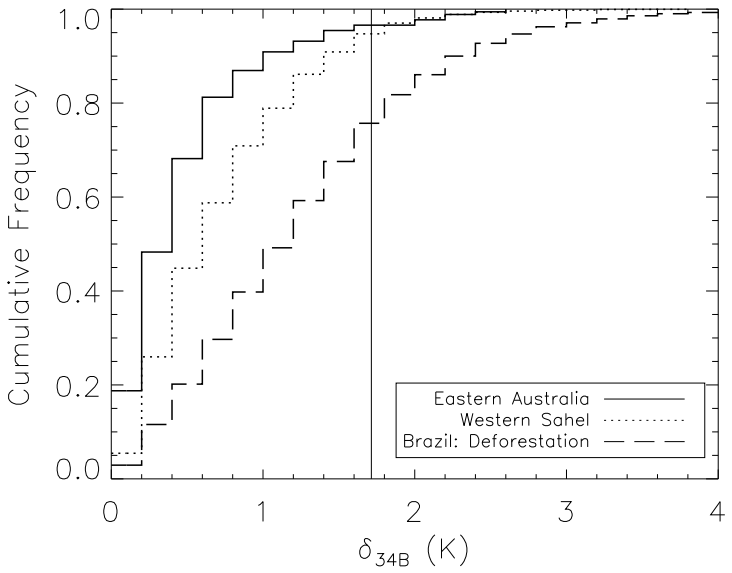

Figure 5.3: Cumulative histograms of the background $T_3 - T_4$ mean absolute deviation ($\delta_{34\mathrm{B}}$) for sample of VIRS fire pixels detected between 1 July and 31 December 2005 in three different regions. Vertical line indicates threshold below which the correction for saturation- induced failure of contextual test (5.11) is encompassed by the correction for saturation-induced failure of contextual test (5.12).

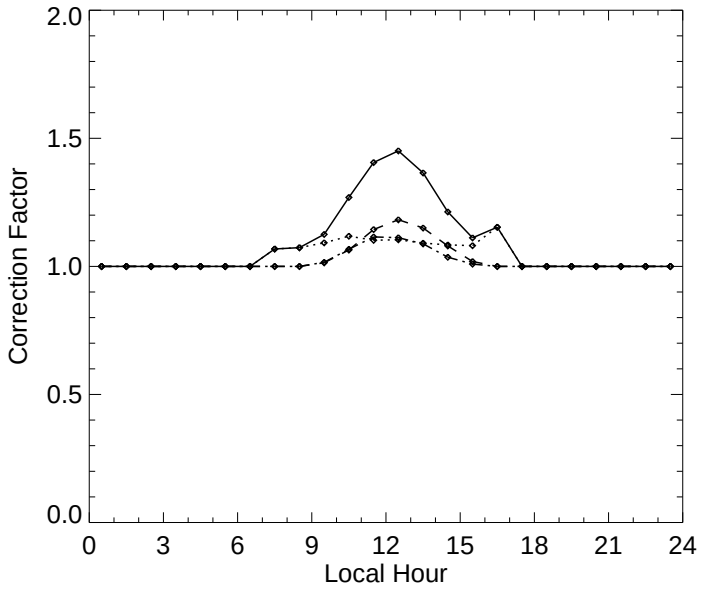

Figure 5.4: Detection bias correction (D_τ) as a function of local time (solid line) for the western Sahel region. Contributions from channel-2 reflectance correction (dotted line), T_{34} absolute threshold test correction (dashed line), and T_{34} contextual test correction (dotted-dashed line) are also shown.

representative VIRS imagery suggest average daytime and nighttime values of 0.96 and 0, respectively. False alarm bias is therefore not expected to be a significant source of error, and we consequently set $\Phi_\tau = 1$ for all τ.

5.5.6 Uncertainty in corrected diurnal fire-pixel fraction

The uncertainty in f_τ^* calculated via Eq. (5.7) arises from statistical variability of the uncorrected mean fire-pixel fraction (f_τ) and the mean cloud fraction (MCF_τ). Assuming the errors in these quantities are independent, the uncertainty in the corrected mean fire-pixel fraction, Δf_τ^*, is given by

$$\begin{aligned} \Delta f_\tau^* &= \sqrt{\left(\frac{\partial f_\tau^*}{\partial f_\tau}\Delta f_\tau\right)^2 + \left(\frac{\partial f_\tau^*}{\partial \mathrm{MCF}_\tau}\Delta \mathrm{MCF}_\tau\right)^2} \\ &= \frac{\beta D_\tau \Phi_\tau}{1-\mathrm{MCF}_\tau}\sqrt{\Delta f_\tau^2 + \left(\frac{f_\tau\,\Delta \mathrm{MCF}_\tau}{1-\mathrm{MCF}_\tau}\right)^2}. \end{aligned} \tag{5.20}$$

The uncertainties Δf_τ and $\Delta \mathrm{MCF}_\tau$ were taken to be the standard deviation of the mean of f_τ and MCF_τ, respectively.

5.6 Results

Mean diurnal fire cycles were extracted for each of the 15 regions using the procedure described in Section 5.5 and are shown in Fig. 5.5. In all regions the diurnal cycle was very prominent, with a maximum in the early- to late-afternoon and typically little or no burning between midnight and approximately 08:00 local time. As expected, the distribution of fire activity is generally skewed with a somewhat longer tail above the peak as fires continue burning into the evening. In general, only a single peak in fire activity was observed throughout the day. For the Eastern Sahel and Northern Australia regions, however, a significant secondary morning peak in fire activity was observed. A detailed analysis of the regional cycles will be deferred to Section 5.6.4.

5.6.1 Diurnal probability density functions

As an aid to the subsequent analysis, it will prove useful to represent the discrete, corrected, diurnal fire fraction f_τ^* for each region as a continuous probability density function (PDF), denoted $p^*(t)$, which describes the probability of observing a detectable fire as a function of local time t. (Note that this is a slight change from the notation of Section 5.5.4, where t was used to denote UTC time.) The skewness and overall structure of the cycles shown in Fig. 5.5 generally preclude use of the standard distribution functions appropriate for circular data [e.g., Fisher, 1995]. Instead we represent the diurnal fire PDF more generally as a Fourier series, i.e.,

$$p^*(t) = A_0 + \sum_{k=1}^{12} (A_k \cos k\omega t + B_k \sin k\omega t) \tag{5.21}$$

where the fundamental diurnal period $T = 24\,\mathrm{h}$ and $\omega = 2\pi/T \approx 0.2618\,\mathrm{rad\,h^{-1}}$ is the fundamental diurnal angular frequency. The coefficients A_k and B_k may be computed from the discrete Fourier transform of the sequence obtained from Eq. (5.7). Since $p^*(t)$ is a probability density function it follows that

$$\int_0^T p^*(t)\,\mathrm{d}t = 1, \tag{5.22}$$

which in turn dictates that $A_0 = 1/T$. The value of the constant β is set when computing the remaining coefficients A_k and B_k so as to arrange that $p^*(t)$ will satisfy Eq. (5.22) directly and eliminate the need to explicitly introduce an additional normalization step (and additional coefficients) at this point.

5.6.2 Summary distribution parameters

Having expressed the regional diurnal fire cycles as PDFs, summary distribution parameters of potential interest may now be calculated. Perhaps most obviously this would include the time of peak fire activity, $t_{\rm p}$, which was determined by a numerical search of Eq. (5.21) in the interval $[0, T)$.

Another useful summary parameter is the median, or 50'th percentile, representing the time of day by which 50% of all daily fires were detected during the previous 12 hours. For the circular PDF in Eq. (5.21), the median (t_{50}) satisfies the relationship

$$\int_{t_{50}-T/2}^{t_{50}} p^*(t)\,\mathrm{d}t = 1/2. \tag{5.23}$$

Evaluating the left hand side of Eq. (5.23) yields the transcendental equation

$$\begin{aligned} 0 \;&=\; \pi A_0 - 1/2 \\ &\quad + \omega^{-1} \sum_{k=1}^{12} k^{-1} \left[1 - (-1)^k\right] \left(A_k \sin k\omega t_{50} - B_k \cos k\omega t_{50}\right), \end{aligned} \tag{5.24}$$

which can be solved numerically for t_{50}.

Then interquartile range (IQR) will be employed as a robust measure of the spread of each diurnal PDF. More common measures include the standard deviation and the full-width-at-half-maximum (FWHM), but complications arise in the interpretation of the former with circular data [Fisher, 1995], and the latter becomes ambiguous in the presence of multiple peaks and is potentially misleading for highly skewed distributions.

By definition, $\mathrm{IQR} = t_{75} - t_{25}$, where t_{25} and t_{75} are the 25'th percentile (lower

quartile) and 75'th percentile (upper quartile), respectively, of the PDF. The IQR is readily interpretable in that 50% of the fires occurring each day will be active between the times t_{25} and t_{75}. The lower and upper quartiles can be defined in terms of the median. By definition,

$$\int_{t_{25}}^{t_{50}} p^*(t)\,\mathrm{d}t = 1/4 \tag{5.25}$$

and

$$\int_{t_{50}}^{t_{75}} p^*(t)\,\mathrm{d}t = 1/4. \tag{5.26}$$

Evaluating the left hand sides of Eqs. (5.25) and (5.26) yields the equations

$$\begin{aligned} 0 \;=\; & A_0(t_{50} - t_{25}) - 1/4 \\ & + \omega^{-1} \sum_{k=1}^{12} k^{-1} \left(A_k \sin k\omega t_{50} - B_k \cos k\omega t_{50}\right) \\ & - \omega^{-1} \sum_{k=1}^{12} k^{-1} \left(A_k \sin k\omega t_{25} - B_k \cos k\omega t_{25}\right) \end{aligned} \tag{5.27}$$

and

$$\begin{aligned} 0 \;=\; & A_0(t_{75} - t_{50}) - 1/4 \\ & + \omega^{-1} \sum_{k=1}^{12} k^{-1} \left(A_k \sin k\omega t_{75} - B_k \cos k\omega t_{75}\right) \\ & - \omega^{-1} \sum_{k=1}^{12} k^{-1} \left(A_k \sin k\omega t_{50} - B_k \cos k\omega t_{50}\right), \end{aligned} \tag{5.28}$$

which can also be solved numerically for t_{25} and t_{75}, respectively.

5.6.3 Uncertainties in distribution parameters

Uncertainties in $t_{\rm p}$, t_{50}, and the upper and lower quartiles were estimated using a Monte Carlo approach. For each region, 1000 random sequences of the corrected diurnal fire-pixel fraction [Eq. (5.7)] were generated, where each point in a sequence was drawn from a normal distribution having mean f_τ^* and standard deviation Δf_τ^*. For each random sequence, the PDF in Eq. (5.21) was refitted and new values of $t_{\rm p}$, t_{50}, t_{25}, and t_{75} were calculated, yielding 1000 samples of each parameter. The standard deviation of each collection of samples was then used as the 1-sigma uncertainty in the corresponding parameter.

Since the uncertainties in the lower and upper quartiles are not independent (both are defined in terms of the median t_{50}, and the coefficients A_k and B_k), the uncertainty in the IQR is estimated as

$$\Delta{\rm IQR} = \Delta t_{25} + \Delta t_{75}, \tag{5.29}$$

where Δt_{25} and Δt_{75} are the respective 1-sigma uncertainties in the lower and upper quartiles.

5.6.4 Regional diurnal fire cycles

The fitted diurnal fire cycles are shown in Fig. 5.5. Relevant parameters calculated from the regional PDFs are listed in Table 5.2. In all regions, the peak burning time varied between approximately 13:00 and 18:30, with fire activity peaking distinctly earlier for the heavily-forested regions. The median time of fire activity spanned a

similar range of values. The IQR, our measure of how "spread out" burning was throughout the day, ranged from a minimum of 1.3 h in Central Africa to a maximum of 5.5 h in Eastern Australia. In general, shorter periods of burning (i.e., smaller values of the IQR) were associated with greater tree cover, and vice versa (Fig. 5.6), a trend that is qualitatively consistent with the earlier findings of Eva and Lambin [1998] regarding open savanna vs. woodland/agriculture fires in the Central African Republic (Section 5.2). This phenomenon may be explained, at least in part, as follows. Within the tropics, low fractional tree cover is indicative of high herbaceous cover (as opposed to sub-tropical latitudes, for example, where low tree cover might instead reflect a preponderance of bare ground). Herbaceous vegetation provides thinner, lighter fuels that dry out comparatively quickly, and is more abundant in drier climatological zones, allowing the fuel to remain dry for longer periods of time. Under these conditions, fire ignition is physically possible at any time of day, and the resulting diurnal fire cycle is dictated primarily by the diurnal cycle of human activity. The opposite extreme of very high fractional tree cover corresponds to tropical rainforest, and here diurnal meteorological conditions (primarily humidity) only permit ignition during a relatively brief period of the day.

As noted earlier, the mean diurnal fire cycles derived for the Eastern Sahel and Northern Australia regions show noticeable dips in daytime fire activity, leading to prominent secondary peaks in their mean diurnal fire cycles. (While minor secondary peaks do occur in several other regions [e.g., Brazilian cropland], the amplitude of these peaks is generally smaller than the corresponding error bars.) It is unclear

whether the dips reflect a true reduction in fire activity or an inadequacy in the detection bias correction. Of the two scenarios, the latter is perhaps the more likely since both dips occur when the detection bias correction reaches its maximum (cf. Fig. 5.4). On the other hand, the diurnal fire intensity curves of Pack et al. [2000] for southern Africa show similar mid-day drops, while Eva and Lambin [1998] show a very substantial drop in CAR fire activity at $\approx$ 17:00 local time, followed by a secondary peak. Use of geostationary satellite data should help resolve this issue.

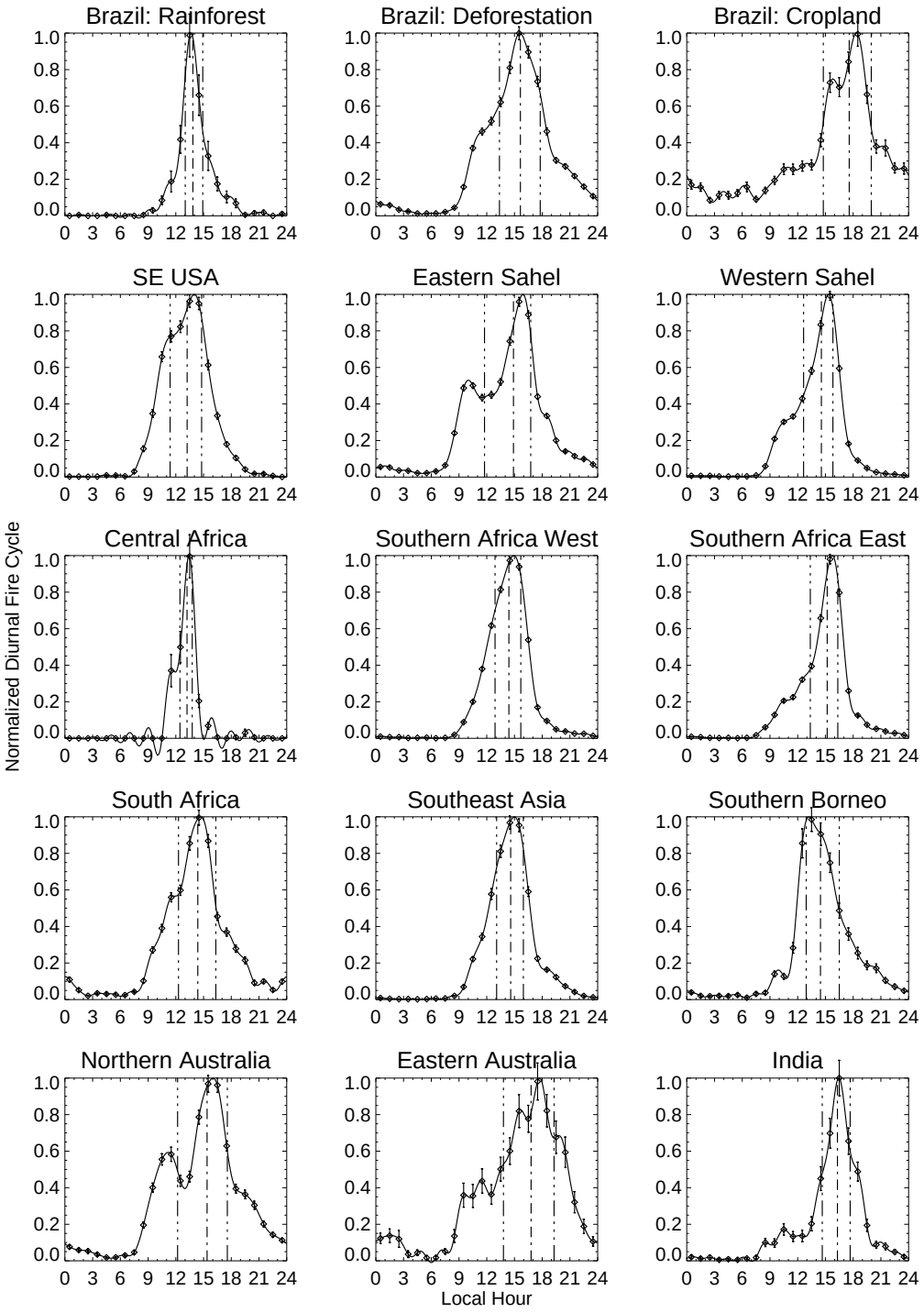

Figure 5.5: Diurnal fire cycles ($p^*(t)$) for the 15 regions considered in this study. The probability density functions have been renormalized to a maximum value of one to eliminate clutter arising from the disparate probability density scales along each abscissa. The dashed vertical lines indicate, from left to right, the locations of the lower quartile, median, and upper quartile of each PDF.

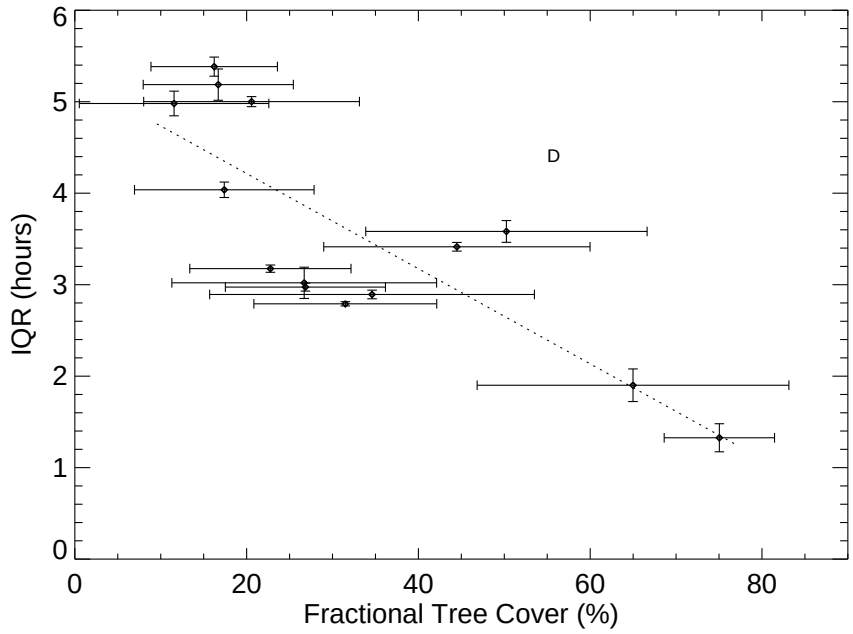

Figure 5.6: Interquartile range (IQR) of the diurnal fire probability density function for each region as a function of mean fractional tree cover. Linear least squares regression (dotted line) yields a correlation coefficient of 0.81. The point marked with a "D" corresponds to the Brazilian deforestation region, and was not included in the regression since the static tree cover map does not reflect the shift toward herbaceous vegetation observed in this region from 1998 to 2005.

Table 5.2: Summary parameters for the diurnal fire probability density functions derived for each region. Peak and median local times are expressed as decimal hours (e.g., 13.6 h = 13:36 local time).

Region	Peak (h)	Median (h)	IQR (h)
Brazil: Rainforest	13.6 $\pm$ 0.1	13.9 $\pm$ 0.1	1.9 $\pm$ 0.2
Brazil: Deforestation	15.6 $\pm$ 0.2	15.64 $\pm$ 0.04	4.41 $\pm$ 0.06
Brazil: Cropland	18.4 $\pm$ 0.2	17.6 $\pm$ 0.1	5.2 $\pm$ 0.2
Southeast USA	14.0 $\pm$ 0.2	13.22 $\pm$ 0.05	3.41 $\pm$ 0.05
Eastern Sahel	15.92 $\pm$ 0.07	14.89 $\pm$ 0.04	5.00 $\pm$ 0.06
Western Sahel	15.34 $\pm$ 0.05	14.57 $\pm$ 0.03	3.18 $\pm$ 0.04
Central Africa	13.42 $\pm$ 0.06	13.21 $\pm$ 0.08	1.3 $\pm$ 0.2
Southern Africa West	14.9 $\pm$ 0.1	14.39 $\pm$ 0.02	2.79 $\pm$ 0.02
Southern Africa East	15.74 $\pm$ 0.05	15.19 $\pm$ 0.02	2.97 $\pm$ 0.05
South Africa	14.7 $\pm$ 0.2	14.38 $\pm$ 0.05	4.04 $\pm$ 0.09
Southeast Asia	15.0 $\pm$ 0.2	14.59 $\pm$ 0.04	2.89 $\pm$ 0.05
Southern Borneo	13.2 $\pm$ 0.5	14.47 $\pm$ 0.08	3.6 $\pm$ 0.1
Northern Australia	16.0 $\pm$ 0.3	15.38 $\pm$ 0.06	5.4 $\pm$ 0.1
Eastern Australia	17.7 $\pm$ 0.6	16.8 $\pm$ 0.2	5.5 $\pm$ 0.2
India	16.5 $\pm$ 0.2	16.30 $\pm$ 0.09	3.0 $\pm$ 0.2

5.7 Implications for the AVHRR fire data record

While the archive of several of the currently-available active fire data sets now spans more than a decade, interest has arisen in using the ∼25 year AVHRR data record to extend the active-fire time series as far back as the early 1980s. Because the AVHRR record is comprised of data collected with a series of AVHRR sensors on board successive NOAA satellites, it is important to understand the effects of this lineage on the consistency of the resulting time series.

Of relevance to the present work is the drift in the orbits of the afternoon NOAA satellites, which changed the local overpass time by 3–6 hours depending on the particular platform (Fig. 5.7a). This drifting consequently changed the diurnal sampling quite significantly over the operational lifetime of each instrument. Csiszar et al. [2003] examined the effect of the change in diurnal sampling on the radiometric contrast between fires and the non-fire background in North America, and found that spurious trends can potentially arise in the number of fires detected over non-forested areas. An additional effect, not examined (but recognized) in that study, was the different sampling of the diurnal fire cycle.

To gauge the magnitude of this effect on the consistency of the AVHRR data record, I have applied three of the diurnal fire cycles shown in Fig. 5.5 to a synthetic AVHRR time series composed of a constant number of fires detected each day. (A realistic time series would include both seasonal and stochastic elements, but the results of this analysis would not change were these refinements included.) Results are shown

in the bottom three panels of Fig. 5.7. All three regions show major spurious trends in the resulting record of fire activity, with the most extreme case occurring in the Brazilian rainforest region, where the apparent number of fires varied by nearly a factor of ten over the lifetime of the NOAA-14 AVHRR. To make matters worse, the trends in different regions can move in entirely opposite directions, potentially superimposing additional time-dependent, spatial inconsistencies on the long-term AVHRR fire record.

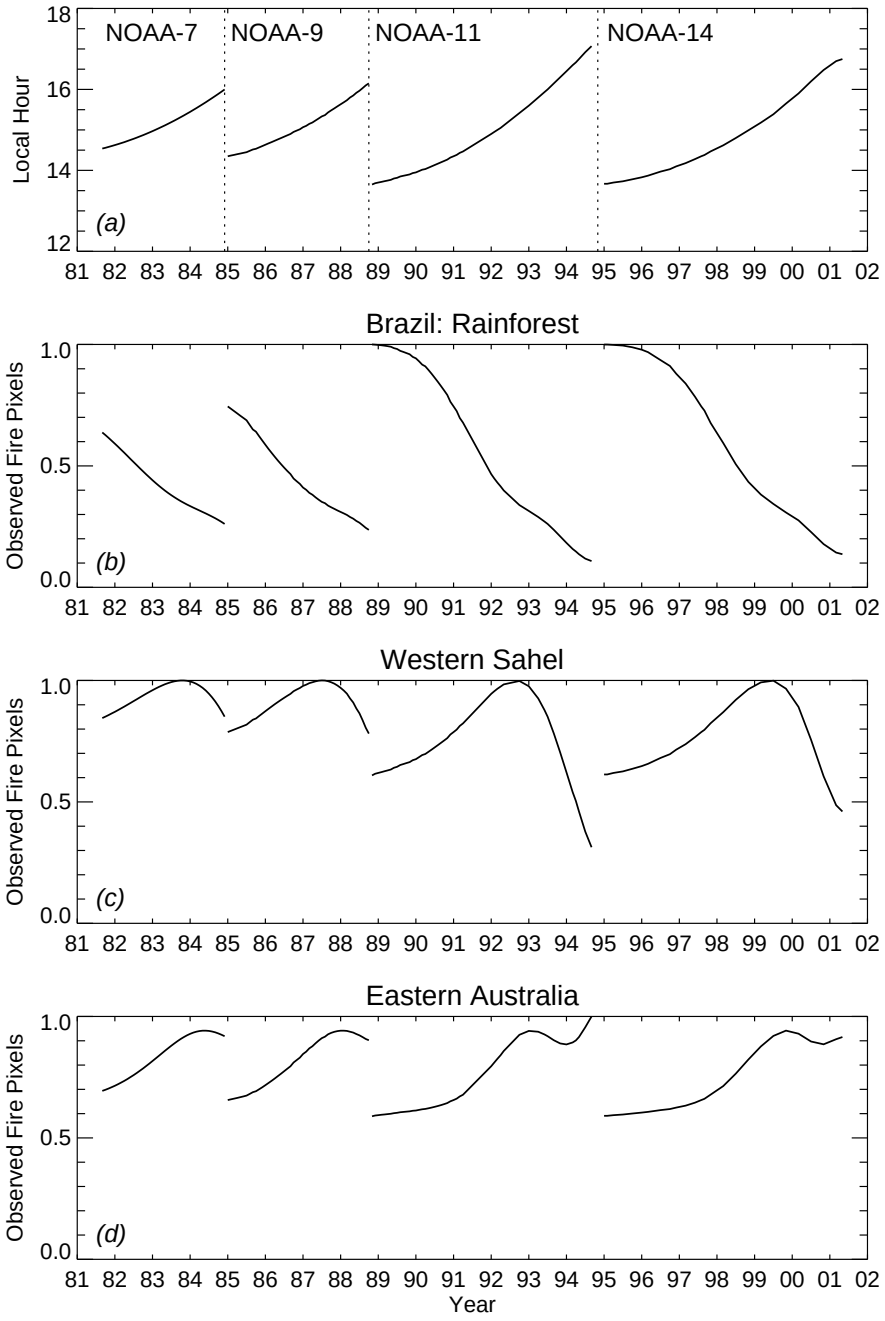

Figure 5.7: Effect of NOAA satellite drift on the time series of active fire activity as observed with consecutive AVHRR instruments. Top panel (a) shows the equator crossing time for the successive NOAA-7, NOAA-9, NOAA-11, and NOAA-14 afternoon satellites [Csiszar et al., 2003]. Lower panels show the resulting normalized time series of active fire activity, given a constant number of fires burning each day and the diurnal fire cycles obtained for the Brazilian rainforest (b), Western Sahel (c), and Eastern Australia (d) regions.

5.8 Conclusion

I have used seven years of TRMM VIRS fire observations to characterize the average diurnal fire cycle in 15 regions of the tropics and sub-tropics. Bias errors in the resulting diurnal cycles were either avoided or removed through a combination of judicious region selection and the application of corrections to compensate for cloud obscuration and time-dependent "blind spots" in the fire-detection capability of the VIRS sensor. Supplementary data from the Moderate Resolution Imaging Spectroradiometer (MODIS) on board NASA's Terra satellite were used to aid this process.

In all regions, the peak burning time varied between approximately 13:00 and 18:30, with fire activity peaking distinctly earlier for the heavily-forested regions. The time period of the central 50% of total daily fire activity (i.e., the interquartile range) varied from a minimum of 1.3 h in Central Africa to a maximum of 5.5 h in Eastern Australia. In general, shorter periods of burning (i.e., smaller values of the IQR) were associated with greater tree cover.

An analysis of the effect of the drift in the orbits of successive NOAA satellites on the AVHRR active-fire data record showed that very large, spurious trends are to be expected in the time series. It is clear that a diurnal sampling correction is essential in any analysis of long-term active fire data sets produced from AVHRR observations. Moreover, even the use of short-term, two-to-three-year AVHRR fire time series can be problematic, especially if the time period under consideration spans a change in

satellite.

Given the substantial effort involved in this work, it is reasonable to ask why one shouldn't rely exclusively on geostationary satellite sensors to investigate the diurnal fire cycle. At present, such a position would entail several disadvantages. First, the spatial resolution available from the current generation of geostationary satellites ($\sim$4 km) is lower than that available with the VIRS. This means that the GOES Imager, for example, has a significantly lower sensitivity to smaller, cooler fires. Since fires are generally smallest either when started or nearly extinguished, the widths of the peaks in fire activity derived from this sensor may be systematically underestimated. Second, although geostationary satellites provide coverage of an entire hemisphere, much of this area is not useful due to the increase in distortion as one moves away from the subsatellite point. This zonal decrease in spatial resolution means that a systematic spatial bias is present in terms of the smallest (or coolest) fires that can be detected. Finally, the current suite of operational geostationary satellites does not provide full coverage of the land surface within the tropics and sub-tropics. In this respect the VIRS sensor is therefore useful as an independent, complementary source of information about diurnal fire activity.

Chapter 6

Global Estimation of Burned Area using MODIS Active Fire Observations

6.1 Introduction

Research over the past 25 years has led to increased recognition of the important role biomass burning plays in the global carbon cycle and the production of trace gas and aerosol emissions. Consequently, Earth-system modeling efforts now often include fire-related information. In particular, there is a strong need for spatially and temporally explicit estimates of the quantity of biomass consumed through combustion [Scholes et al., 1996]. Typically such estimates are based on a simple relationship of the form [e.g., Seiler and Crutzen, 1980, Hao et al., 1990, Pereira et al., 1999]

$$M = ABc, \tag{6.1}$$

where M is the mass of vegetation combusted within a given time interval, A is the area burned during the same time interval, B is the biomass density, and c is a factor describing the completeness of combustion. Although all of the terms appearing on the

right hand side of Eq. (6.1) are highly variable, burned area is particularly difficult to estimate because of the potentially high spatial and interannual variability in this quantity at continental to global scales. It is therefore especially important that accurate, spatially explicit, multi-year estimates of burned area are available when relying on a relationship having the form of Eq. (6.1). At present, however, there is a dearth of such data. While a number of satellite-based global burned area products are currently under development, specifically GLOBSCAR [Simon et al., 2004], GBA2000 [Tansey et al., 2004], and the MODIS burned area product [Justice et al., 2002, Roy et al., 2002], none are yet available on a multi-year basis.

Unlike burned area data, long-term observations of active fires made with spaceborne sensors are readily available. Representative multi-year examples include the Along-Track Scanning Radiometer (ATSR) nighttime fire product [Arino and Rosaz, 1999], the Visible and Infrared Scanner (VIRS) monthly fire product [Giglio et al., 2003b], the Moderate Resolution Imaging Spectroradiometer (MODIS) global fire product [Justice et al., 2002], and the Geostationary Operational Environmental Satellite (GOES) Wildfire Automated Biomass Burning Algorithm (WF_ABBA) fire product [Prins et al., 1998]. At their most basic level, active fire products contain information about the location and timing of fires that are burning at the time of the satellite overpass, usually in the form of swath-based fire masks or as lists of fire pixel locations and dates. These observations are in turn often summarized at coarse spatial resolutions (e.g., $0.5^\circ \times 0.5^\circ$) over daily or monthly time periods, yielding data products containing gridded counts of active fire pixels. Although these “fire count” products

capture many aspects of the spatial distribution and seasonality of burning, it is difficult to relate them to actual area burned due to inadequate temporal sampling, variability in fuel conditions and cloud cover, differences in fire behavior, and issues related to spatial resolution [Scholes et al., 1996, Eva and Lambin, 1998, Kasischke et al., 2003].

Despite these difficulties, the lack of long-term, spatially-explicit global burned area data has meant that active fire observations must often be used as a proxy for area burned [e.g., Setzer and Pereira, 1991, Scholes et al., 1996, Stroppiana et al., 2000a, Potter et al., 2001, van der Werf et al., 2003, 2004, Langmann and Heil, 2004]. Perhaps the most common approach has been to assume that the area burned is proportional to simple counts of fire pixels, i.e.

$$A(i,t) = \alpha N_{\mathrm{f}}(i,t), \tag{6.2}$$

where A is the area burned within a particular spatial region labeled by the index i – typically a grid cell – during a fixed time period labeled by the index t, N_{f} is the number of fire pixels observed within the same region during the same time period, and α is a constant representing the effective burned area per fire pixel.

The reported accuracies of the burned area estimates obtained with Eq. (6.2) vary greatly and are dependent upon, among other things, the spatial scale at which the relationship is applied. Eva and Lambin [1998] found almost no correlation between AVHRR fire counts and burned area in the Central African Republic at a spatial resolution of 15 km over a time interval of about one month. Randriambelo et al. [1998], however, report a good qualitative agreement between one year of monthly

AVHRR fire counts and ground-based monthly burned area estimates for a study region in Madagascar. Pereira et al. [1999] report a poor linear correlation (r=0.44) between daytime AVHRR fire counts and burned area estimates in a 20° by 10° region encompassing the Central African Republic over a 25-day time period. Kasischke et al. [2003] examined the relationship between ATSR fire counts and area burned in Alaska and Canada from 1997 to 2002, and in Russia during 1998. They reported significant linear correlations between fire counts and burned area for Canada and Russia, but in the former region found that the slope (i.e., the effective area burned per fire pixel) for different years varied by up to a factor of about two. The authors caution against scaling fire counts to area burned since rates of fire detection, cloud obscuration, and fire spread are not constant across years.

Variations of Eq. (6.2) in which α assumes some spatial dependence have also been explored. Scholes et al. [1996] were able to relate the area burned in southern Africa to monthly 0.5° gridded AVHRR fire counts using ancillary Normalized Difference Vegetation Index (NDVI) data such that $\alpha(i)=f[\mathrm{NDVI}(i)]$, where f is a linearly decreasing function of the mean annual NDVI in grid cell i. In other words, increasing greenness reduces the effective burned area per fire pixel. Van der Werf et al. [2003] related burned area to VIRS active fire counts using fractional tree cover at a spatial resolution of 1° such that $\alpha(i)=f[T(i)]$, where f is a linearly decreasing function of the mean fractional tree cover T in grid cell i. Here, increasing tree cover slows the fire spread rate and reduces the effective burned area per fire pixel. The two approaches are closely related since NDVI and tree cover are positively correlated.

Active fire observations have also been used to spatially and temporally allocate climatological inventories of combusted biomass and pyrogenic trace gas emissions [Schultz, 2002, Duncan et al., 2003, Generoso et al., 2003, Heald et al., 2003, Streets et al., 2003, Jaffe et al., 2004, Damoah et al., 2006]. These methods are fundamentally related to Eq. (6.2) in that they assume the quantity of interest is proportional to counts of fire pixels. While our interest here is confined to burned area, much of the subsequent discussion is applicable to allocation-based approaches as well.

In this chapter, we present a method for calibrating active fire observations made with the Terra MODIS sensor to produce global, coarse resolution estimates of burned area on a monthly basis. Our approach draws upon two types of information: the sensitivity of α to fractional tree and herbaceous cover (extending the approach used by van der Werf et al., 2003), and the sensitivity of α to fire-pixel cluster size. These components were combined using regression trees that were applied to large geographic regions. In recognizing that production of accurate burned area maps suitable for calibration is problematic in closed canopy tropical forest, particularly in areas of active deforestation, we implement a subsequent refinement in which a correction is applied to the burned area predicted with the regression trees using tree cover data and a simple measure of fire persistence.

The uncertainties associated with any calibration approach are likely to be comparatively large given the sampling issues mentioned above, but for some applications may still be tolerable. Global models of the terrestrial carbon cycle, for example, have only recently begun to include explicit treatment of fire as a disturbance

factor [e.g., van der Werf et al., 2003]. We expressly do not claim that an active-fire based method can provide a universal substitute for burned area maps generated via direct observation of burn scars. Rather, in agreement with Schultz [2002], we suggest that statistical coarse-resolution burned area estimates derived from MODIS active fire observations can serve as a useful interim product until long-term burned area data sets become available. Moreover, it may be possible to use an active-fire calibration approach with functional sensors pre-dating MODIS, offering the possibility of generating even longer-term global burned area data sets.

6.2 Data

6.2.1 Active fire data

We used the Collection 4, version 4 Terra MODIS monthly Climate Modeling Grid (CMG) fire products at 0.5° spatial resolution ("MOD14CMH"), from January 2001 through December 2004. The gridded monthly overpass-corrected fire pixel counts were summed to a 1° working spatial resolution for this study. The CMG product also contains the mean percent tree cover (T_{f}), percent herbaceous vegetation cover (H_{f}), and percent bare ground (B_{f}) from the global MODIS Vegetation Continuous Fields (VCF) products [Hansen et al., 2003] for all fire pixels within each grid cell; we averaged these to 1° spatial resolution as well. (We use the subscript "f" as a reminder that T_{f}, H_{f}, and B_{f} are averages for fire pixels only, as opposed to averages over the

entire land surface encompassed by the grid cell.)

Using the locations of individual Collection 4 MODIS fire pixels at the nominal 1-km MODIS resolution (available separately), we linked adjacent fire pixels within each 1° grid cell into clusters on a monthly basis. For each grid cell we then computed the monthly mean fire-pixel cluster size, which we denote as C_{f}. We hypothesized that cluster-related information might improve the estimation of burned area based on the empirical observation that larger clusters of MODIS fire pixels tend to be associated with larger burn scars (Fig. 6.1).

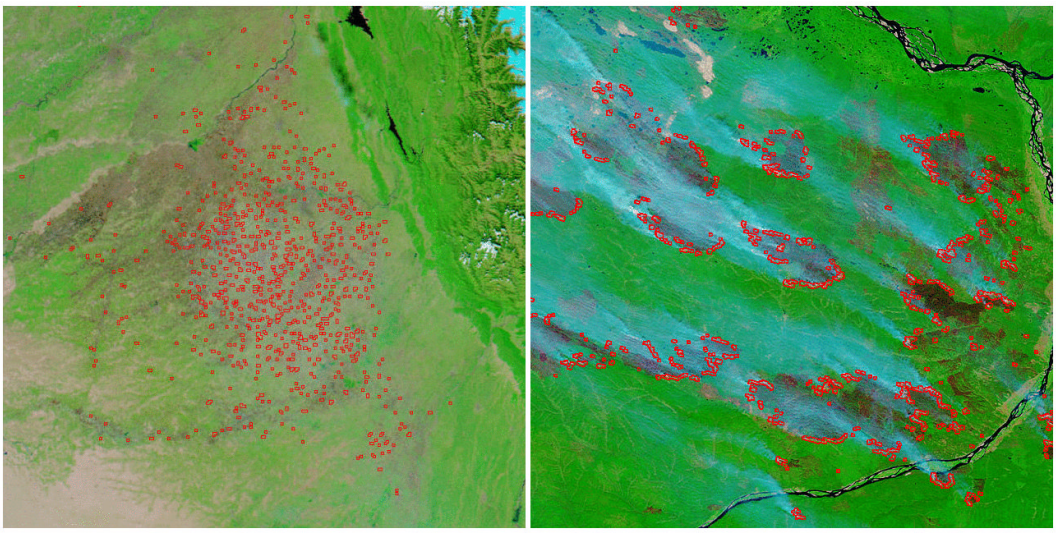

Figure 6.1: Aqua MODIS 500-m false color imagery of northern India (left) on 23 October 2004 (08:20 UTC) and Yakutsk, Russia (right) on 19 August 2002 (03:00 UTC). Outlines of 1-km active fire pixels are shown in red. With this band combination (2.1 μm, near-infrared, red) dense vegetation appears green, heavy smoke appears light blue, burn scars appear dark brown, water appears black, and non-cirrus clouds appear white. The scale (approximately 320×320 km) is identical in both images. Note how larger Yakutsk burn scars are accompanied by large clusters of adjacent fire pixels, while the small (but numerous) agricultural burns in India are characterized by much smaller clusters of fire pixels and no visible burn scars. Images were produced within the MODIS Rapid Response System and appear courtesy of Jacques Descloitres.

6.2.2 Burned area data

Burned area maps were produced using a prototype algorithm that uses the 500-m MODIS atmospherically-corrected Level 2G surface reflectance product [Vermote and Justice, 2002], the MODIS Level 3 daily active fire products [Justice et al., 2002], and the MODIS Level 3 96-day Land Cover Product [Friedl et al., 2002]. The algorithm, which is described in Appendix B, identifies the date of burn, to the nearest day, for pixels within individual MODIS Level 3 tiles [Wolfe et al., 1998] at 500-m spatial resolution. Since these burn scar masks were to serve as truth for calibration of active fire observations, we visually inspected each to ensure that no obvious omission or commission errors were present. Often this required appealing to higher resolution 250-m MODIS imagery to verify the existence of smoke plumes and help resolve the boundaries of ambiguous burn scars. Manual corrections were required in approximately five tiles, usually to add a burn scar that was undetected due to persistent cloud cover. At present, validation of our 500-m burned area maps has been limited to Russia through comparison with maps generated manually from high resolution Landsat imagery [Loboda and Csiszar, 2004]. Proper global validation would require that a similar procedure be applied to representative sites over the entire globe. This is a very substantial undertaking that has not yet been completed for any burned area product.

Selected calendar months were processed for selected MODIS tiles, yielding a total of 446 “tile-months” of burned area estimates between January 2001 and December

2004 (Fig. 6.2). Tile locations were selected to provide a good sampling of worldwide fire activity over multiple fire seasons, although erratic data availability ultimately produced an uneven temporal sampling of the different tiles. The resulting burned area maps were aggregated to 1° spatial resolution and monthly temporal resolution.

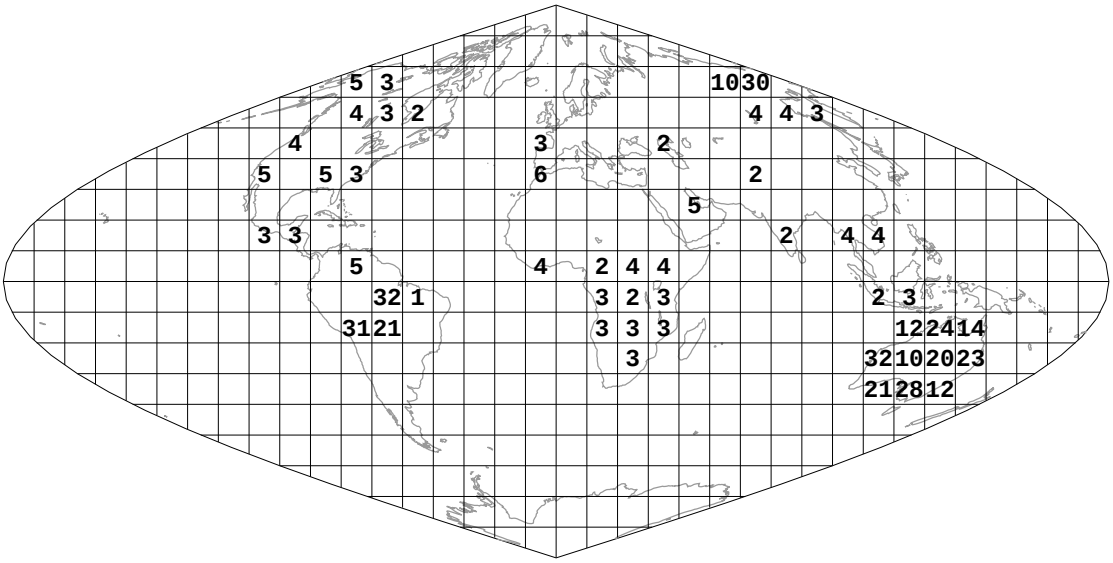

Figure 6.2: Locations of MODIS calibration tiles used in this study. Numbers in each $10^\circ \times 10^\circ$ tile indicate the number of months for which 500-m burned area masks were produced for that tile.

While we believe that commission and omission errors in our 500-m burned area maps are generally negligible compared to the statistical variability inherent in modeling the relationship between burned area and active fire pixels with Eq. (6.2), we recognize that the quality of these maps is substantially lower in the closed canopy forests of South America and Equatorial Asia. A combination of three factors make mapping of burned area problematic in this biome. First, surface burns are at least partially obscured by the tree canopy, which can leave an insufficient post-burn,

top-of-atmosphere radiometric signal with which to detect the burn. Second, substantial spectral overlap can occur between cleared (but unburned) forest patches, and patches that have been cleared and subsequently burned. Finally, persistent cloud cover ($\sim$1 month and longer) is common in rainforest, and this can lead to significant errors of omission, particularly following vegetation regrowth. This issue will be addressed further in Section 6.3.3.

6.3 Method

6.3.1 Preliminary analysis

As part of a preliminary analysis we examined the relationship between monthly corrected Terra fire pixel counts and area burned within 14 different regions (Fig. 6.3) using the model in Eq. (6.2). Results obtained from least squares fits to this model are summarized in Table 6.2. There is clearly strong regional variation in the effective area per fire pixel (α), from a minimum of 0.29 km^2/pixel in southern-hemisphere (SH) South America to a maximum of 6.6 km^2/pixel in Central Asia, which is a factor of more than 20. We note that, with the exception of the SH South America region, the correlation coefficients we obtained are substantially higher than those reported by Boschetti et al. [2004] between ATSR fire counts and the GBA2000 and GLOBSCAR burned area data sets for the year 2000. There are at least five possible reasons for our higher correlation. First, our 1° grid cells are larger than the hexagonal grid cells used by Boschetti et al. [2004] by about a factor of four at the Equator, and by a factor of two at boreal latitudes. The correlation between many spatial quantities tends to improve over larger areas [Curran and Atkinson, 2002, Fotheringham et al., 2002]. Second, with the exception of Europe, the six geographic regions defined by Boschetti et al. [2004] were much larger than the 14 geographic regions used in our study. Our results show that α can vary by as much as a factor of nearly seven within these larger regions. Third, the larger MODIS swath yields a higher temporal sampling rate, making it more likely that MODIS will "fill in" large burned areas with active fire pixels, and leading to

fewer small burned areas for which no active fire pixels were detected. (We will return to the issue of temporal sampling in Section 6.7.) Fourth, the "fill-in" effect might become more pronounced in those regions having a strong diurnal fire cycle since fewer fires are likely to be burning at the time of the nighttime ATSR overpass. Finally, smaller burns present in the 500-m MODIS burned area maps might not be identified in the 1-km GBA2000 and GLOBSCAR data sets. This last factor contributes because, for pixels of a given size, the minimum detectable size of an actively burning fire is much smaller than the minimum detectable size of a burn scar (by a factor of $\sim$1000). Mapping burn scars with larger pixels will therefore yield more cases in which small clusters of active-fire pixels are not accompanied by an observable burn scar, and will therefore reduce the correlation between the two variables (cf. Fig. 6.1, left panel).

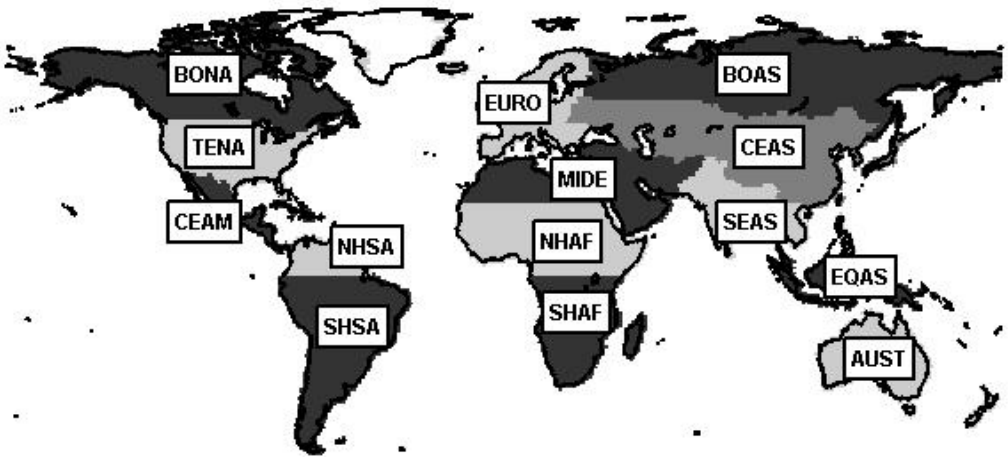

Figure 6.3: Map of the 14 regions used in this study. Abbreviations are explained in Table 6.1.

Table 6.1: Regions used within this study. Abbreviations refer to those used in Fig. 6.3.

Abbr.	Short Name	Comments
BONA	Boreal North America	Alaska and Canada.
TENA	Temperate North America	Conterminous United States.
CEAM	Central America	Mexico and Central America.
NHSA	Northern Hemisphere South America	Division with SHSA is at the Equator.
SHSA	Southern Hemisphere South America	Division with NHSA is at the Equator.
EURO	Europe	Includes the Baltic States but excluding White Russia and the Ukraine.
MIDE	Middle East	Africa north of the Tropic of Cancer, and the Middle East plus Afghanistan.
NHAF	Northern Hemisphere Africa	Africa between the Tropic of Cancer and the Equator.
SHAF	Southern Hemisphere Africa	
BOAS	Boreal Asia	Russia, excluding area south of 55° N between the Ukraine and Kazakhstan.
CEAS	Central Asia	Mongolia, China, Japan, and former USSR except Russia.
SEAS	Southeast Asia	Asia east of Afghanistan and south of China.
EQAS	Equatorial Asia	Malaysia, Indonesia, and Papua New Guinea.
AUST	Australia	Includes New Zealand.

We repeated the above analysis with fire pixel counts having an additional correction for cloud cover (data layers with and without this correction are present in the MODIS CMG fire products). The resulting correlation coefficients were almost uniformly lower, most likely because the cloud correction relies on assumptions that are frequently not met and consequently has a tendency to overcorrect. We performed the remainder of our investigation, therefore, with overpass-corrected fire pixel counts lacking the additional cloud correction.

Table 6.2: Correlation (r) between predicted and observed burned area within each region for linear regression [Eq. (6.2)] and regression tree approaches. The slope of the linear regression (α) and the total number of non-zero observations (N) are also shown. An observation consists of the corrected fire pixel counts, 500-m burned area, mean VCF fraction for all fire pixels, and mean fire-pixel cluster size within a single 1° grid cell for a specific month. Observations having zero burned area and zero fire pixels ("zero-zero" observations) were not included in the analysis and are not reflected in the tabulated values of N. All correlations are highly significant with a probability $p \ll 0.001$.

	Linear [Eq. (6.2)]			Tree
Region	α (km^2/pixel)	r	N	r
Boreal North America	1.4	0.69	1018	0.85
Temperate North America	0.84	0.94	982	0.98
Central America	0.43	0.73	301	0.85
NH South America	1.0	0.78	352	0.85
SH South America	0.29	0.35	4034	0.56
Europe	3.1	0.91	225	0.95
Middle East	0.40	0.34	215	0.78
NH Africa	5.2	0.86	910	0.90
SH Africa	2.9	0.60	1670	0.73
Boreal Asia	1.3	0.90	2104	0.94
Central Asia	6.6	0.85	282	0.92
South Asia	2.9	0.75	531	0.83
Equatorial Asia	0.49	0.71	192	0.78
Australia	3.4	0.82	5563	0.89

We next examined the effect of tree cover on α. We partitioned the observations for each region into 20% tree-cover intervals and fitted Eq. (6.2) separately to each of the resulting subsets. Results for five regions are shown in Fig. 6.4. We found that in savanna regions α decreased with increasing tree cover, although the slope of the relationship varied substantially between different savanna regions. A similar analysis revealed a comparable link between α and herbaceous cover, but with α increasing with increased herbaceous cover. This is not surprising given that, in most fire susceptible areas, woody-herbaceous gradients (rather than, say, woody-bare gradients) are more often the norm. The variation in α with respect to bare cover was generally much weaker except in Australia, where fires are common along gradients of bare and herbaceous cover. In tropical forests (e.g., South America), there was no significant relationship between α and tree cover, and in boreal forests α slightly increased with increasing tree cover.

We also examined how α varied with respect to mean fire-pixel cluster size. We partitioned the observations for each region into different ranges of mean cluster size and fitted Eq. (6.2) to each of the resulting subsets. We found that, in general, the effective burned area per fire pixel increased very rapidly as cluster size increased (Fig. 6.5).

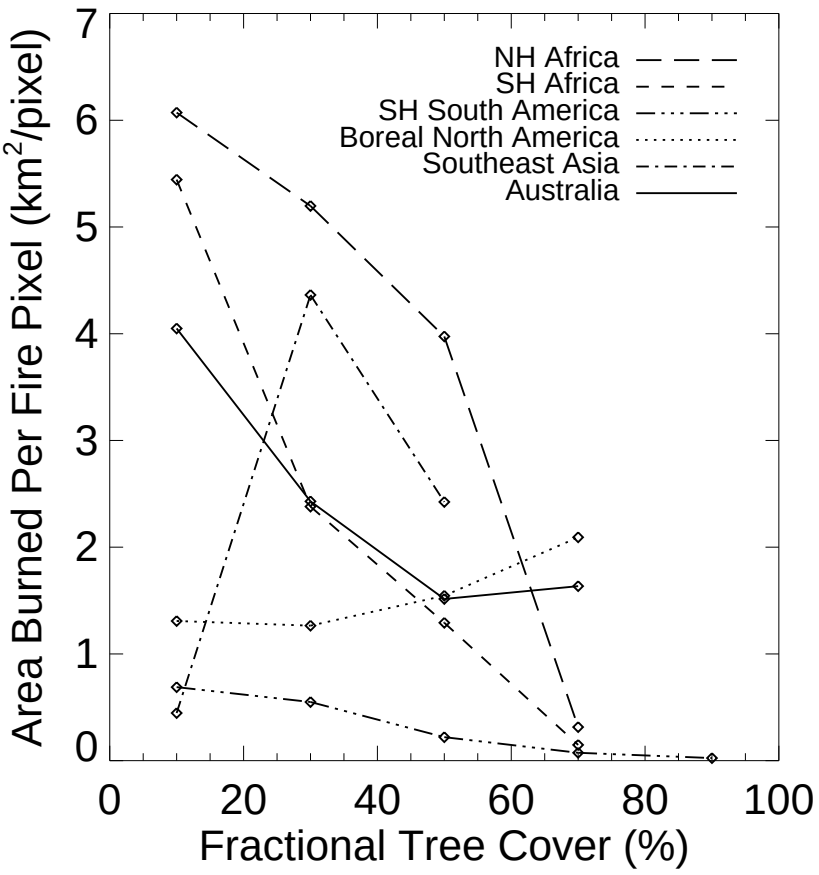

Figure 6.4: Effective burned area per Terra MODIS fire pixel (α) as a function of mean percent tree cover for six of the 14 regions considered in this study.

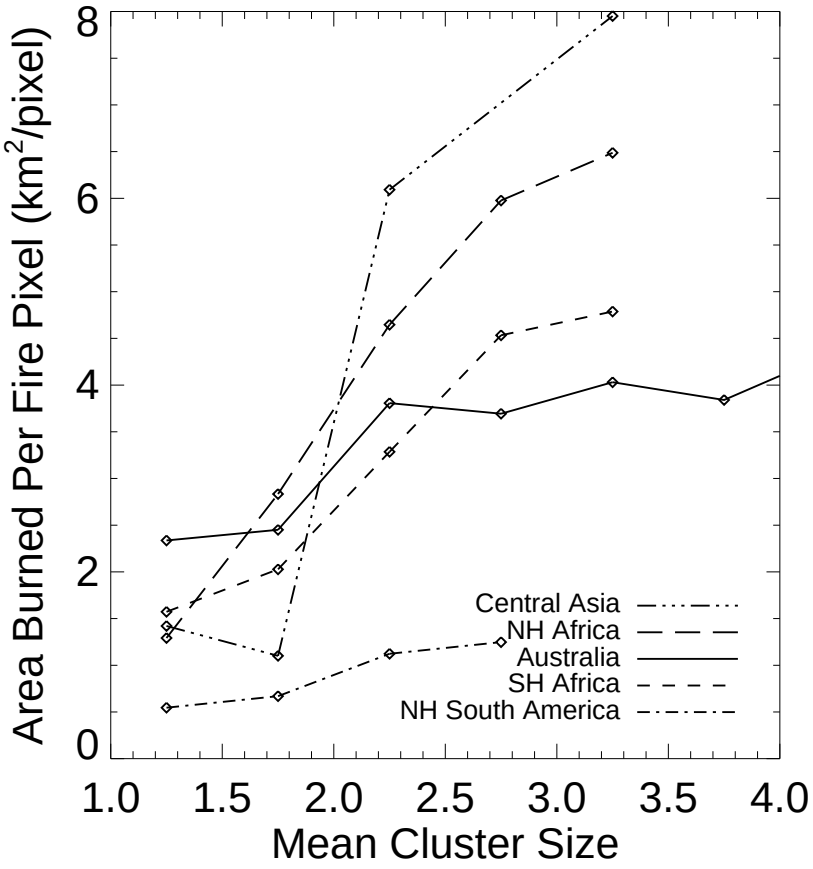

Figure 6.5: Effective burned area per Terra MODIS fire pixel (α) as a function of mean fire-pixel cluster size for five of the 14 regions considered in this study.

6.3.2 Regression tree approach

The analysis in the previous section shows that vegetation fraction (tree [$T_{\rm f}$], herbaceous [$H_{\rm f}$], bare [$B_{\rm f}$]) and fire cluster size $(C_{\rm f})$ are important predictive variables that should potentially appear in an empirical relationship linking active fire counts to area burned. We may write such a relationship very generally as

$$A(i,t) = g[T_{\rm f}(i,t), H_{\rm f}(i,t), B_{\rm f}(i,t), C_{\rm f}(i,t), N_{\rm f}(i,t)] \tag{6.3}$$

where g is an unknown function. It is not obvious, however, what particular functional form one should assume for g that will be optimal in every region. Based on a separate exploratory analysis, we believe that a globally optimal function is likely to require an unreasonably large number of free parameters. We therefore pursued the conceptually simpler approach of expressing the relationship in Eq. (6.3) as a *regression tree* for each region.

A regression tree is an alternative model for expressing a relationship between a continuous dependent variable y and one or more predictive (or explanatory) variables x_i [Breiman et al., 1984]. The tree per se consists of a set of rules of the form "if x_1<1 and x_2<2 then y=3" which supply an appropriate value for y over the range of the x_i. These rules are constructed by partitioning (or splitting) observations along the x_i into two subsets in such a way as to maximize the reduction in an error metric (or "deviance"). Following the split, the homogeneity of the resulting pair of subsets is increased. This procedure is applied recursively to each subset until certain stopping criteria are met (typically the number of remaining observations becomes too small, or

the reduction in deviance becomes insignificant). The resulting binary tree consists of splits (e.g., "if x_1<1"), and leaves (or terminal nodes) in which the dependent variable is assigned a value. Following tree construction, pruning is usually applied to eliminate overfitting that would otherwise degrade the predictive ability of the tree. During this process, terminal nodes having little predictive robustness are eliminated through the use of a cost-complexity function [Breiman et al., 1984].

For this study we used a more flexible form of regression tree which models the dependent variable using a linear regression in each terminal node [Breiman and Meisel, 1976]. Trees built in this manner are usually smaller and are also often easier to interpret. The particular linear model we used was simply that in Eq. (6.2). To help ensure the resulting fit was robust, we required a minimum of 30 observations within each terminal node. (By "observation" we are referring to the corrected fire pixel counts, 500-m burned area, mean fire-pixel VCF fractions (tree, herbaceous, bare), and mean fire-pixel cluster size within a single 1° grid cell for a single month.)

During tree construction, we permitted splitting on all five predictive variables appearing in Eq. (6.3). These variables are clearly not independent given their constraints ($T_\mathrm{f}+H_\mathrm{f}+B_\mathrm{f}$=100%, $C_\mathrm{f} \leq N_\mathrm{f}$), and that, within the tropics, larger fire clusters tend to occur in regions having higher herbaceous cover. This multi-collinearity will have no impact on the predictive ability of the regression trees that we derive, but it does mean that the final choice of splitting variable will be more or less arbitrary in the event two such variables yield comparable reductions in deviance following a trial split. When interpreting the final trees, therefore, one should not attach too much

significance to the fact that, say, tree cover was selected as the splitting variable rather than herbaceous cover.

6.3.3 Tropical closed-canopy forest correction

As mentioned in Section 6.2.2, accurate mapping of burned areas within tropical closed-canopy forest is extremely challenging. In brief, obscuration of the surface by persistent cloud cover and the tree canopy can lead to significant errors of omission. This problem is not unique to the MODIS instrument. A further complication occurs in tropical areas undergoing deforestation: where fire is used in the deforestation process (e.g., South America and Equatorial Asia), burning is usually preceded by mechanical clearing and aggregation of the resulting slash. Consequently, despite the fact that a relatively large area of forest has been cleared and burned, the spatial extent of the burn scar per se is much smaller than the area cleared. Satellite-based maps of burn scars under these conditions are therefore likely to systematically underestimate the effective area burned and fuel consumed. To help rectify this in our burned area product, we attempt to use information about fire persistence and tree cover to specify locations and time periods within the tropics for which a fixed correction factor, κ, will be applied to the burned area predicted via the regression trees. It may prove beneficial, in the future, to vary κ as a function of fire persistence in these areas, but we lack sufficient data to resolve this issue at present.

Our method of calculating fire persistence relied on the same subdivision of

individual 1° grid cells into a fine grid of ∼1-km cells with which we identified fire-pixel clusters (Section 6.2.1). For each 1-km cell, we counted the number of days on which fires were detected during the particular month being processed. By averaging the number of days for all 1-km cells affected by fire, we computed the mean fire persistence (in days), denoted P_{f}, for each 1° grid cell on a monthly basis In Fig. 6.6 we show the climatological average of the monthly means (weighted by the number of fire pixels each month) from January 2001 through December 2004. Perhaps most obvious is the high persistence in Boreal North America, Boreal Asia, and the American Pacific Northwest, a consequence of the higher fuel loads and lower fire spread rates in the forested areas of these regions. Smaller patches of higher persistence are present in the Middle East region as well, where some residual gas-flare contamination remains in our MODIS fire data. Of most interest here, however, is the high persistence evident in areas of SH South America and Equatorial Asia in which deforestation is actively occurring. In these regions of slash-and-burn conversion, fire is a critical element of the deforestation process. It is also evident that high fire persistence does not occur in deforestation hot spots, such as Central Africa, where "slash-and-rot" conversion is commonplace [Achard et al., 1998].

Based on the previous discussion, it is relatively straightforward to identify grid cells within tropical rainforest for which application of the correction factor is appropriate; simple thresholds applied to tree cover and fire persistence, and restricted to the appropriate tropical regions, will suffice. Selection of an explicit value for κ, however, is more difficult. Although we lack the necessary data to adjust for cloud and

canopy obscuration, we can at least use rough estimates to help correct for deforestation bias. Field observations suggest that forest clearings are typically one to ten times larger than the slash piles destined for burning, depending on whether the slashing was performed manually or mechanically (Douglas Morton and Wilfrid Schroeder, personal communication). We chose the geometric mean of these limits, yielding $\kappa \approx 3.2$. This is probably a more reasonable choice than the larger arithmetic mean as manual clearing is more prevalent in the tropics as a whole. In implementing the correction, we identified those monthly grid cells within the tropics for which $T_{\mathrm{f}}(i,t) \geq 50\%$ and $P_{\mathrm{f}}(i,t) \geq 1.2$ days. For tropical grid cells satisfying these conditions, we multiplied the burned area predicted with the appropriate regression tree by κ.

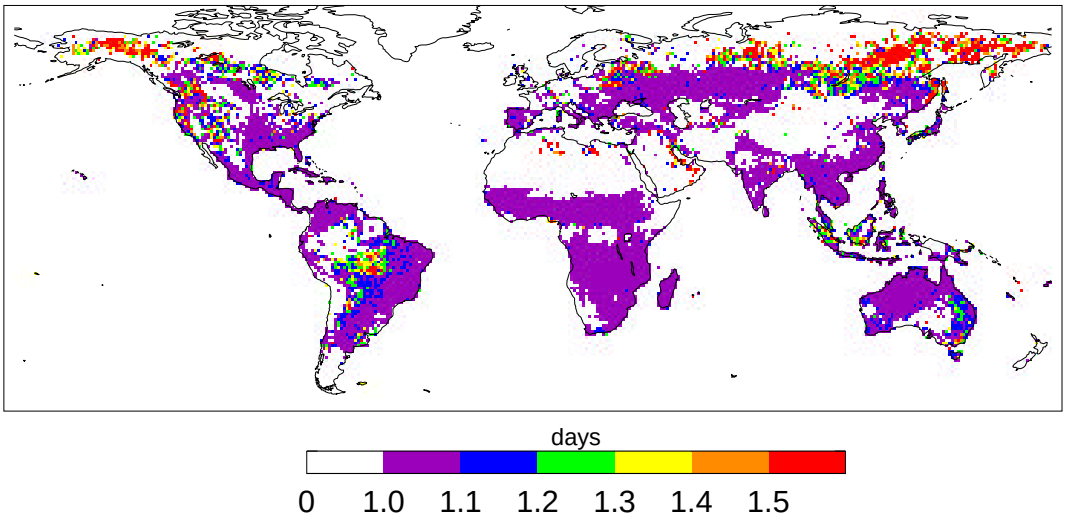

Figure 6.6: 2001–2004 mean monthly fire persistence computed from Terra MODIS active fire observations.

6.4 Results

6.4.1 Regional regression trees

Regression trees were grown and pruned for each region; representative examples of the final result obtained for three of the fourteen regions are shown in Figs. 6.7 through 6.9. The number of terminal nodes in the final trees ranged from two (Europe and Equatorial Asia) to nine (Australia and SH South America). This wide range in size primarily reflects differences in the quantity of calibration data available for each region, and secondarily as an indication of the regional complexity in the burned-area/fire-count relationship.

Taking into consideration our previous discussion of the interpretation of regression trees grown from correlated variables (Section 6.3.2), we note that, in agreement with our preliminary analysis, both vegetation cover and fire-pixel cluster information play an important predictive role in the estimation of burned area. Considering the splits in all 14 regression trees together, 41 (68%) involved one of the three VCF variables, while 17 (28%) occurred on the mean fire-pixel cluster size. A detailed analysis of the final trees revealed that the reduction in deviance achieved by splitting on C_{f} was often much larger than that achieved by splitting on tree and herbaceous cover, indicating that the predictive utility of mean cluster size is not simply an artifact of its correlation with the VCF variables in the tropics. Only two splits (3%) occurred on N_{f}, primarily to deal with mild nonlinearities in the burned-area/fire-count relationship for SH Africa and Australia.

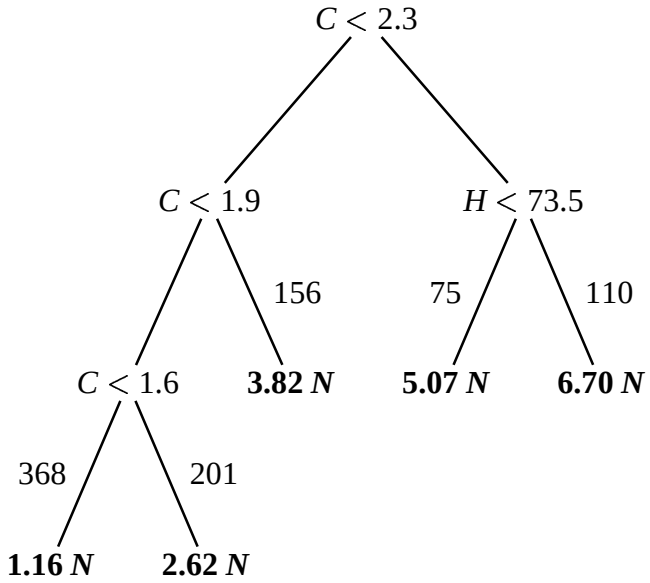

Figure 6.7: Regression tree constructed for Northern Hemisphere Africa with Terra MODIS active fire data. Terminal nodes (leaves) are shown in boldface. The left fork is taken when the condition at a split is met. The numbers adjacent to each branch leading to a terminal node indicate the total number of observations assigned to the node during construction. To reduce clutter in the figure, subscripts have been dropped from the variables $T_{\rm f}$ (percent tree cover), $H_{\rm f}$ (percent herbaceous cover), $B_{\rm f}$ (percent bare ground), $C_{\rm f}$ (mean fire-pixel cluster size), and $N_{\rm f}$ (corrected fire pixel counts). Coefficients of $N_{\rm f}$ in terminal nodes have units of km^2/pixel.

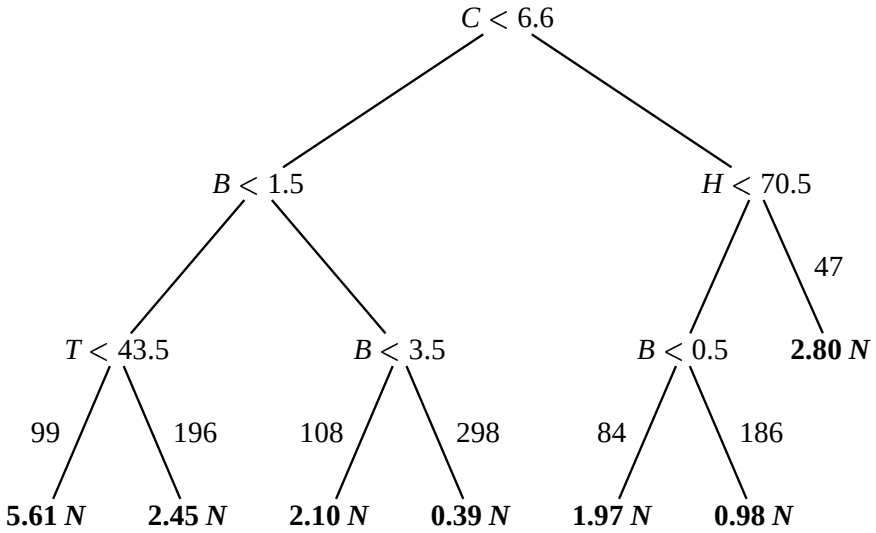

Figure 6.8: Same as in Fig. 6.7 but for Boreal North America.

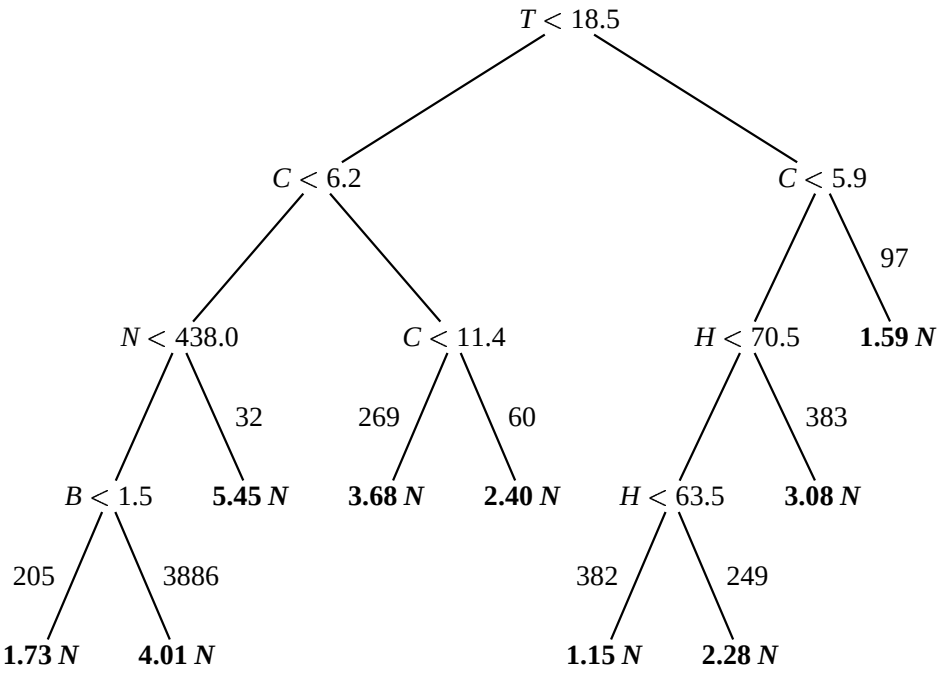

Figure 6.9: Same as in Fig. 6.7 but for Australia.

Figure 6.10 shows plots of predicted versus observed burned area for each region; the corresponding correlation coefficients are listed in Table 6.2. Regions showing the greatest agreement between predicted and observed burned area were Boreal Asia (r=0.94 with N=2104 observations), Central Asia (r=0.92, N=282), Europe (r=0.95, N=225), and Temperate North America (r=0.98, N=982); for these cases the predictions of area burned are comparatively accurate and precise. The region having poorest agreement was SH South America (r=0.56, N=4034), where predicted values of burned area suffer from large random and systematic errors. This is, at least in part, probably a consequence of the lower quality in 500-m burned area maps available for this region (Section 6.2.2). The remaining nine regions lie between these two extremes, yielding comparatively accurate, but imprecise, estimates of monthly burned area.

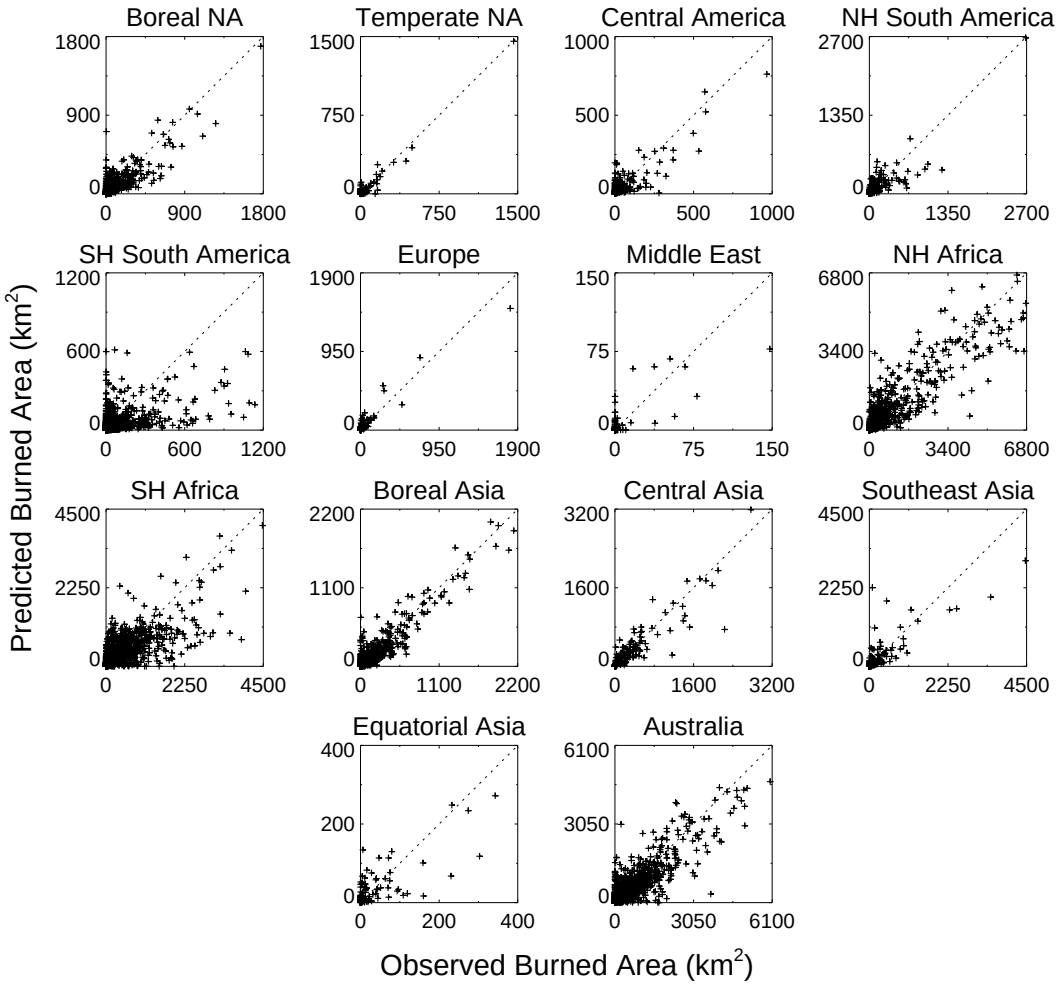

Figure 6.10: Scatter plots of burned area predicted by regional regression trees vs. "true" burned area derived from 500-m burned area maps. Axes show area in km^2.

6.4.2 Uncertainties

Since we ultimately intend to use the regression trees to produce global monthly burned area estimates for input into coarse resolution models, it is important that uncertainty estimates be provided. A natural approach for quantifying these uncertainties would be through prediction confidence intervals computed for the fit of Eq. (6.2) within each terminal node of the regression tree. However, this approach is problematic in practice since the variance in burned area is not constant but instead increases as one considers larger burned areas. This behavior is characteristic of many physical variables and is referred to as *heteroskedasticity* in the statistical literature [e.g., Mandel, 1984]. Heteroskedasticity violates the constant-variance assumption of ordinary least squares fitting and, if ignored, may lead to inaccurate statistical error estimates for the fit.

Methods for dealing with heteroskedastic variables (weighted least squares, nonlinear data transformation) increase the influence of low-variance observations on the fit, while simultaneously decreasing the influence of high-variance observations. For our purposes this is undesirable. While it is true that the observations of very small burned areas have very low variability in an absolute sense (but very *high* variability in a relative sense), it is also true that these points are usually of less interest to most users. (An important exception is the burning of aggregated forest slash. As discussed in Section 6.3.3, such fires can consume prodigious quantities of biomass yet leave a very small burn scar.) In terms of emissions and land cover conversion, it is the observations of larger burns (which have high absolute variability but low relative

variability) that are generally most important. Compensating for heteroskedasticity will therefore have the undesirable effect of assigning the greatest importance to the observations of least interest to us; this will in turn introduce biases (usually downward) in the predictions of large burned areas.

Given the above issues, we did not correct for heteroskedasticity when fitting Eq. (6.2) but adopted an alternative approach for estimating the uncertainties in our burned area estimates. For the fit of Eq. (6.2) within each terminal node of the regression tree, we regressed the square of the residuals (i.e. the variance) against fire pixel counts. The square root of the variance predicted by this supplementary fit then provided a one-standard-deviation ("one-sigma") uncertainty estimate for all future predictions emanating from the terminal node.

6.5 Multi-Year burned area estimates

We applied the regional regression trees to the entire archive of high-quality Terra MODIS data to produce a monthly global burned area data set spanning November 2000 through mid-2005. Using these data, we calculated the 2001–2004 mean monthly area burned and the associated uncertainties (Fig. 6.11). In propagating the monthly uncertainties we assumed they were random and independent, and hence added these in quadrature. (Given the large systematic errors noted earlier for SH South America, these estimates should be considered lower bounds in this region. The uncertainties in mean annual burned area suggested by Fig. 6.11 therefore probably underestimate the

true error.) In general, the absolute uncertainties for regions characterized by large burned areas ($\gtrsim$1000 km^2/year) correspond to relative errors of 10% to 40%. In regions characterized by relatively small burned areas ($\leq$100 km^2/year), the absolute uncertainties typically correspond to much higher relative errors of 50% to 100%.

In Table 6.3 we show the annual area burned within each region for the years 2001–2004. The most extensive burning consistently occurred in northern hemisphere (NH) Africa, with well over 10^6 km^2 burned in this region each year. Over this four-year period substantial interannual variability – here arbitrarily defined as having at least one year of burned area varying by more than 50% of the four-year mean – occurred in Boreal North America, Boreal Asia, Equatorial Asia, and Australia. The interannual variability of burned area in NH Africa exceeded the annual area burned in all other regions, except SH Africa and Australia, over all four years. Taken together, the total area burned in northern- and southern-hemisphere Africa and Australia from 2001–2004 comprised 80% of the total area burned globally.

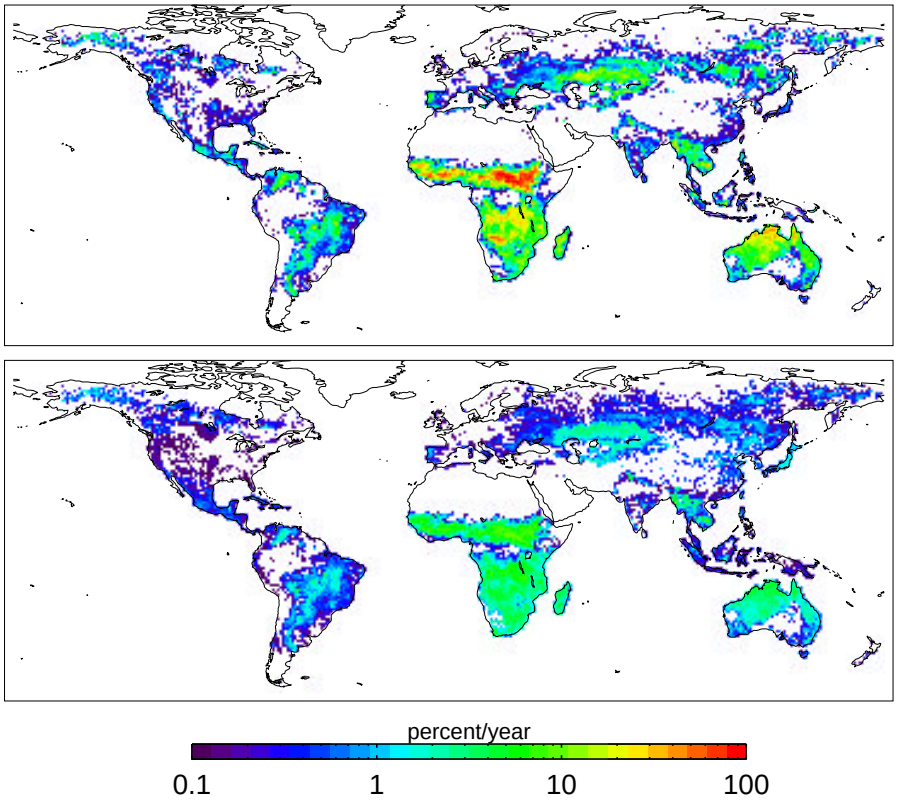

Figure 6.11: 2001–2004 mean annual burned area derived from Terra MODIS active fire observations (top), and accompanying one-sigma uncertainties (bottom), expressed as the fraction of each grid cell that burns each year. One-sigma uncertainties were obtained by adding our spatially-explicit, monthly uncertainty estimates (assumed to be independent and random) in quadrature (Section 6.5). The estimation of monthly uncertainties is described in Section 6.4.2.

Table 6.3: 2001–2004 estimated annual area burned for the regions used in the study, with the mean of the relative errors (MRE) for the individual years shown in the rightmost column.

	Area Burned ($\times 10^4$ km^2=Mha)				
Region	2001	2002	2003	2004	MRE (%)
Boreal North America	0.4	2.6	2.3	4.0	8
Temperate North America	1.4	1.7	1.5	1.2	4
Central America	1.8	2.2	2.9	1.8	8
NH South America	4.4	3.6	4.8	3.8	6
SH South America	12.4	12.7	10.8	13.4	5
Europe	2.9	1.6	2.6	1.9	4
Middle East	0.6	0.5	0.4	0.4	8
NH Africa	153.2	135.2	125.5	129.8	2
SH Africa	84.0	82.4	79.6	75.3	3
Boreal Asia	6.3	9.3	14.5	4.9	3
Central Asia	16.5	26.7	17.1	18.9	4
Southeast Asia	10.8	10.2	8.4	16.1	7
Equatorial Asia	0.8	3.4	1.4	2.9	9
Australia	78.7	58.9	24.8	44.9	2

6.6 Evaluation

Rigorous validation of our global burned area data set requires independent, ground-truth quality maps of burn scars from representative locations over the entire globe. At present there is a paucity of such data, especially data that encompasses the monthly, 1° scale of our estimates. For example, global validation using direct estimates of burned area from Landsat imagery is limited by high data volumes and temporal discontinuities. A single Landsat scene provides coverage over an area approximately 180 km by 180 km in size, spanning in entirety at most a single 1° grid cell. When combined with the 16-day Landsat repeat cycle, it is difficult to unambiguously assign burned area to a specific calendar month. A practical (but more limited) alternative, which we describe here, is to compare our estimates of burned area to existing independent inventories. Results are summarized by region.

6.6.1 Canada

We compared our burned area estimates to independent estimates compiled by the Canadian Interagency Forest Fire Centre (CIFFC). These data are provided on a yearly basis from 2001–2004 for nine Canadian provinces (British Columbia, Alberta, Manitoba, Newfoundland and Labrador, Northwest Territories, Ontario, Quebec, Saskatchewan, and the Yukon Territories). A plot of predicted versus CIFFC burned area (Fig. 6.12) shows a very strong linear relationship (slope = 0.70, r=0.89, $p \ll 0.001$), with some degree of underestimation for very large burned areas. This bias

might in part be explained by the fact that ground-based and aerial surveys often record only the outermost perimeter of burn scars.

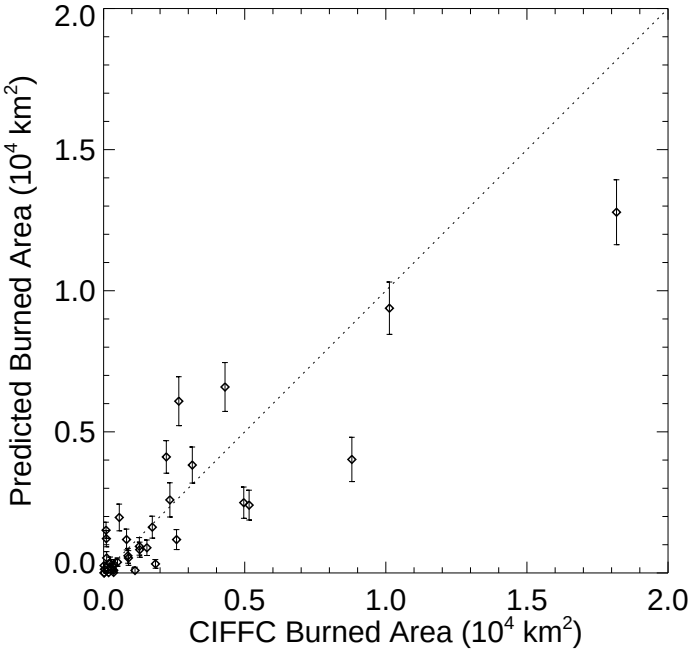

Figure 6.12: Burned area predicted by regression tree each year for individual Canadian provinces during 2001–2004, versus annual provincial totals compiled by the Canadian Interagency Forest Fire Centre (http://www.ciffc.ca/). Error bars represent one-sigma uncertainties in predicted values.

6.6.2 United States

We compared annual nationwide burned area statistics (including Alaska) compiled by the National Interagency Fire Center (NIFC) for the years 2001–2004 (Fig. 6.13). The two data sets are strongly linearly related (slope = 0.83, r=0.91, p=0.093), although there is again a modest bias towards underestimation in large fire years. As with

Canada, this bias might be partly explained by the manner in which large burns are surveyed. Considering the NIFC statistics as truth, the mean absolute percent error (MAPE) of our estimates is 13%.

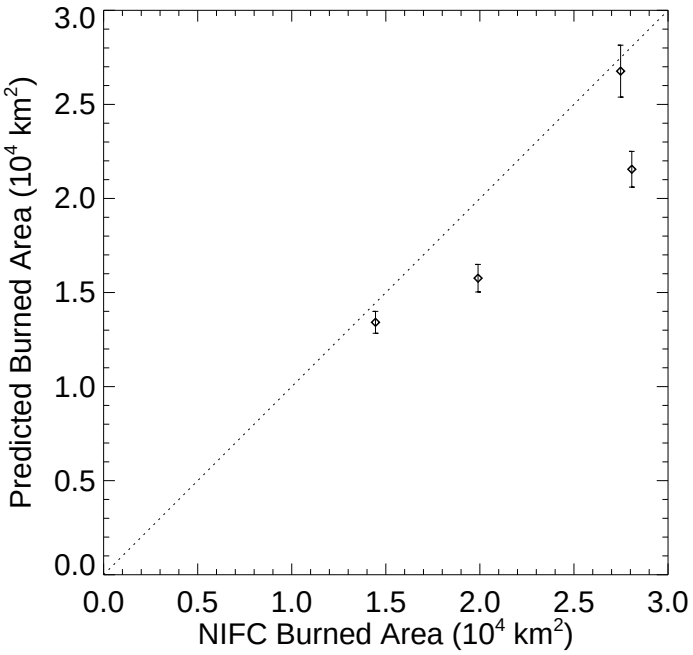

Figure 6.13: Total predicted burned area within the United States for the years 2001–2004 versus annual totals compiled by the National Interagency Fire Center (http://www.nifc.gov/stats/index.html). Error bars represent one-sigma uncertainties in predicted values.

6.6.3 Russia

We compared the total area burned in Russia for 2001 and 2002 to estimates produced by Sukhinin et al. [2004] from satellite data (Table 6.4). For 2001, a year of somewhat lower fire activity, our estimates were about 26% larger. For 2002 both totals agree to

within a few tenths of a percent.

Table 6.4: Comparison of predicted annual area burned in Russia with estimates of Sukhinin et al. [2004].

	Area Burned ($\times 10^4$ km^2=Mha)	
Year	This study	Sukhinin et al. [2004]
2001	9.6	7.56
2002	12.1	12.1
2003	16.0	–
2004	6.9	–

6.6.4 World

Our estimates of the total global annual area burned calculated for the years 2001–2004 range from a low of 2.97 million km^2 in 2003 to a high of 3.74 million km^2 in 2001. Although this does not qualify as an evaluation, we compared these results to the GBA2000 and GLOBSCAR products available for the year 2000 (Table 6.5). Despite the fact that we are comparing different years, our annual totals are only 0.3% to 27% higher than the total obtained with GBA2000. They are, however, substantially above the annual total obtained from GLOBSCAR, by a minimum of 51% and as much as 92%. Confining the comparison to November and December 2000, the only time period during which all three data sets overlap, our total burned area (0.91 million km^2) is about 32% higher than that of GBA2000, and 144% higher than that of GLOBSCAR. Thus, even if the 2002–2003 period corresponding to the weak El-Niño Southern Oscillation is not considered, the global burnt area estimate derived here is significantly higher than the GLOBSCAR estimate.

Table 6.5: Comparison of global annual area burned obtained from the GBA2000 [Tansey et al., 2004] and GLOBSCAR [Simon et al., 2004] data sets, and estimated using the calibration approach described in this chapter.

Source	Year	Area Burned ($\times 10^6$ km^2)
GBA2000	2000	2.93
GLOBSCAR	2000	1.94
This study	2001	3.74
	2002	3.51
	2003	2.97
	2004	3.19
	2001–2004 mean	3.35
GBA2000	Nov.–Dec. 2000	0.69
GLOBSCAR	Nov.–Dec. 2000	0.37
This study	Nov.–Dec. 2000	0.91

6.7 Application to other sensors

Clearly any active-fire calibration technique must be tuned to a specific sensor to compensate for differences in the characteristics of the sensor (e.g., spatial resolution), as well as the temporal sampling afforded by the platform on which the sensor resides. The latter issue is especially relevant because an increase in the rate at which "snapshots" of an active fire are made will generally increase the correspondence between a map of cumulative fire pixels and the spatial extent of the burn scar. It is instructive, therefore, to consider the effective temporal sampling rate of a particular instrument in gauging its suitability for providing burned area estimates via active-fire calibration. For a sensor on board a satellite having a polar or precessing orbit, a convenient measure of this sampling frequency is the daily equatorial coverage,

denoted c_{eq}, which is simply the fraction of the Equator imaged by the sensor each day, irrespective of exactly where along the Equator the imaging occurs. For a swath width of w, this quantity is given by

$$c_{\mathrm{eq}} = \frac{w}{\pi R_E \sin\gamma} \left(\frac{24\,\mathrm{h}}{T} \right), \tag{6.4}$$

where R_E is the radius of the Earth, γ is the orbit inclination, and T is the orbital period (in hours). Values of the daily equatorial coverage for the MODIS, VIRS, and ATSR instruments (normalized to that of MODIS) are listed in Table 6.6. For the ATSR we explicitly considered the effect of restricting observations to nighttime overpasses, which halves the coverage predicted by Eq. (6.4), since the ATSR nighttime fire product is restricted in this manner.

Comparing the VIRS and MODIS instruments, the former provides about 34% less equatorial coverage; although the orbit inclination of the TRMM satellite on which VIRS resides increases the coverage by a factor of about two, the VIRS swath is narrower by a factor of about three. This suggests that a calibration-based technique based on VIRS active fire data is likely to yield lower quality estimates of burned area than for MODIS. More robust estimates are expected at higher subtropical latitudes where the VIRS sampling frequency increases by about a factor of three [Giglio et al., 2003c]. However, the coarser VIRS spatial resolution (2.5 km) will probably degrade the quality of any calibration relationship involving cluster size, regardless of latitude, since VIRS fire-pixel clusters, being composed of larger areal units, provide a narrower range of unique values over which to discriminate different burned areas.

A comparison between MODIS and ATSR is more straightforward since these instruments have virtually identical spatial resolution. Given the narrower swath, combined with the need to restrict fire observations to nighttime overpasses, the ATSR provides nearly an order of magnitude fewer opportunities to record active fire activity at the Equator. In the context of our calibration approach, this is equivalent to discarding nearly 90% of the MODIS active fire pixels recorded in each grid cell each month and repeating the calibration procedure. In addition, clusters of cumulative ATSR fire pixels are also likely to be smaller and more fragmented since the time interval between successive satellite overpasses is about ten times longer, thus reducing the utility of cluster-related information as a splitting variable. The combination of these factors is likely to yield larger uncertainties in estimates of burned area produced by calibrating ATSR active fire observations. Nevertheless, the ATSR has been shown to provide very useful estimates of the seasonal and interannual variability in burned area [e.g., Schultz, 2002].

Table 6.6: Swath width (w), orbit inclination angle (γ), and temporal sampling frequency (relative to that of the MODIS instruments) at the Equator for three sensors on-board operational satellites.

Sensor	w (km)	γ (°)	Relative Sampling Frequency
MODIS[1]	2330	98	1
VIRS[2]	830	35	0.66
ATSR[3]	512	99	0.22 (day)
			0.11 (night)

[1] Values applicable to Terra and Aqua MODIS instruments.
[2] Post August 2001 orbit boost.
[3] Entries are also applicable to the Advanced ATSR (AATSR).

6.8 Conclusion

We have presented a method for estimating monthly burned area globally at 1° spatial resolution using Terra MODIS active fire observations and ancillary vegetation cover information. Using regional regression trees, these data were calibrated to burned area estimates derived from 500-m MODIS imagery based on the conventional assumption that burned area is proportional to counts of fire pixels under specific conditions. Traditionally, the constant of proportionality (α) has either been held fixed, or adjusted based on a single vegetation-related parameter. Neither practice is satisfactory at a global scale. We propose a more flexible approach in which α is permitted to vary as a function of both tree and herbaceous vegetation cover (or alternatively bare ground fraction), and the mean size of monthly cumulative fire-pixel clusters within each 1° grid cell. Though we found this to be usually unnecessary, we also allowed α to vary with fire pixel counts to accommodate slight deviations from the assumption of linearity. The exact form of the functional dependence of α on these predictive variables was not specified a priori, but was constructed through recursive partitioning and expressed in terms of the splits and leaves of a regression tree. In addition to their considerable flexibility, regression trees offer the advantage of readily accommodating additional explanatory variables on a trial basis.

Recognizing limits in our ability to measure burned area in closed canopy tropical forests, we used information about monthly fire persistence and tree cover to identify locations and time periods within the tropics requiring the application of a fixed

correction factor to the burned area predictions obtained from the regression trees.

Regions showing good agreement between predicted and observed burned area included Boreal Asia, Central Asia, Europe, and Temperate North America, where the estimates produced by the regression trees were relatively accurate and precise. Poorest agreement was found for SH South America, where predicted values of burned area are both inaccurate and imprecise. The poor result obtained in this region is most likely a consequence of multiple factors that include extremely persistent cloud cover and a degradation in the quality of the 500-m burned area maps used for calibration. Agreement in the nine remaining regions fall between these two extremes, yielding comparatively accurate, but less precise, estimates of monthly burned area.

We used the regional regression trees to produce multi-year, global burned area estimates on a monthly basis from the current archive of Terra MODIS active fire data. Annual totals derived from these data showed good agreement with independent annual estimates available for nine Canadian provinces, the continental United States, and Russia. Using these data, we estimated the global annual burned area for the years 2001–2004 to vary between 2.97×10^{6} and 3.74×10^{6} km^{2}, with the maximum occurring in 2001. The most extensive burning consistently occurred in NH Africa, with well over 10^{6} km^{2} burned in this region each year. Over this four-year period significant interannual variability occurred in Boreal North America, Boreal Asia, Equatorial Asia, and Australia. Taken together, the total area burned in northern- and southern-hemisphere Africa and Australia from 2001–2004 comprised 80% of the total area burned globally.

We reiterate that we are not promoting our regression-tree approach (or, indeed, any active-fire calibration approach) as a substitute for burned area maps generated from direct observations of burn scars. Rather, for some applications, statistical coarse-resolution burned area estimates derived from MODIS active fire observations can serve as a useful interim product until long-term burned area data sets become available.

Chapter 7

Conclusion

7.1 Summary of Research

The five individual studies presented in this dissertation, which center around the utilization of MODIS data, address a range of issues related to the remote sensing of fires using satellite-based sensors. In this final chapter, I will briefly review each study, with an emphasis on the importance of the results obtained from this work for the global modeling community.

In Chapter 2 an operational active-fire detection algorithm was presented for the MODIS instrument on-board NASA's Terra and Aqua satellites. MODIS has enabled, for the first time, global daytime and nighttime fire monitoring in near real time, and the compilation of a multi-year data record of fire activity. The algorithm, which incorporates many refinements to earlier approaches, offers greater sensitivity to smaller, cooler fires, as well as a lower false alarm rate under many conditions. Both features are important in that they provide a more accurate picture of global fire activity. As mentioned in Chapter 4, for example, the fire detection algorithm used to

produce the AVHRR Global Fire Product (GFP) is particularly susceptible to false alarms. Among other problems, the high false alarm rate makes it appear as though fire activity is both frequent and uniformly likely across the entire continental United States; this is extremely misleading and not at all representative of reality.

Validation of the MODIS active fire products requires coincident fire observations of a higher spatial resolution. To this end, Chapter 3 presented an automated active-fire detection algorithm for the high resolution ASTER instrument. Since ASTER lacks channels in the mid-infrared portion of the electromagnetic spectrum, the algorithm differs somewhat from the methods used with the coarser-resolution sensors traditionally used for active fire monitoring. ASTER co-resides with the MODIS sensor on-board the Terra satellite, and as such has become an important tool in the ongoing validation of the Terra MODIS active fire products. The resulting 30-m ASTER fire masks provide a significant step forward in that they enable large, meaningful statistical samples to be employed in the evaluation of the MODIS (and potentially VIRS and SEVIRI) active fire products.

In the work described in Chapter 4, MODIS fire data were distilled into a format suited for global modeling studies, and these data were used to analyze the global distribution of biomass burning using five different temporal metrics (fire pixel density, peak fire month, fire season length, annual periodicity, and fire radiative power [FRP]). Additionally, three years of Terra and Aqua MODIS observations were combined to demonstrate that a strong diurnal fire cycle is prevalent at tropical and subtropical latitudes. The consistency of the fire time series recorded by the two MODIS

instruments was also considered; in most areas the month of peak burning and the length of the fire season observed by each was found to be in good agreement. As shown in this work, the MODIS CMG active fire products provide useful information about the spatial and temporal dynamics of global fire activity, the distribution of fire activity within different land cover types, and fire intensity. In particular, given the current paucity of spatially-explicit, global burned area data, active fire products continue to be the only source of information about the interannual variability of fire activity at large spatial scales.

To understand the MODIS product more fully Chapter 5 presented a more detailed look at the diurnal fire cycle in 15 different regions of the tropics and subtropics. Bias errors in the resulting diurnal cycles were either avoided or removed through a combination of judicious region selection and the application of corrections to compensate for cloud obscuration and time-dependent “blind spots” in the fire-detection capability of the VIRS sensor. A strong diurnal cycle was found in all regions, with the time of peak burning varying between approximately 13:00 and 18:30 local time. An important finding of this work was that a correction for orbital drift is absolutely critical when producing multi-year, active fire data records from the AVHRR instruments residing on the NOAA satellites.

Finally, recognizing the limitations of active fires observations for representing burned area, and the importance of burned area information for global change research, Chapter 6 presented a method for estimating monthly burned area globally at 1° spatial resolution using Terra MODIS data and ancillary vegetation cover information. Using

regression trees constructed for 14 different global regions, MODIS active fire observations were calibrated to burned area estimates derived from 500-m MODIS imagery based on the assumption that burned area is proportional to counts of fire pixels. Unlike earlier methods, the constant of proportionality was allowed to vary as a function of tree and herbaceous vegetation cover, and the mean size of monthly cumulative fire-pixel clusters. In areas undergoing active deforestation, a subsequent correction was devised based on tree cover information and a simple measure of fire persistence. The regional regression trees were used to produce global burned area estimates on a monthly basis from the current archive of Terra MODIS active fire data from November 2000–December 2005. At the time of this writing, this data set is the only source of global, spatially-explicit burned area data available on a multi-year basis. While not a universal substitute for burned area maps generated via direct observation of burn scars, coarse-resolution burned area estimates derived from MODIS active fire observations can serve as a useful interim product for global emissions and carbon cycle models until long-term, directly-mapped burned area data sets become available.

7.2 Implications of the Research

The MODIS fire data produced as part of this research (Chapters 2 and 4) have advanced our knowledge of global biomass burning. At present these data are the only multi-year, global fire data set to include daytime fire observations. The global MODIS

fire product also provides, for the first time, a global picture of the FRP, a quantity having, among other benefits, significant potential to improve estimates of pyrogenic emissions. To date, MODIS fire data have been used to address scientific questions [Clerici et al., 2004, Damoah et al., 2004, Edwards et al., 2004, Jaffe et al., 2004, Edwards et al., 2006, Damoah et al., 2006, Giglio et al., 2006a,b, Mollicone et al., 2006] as well as to support operational fire management via the MODIS Rapid Response System and a suite of Direct Broadcast receiving stations. The research presented in this thesis has also shown that MODIS active fire data can be used to estimate burned area when combined with ancillary information on vegetation and fire-pixel clusters. The interim burned area data set produced from this work has been publicly available since December 2005 and has been used to study the interannual variability of global biomass burning emissions by van der Werf et al. [2006].

The tropical and sub-tropical diurnal fire cycles found in this research (Chapter 5) have important implications for all long-term active fire data records, in particular those produced from the AVHRR and ATSR sensors. The Stroppiana et al. [2000b] Global Fire Product, for example, was produced using 21 months of NOAA-11 AVHRR data from April 1992 to December 1993. During this time period, the NOAA-11 Equator crossing time drifted from about 15:00 to 16:00 local time. Although this 1-h shift seems small, for many regions it spans parts of the diurnal fire cycle where the rate of change is very high. This can cause artificial changes in the apparent number of AVHRR fire pixels recorded by the instrument (by up to 30%) over the 21-month time period. The impact of these artifacts on the results reported in

Dwyer et al. [1999, 2000a,b] is not known. Despite the stable orbit of the ENVISAT satellite, the diurnal fire cycles reported here also have implications for the use of the ATSR World Fire Atlas (WFA). The exclusive mapping of nighttime fires at about 22:30 local time is likely to distort the apparent relative amount of fire activity in different regions. Further investigation, including an intercomparison of the WFA and other fire products, is warranted.

The more rigorous derivation of the fire radiative power in a form suitable for a remote-sensing retrieval (Appendix A) revealed a previously-unknown dependence on sub-pixel fire fraction. While a preliminary analysis showed that this dependence could be neglected for very small and very large fires, the implications for intermediate size fires is not yet known and requires further investigation.

7.3 Future Directions

The global active fire product developed as part of this thesis provides the basis for long term monitoring of global fire activity using the two MODIS instruments. There is a need for the capabilities of these experimental satellites developed by NASA to transition to an operational agency for continued long term monitoring. This is currently planned through the Visible Infrared Imager/Radiometer Suite (VIIRS) sensor scheduled to fly on a suite of satellites comprising the National Polar-orbiting Operational Environmental Satellite System (NPOESS). The algorithm presented in Chapter 2 now forms the basis for the environmental data record on fire being

developed for the VIIRS instrument.

For the science community it is important that the data products are validated and consistent over time. For validation of the fire products, the coincident ASTER and MODIS data have provided a unique opportunity. In the coming months, there is a need to apply the ASTER algorithm developed in Chapter 3 to a global sample of scenes, thus achieving Stage 2 [Morisette et al., 2002] validation of the global product. Similar coincident high resolution and moderate resolution sensors designed for fire monitoring will be needed in the future. For consistency of fire observations it is important to consider the diurnal cycle of fire activity, either by accounting for bias or timing the overpass of future systems to observe near the peak. Results from this thesis would indicate this would be between 13:00 and 18:30 local time. Although a global network of geostationary satellites appears to hold considerable promise for capturing the diurnal cycle, consideration must be given to the spatial consistency. A micro-satellite constellation of polar orbiters designed specifically for fire monitoring might provide an alternative approach.

The research presented in this thesis has shown that, in combination with ancillary vegetation information, active fire data can be used to estimate burned area. While an interim approach, it has the potential to capture small agricultural fires which, because of their small size, often will not appear in forthcoming $\sim$1-km global burned area products. In the future, a hybrid of active fire and burned area products may provide the optimal combination for global fire monitoring.

Appendix A

Retrieval of Fire Radiative Power

The MODIS active fire product includes an estimate of the *fire radiative power* (FRP), a radiometric quantity related to fire intensity first proposed by Kaufman et al. [1998b], within each MODIS pixel. Among other applications, the FRP can be integrated over time to estimate combusted biomass, and is thus a topic of current research for its potential in quantifying pyrogenic greenhouse-gas emissions.

The original approach for retrieving FRP was developed by Kaufman et al. [1998b], who used simulated fire scenes to determine an empirical relationship expressing the FRP in terms of 4-μm brightness temperatures measured with the primary MODIS fire detection channels (bands 21 and 22). This approach was subsequently supplemented with an analytical technique developed by Wooster et al. [2003]. In this Appendix, the Wooster et al. approach is more rigorously derived, and several minor errors are corrected in the process. Some important caveats are also noted.

The FRP for N different fire components within a pixel, each having its own

temperature and area, is defined as [Wooster et al., 2003]

$$\mathrm{FRP} = A_{\mathrm{pix}}\,\epsilon\,\sigma \sum_{i=1}^{N} p_i T_i^4, \tag{A.1}$$

where p_i is the fraction of the pixel occupied by the i'th fire component at temperature T_i, A_{pix} is the area of the pixel, ϵ is the weighted mean emissivity of the fire components, and σ is the Stefan-Boltzmann constant. The fire fractions p_i satisfy the constraint that

$$\sum_{i=1}^{N} p_i = 1 \tag{A.2}$$

since in total they encompass the full spatial extent of the fire.

For operational satellite retrieval, the FRP must be cast in terms of radiometric quantities that can be remotely sensed with spaceborne sensors. As will be seen, a middle-infrared channel located near 4 μm uniquely permits a direct route to this goal. Using the notation in Table A.1, the observed top-of-atmosphere, middle-infrared radiance, L, for a pixel containing N black-body fire components and a Lambertian, non-fire background is given by

$$\begin{aligned} L \;=\; & \tau_{\mathrm{u}} \sum_{i=1}^{N} p_i B(\lambda, T_i) + \tau_{\mathrm{u}}\, p_{\mathrm{b}}\, \epsilon_{\mathrm{b}}\, B(\lambda, T_{\mathrm{b}}) \\ & + \tau_{\mathrm{u}}\, p_{\mathrm{b}} (1 - \epsilon_{\mathrm{b}}) \left[\tau_{\mathrm{d}}\, I_{\mathrm{sun}} \cos\phi + I_{\mathrm{atm}}\right] / \pi \\ & + L_{\mathrm{atm}}, \end{aligned} \tag{A.3}$$

where T_{b} is the temperature of the non-fire background occupying a relative pixel fraction of p_{b}, where

$$p_{\mathrm{b}} = 1 - \sum_{i=1}^{N} p_i. \tag{A.4}$$

We assume that a neighboring, fire-free pixel (or pixels) can be used to estimate the radiance of the non-fire fraction, and denote this radiance as $L_{\rm b}$. Assuming identical surface and atmospheric conditions in this pixel (or pixels), the observed middle-infrared radiance for the fire-free pixel is

$$L_{\rm b} = \tau_{\rm u}\,\epsilon_{\rm b}\,B(\lambda, T_{\rm b}) + \tau_{\rm u}(1-\epsilon_{\rm b})\left[\tau_{\rm d}\,I_{\rm sun}\cos\phi + I_{\rm atm}\right]/\pi + L_{\rm atm}. \tag{A.5}$$

Using this result, Eq. (A.3) may then be written as

$$L = \tau_{\rm u}\sum_{i=1}^{N} p_i B(\lambda, T_i) + p_{\rm b}\,L_{\rm b} + (1-p_{\rm b})L_{\rm atm}. \tag{A.6}$$

The term $(1-p_{\rm b})L_{\rm atm}$ will always be small compared to at least one of the first two terms in Eq. (A.6) and may therefore be neglected. Thus,

$$L \approx \tau_{\rm u}\sum_{i=1}^{N} p_i B(\lambda, T_i) + p_{\rm b}\,L_{\rm b}. \tag{A.7}$$

Table A.1: Notation for radiometric and other quantities.

T_i	kinetic temperature of i'th fire component
p_i	fraction of pixel occupied by i'th fire component
$T_{\rm b}$	kinetic temperature of non-fire background
p_b	non-fire fraction of pixel
$\epsilon_{\rm b}$	middle-infrared background emissivity
$\tau_{\rm u}$	upward middle-infrared atmospheric transmittance
$L_{\rm atm}$	upwelling mid-IR atmospheric radiance
ϕ	solar zenith angle
$\tau_{\rm d}$	downward mid-IR atmospheric transmittance (at angle ϕ)
$I_{\rm sun}$	extraterrestrial mid-IR solar irradiance
$I_{\rm atm}$	diffuse downwelling atmospheric mid-IR irradiance

As shown by Wooster et al. [2003], the Planck function may be approximated over a limited temperature range as

$$B(\lambda, T) \approx aT^b, \tag{A.8}$$

where a and b are empirical constants dependent upon both λ and the temperature range of interest. For wavelengths near 4 μm, choosing b = 4 yields a good approximation to the Planck function over a range of temperatures encompassing most flaming and many smoldering vegetation fires. Substituting this approximation into Eq. (A.7), we have

$$L \approx a\,\tau_{\mathrm{u}} \sum_{i=1}^{N} p_i T_i^4 + p_{\mathrm{b}}\,L_{\mathrm{b}}. \tag{A.9}$$

Solving Eq. (A.9) for the summation over all fire components shows that

$$\sum_{i=1}^{N} p_i T_i^4 \approx \frac{L - p_{\mathrm{b}}\,L_{\mathrm{b}}}{a\,\tau_{\mathrm{u}}}. \tag{A.10}$$

The fact that b = 4 is most serendipitous as it allows one to combine this result with the original definition of the FRP. Substituting Eq. (A.10) into Eq. (A.1), we find that

$$\boxed{\mathrm{FRP} \approx \frac{A_{\mathrm{pix}}\epsilon\sigma}{a\tau_{\mathrm{u}}}\left(L - p_{\mathrm{b}}\,L_{\mathrm{b}}\right).} \tag{A.11}$$

Our final expression for the FRP [Eq. (A.11)] differs slightly from that of Wooster et al. [2003], who reported that[1]

$$\mathrm{FRP} \approx \frac{A_{\mathrm{pix}}\epsilon\sigma}{a\,\epsilon_{\mathrm{MIR}}}(L - L_{\mathrm{b}}), \tag{A.12}$$

where ϵ_{MIR} is the middle-infrared fire emissivity. The minor differences explained as follows. The atmospheric transmittance τ_{u} does not appear in Eq. (A.12) because Wooster et al. implicitly assumed that all radiances were atmospherically corrected; here, we have not. For the $\sim$1-km sensors considered by Wooster et al., fires generally occupy only a small fraction of a pixel and, consequently, $p_{\mathrm{b}} \approx 1$, effectively bringing

[1]The original notation of Wooster et al. [2003] has been changed to match the notation used here.

the two different results into better agreement. For very large fires, $p_{\rm b} \ll 1$, and Eq. (A.12) will clearly overcompensate for the presence of a non-fire background in the fire pixel. However, the degree of overcompensation is absolutely negligible since, for such fires, $L \gg L_{\rm b}$. This is fortunate because, in the absence of independent information about fire size, there is really no way to estimate $p_{\rm b}$ without appealing to the problematic bispectral temperature and area retrieval discussed in Section 3.6.

The middle-infrared fire emissivity ($\epsilon_{\rm MIR}$) appearing in the denominator of Eq. (A.12) is more problematic as it does not fully account for departures from the assumption of black-body fire components. To account for such departures, one needs to incorporate the middle-infrared fire emissivity as well as an additional reflected solar component into Eq. (A.3), i.e.,

$$\begin{aligned} L &= \tau_{\rm u}\,\epsilon_{\rm MIR} \sum_{i=1}^{N} p_i B(\lambda, T_i) + \tau_{\rm u}\,p_{\rm b}\,\epsilon_{\rm b}\,B(\lambda, T_{\rm b}) \\ &\quad + \tau_{\rm u}\left[p_{\rm b}(1-\epsilon_{\rm b}) + (1-\epsilon_{\rm MIR})(1-p_{\rm b})\right]\left[\tau_{\rm d}\,I_{\rm sun}\cos\phi + I_{\rm atm}\right]/\pi \\ &\quad + L_{\rm atm}, \end{aligned} \tag{A.13}$$

If we now substitute our independent estimate of the background (non-fire) radiance, $L_{\rm b}$, into Eq. (A.13), we find that

$$\begin{aligned} L &= \tau_{\rm u}\,\epsilon_{\rm MIR} \sum_{i=1}^{N} p_i B(\lambda, T_i) + p_{\rm b}\,L_{\rm b} + (1-p_{\rm b})L_{\rm atm} \\ &\quad + \tau_{\rm u}(1-\epsilon_{\rm MIR})(1-p_{\rm b})\left[\tau_{\rm d}\,I_{\rm sun}\cos\phi + I_{\rm atm}\right]/\pi. \end{aligned} \tag{A.14}$$

This result is similar to Eq. (A.6), but contains the extra baggage of an additional term accounting for sunlight reflected by the fire. Due to the variability of the factors within

this term, it may not always be neglected, and consequently must propagate through the steps shown above into the final expression for the FRP. Accurate retrieval of the FRP for grey-body fire components may therefore require a relationship more complicated than that suggested by Eq. (A.12).

Appendix B

Burned Area Detection Algorithm

Burned area maps were produced using a prototype algorithm that uses the 500-m MODIS atmospherically-corrected Level 2G surface reflectance product [Vermote and Justice, 2002], the MODIS Level 3 daily active fire products [Justice et al., 2002], and the MODIS Level 3 96-day Land Cover Product [Friedl et al., 2002]. The algorithm, which is a major extension of an earlier method proposed by Roy et al. [1999], detects persistent changes in a daily vegetation-index (VI) time series derived from MODIS band 5 (1.2 μm) and band 7 (2.1 μm) surface reflectances, respectively denoted ρ_5 and ρ_7, where

$$\mathrm{VI} = \frac{\rho_5 - \rho_7}{\rho_5 + \rho_7}. \tag{B.1}$$

This index shows a significant decrease following a burn, and provides somewhat better discrimination of burned areas than the more commonly used Normalized Burn Ratio (NBR), an index defined similarly but with Landsat Thematic Mapper (TM) bands 4 (0.83 μm) and 7 (2.2 μm) [Miller and Yool, 2002].

The general detection approach is to first derive a summary map of persistent change from the VI time series, and then use spatial and temporal active fire

information to guide the statistical characterization of burn-related and non burn-related change within the scene. This information is used to estimate probabilistic thresholds suitable for classifying the scene into burned and unburned pixels. The approach ultimately identifies the date of burn, to the nearest day, for pixels within individual MODIS Level 3 tiles [Wolfe et al., 1998] at 500-m spatial resolution.

B.1 Composite change summary

The algorithm first examines the daily VI time series by considering observations within two adjacent sliding temporal windows of duration $W{=}10$ days; these windows are referred to as the *candidate pre-burn* and *candidate post-burn* windows, respectively. Within the k'th candidate pre-burn window, the trimmed mean [$\mathrm{VI}_{\mathrm{pre}}(k)$] and trimmed standard deviation [$\sigma_{\mathrm{pre}}(k)$] of all observations are computed. Statistics for the k'th candidate post-burn window are similarly computed and denoted $\mathrm{VI}_{\mathrm{post}}(k)$ and $\sigma_{\mathrm{post}}(k)$. The index k references the position within the daily time series on which the sliding windows are aligned (incrementing k moves both windows forward in time by one day). The time series of active fire observations for the pixel under consideration is also examined, and the occurrence of any such pixels in the time series is flagged.

A measure of temporal separability $S(k)$, defined as

$$S(k) = \frac{\Delta\mathrm{VI}(k)}{\sigma_{\mathrm{pre}}(k) + \sigma_{\mathrm{post}}(k)}, \tag{B.2}$$

where $\Delta\mathrm{VI}(k){=}\mathrm{VI}_{\mathrm{pre}}(k){-}\mathrm{VI}_{\mathrm{post}}(k)$, is evaluated for all k. For each pixel the

maximum separability $\max(S(k))=S(k_{\max})$ is identified. The date associated with the maximum change is the midpoint of the interval between the last observation in the pre-burn window and the first observation in the post-burn window. The time series for each pixel of the MODIS tile is processed, yielding composite images of $\Delta\mathrm{VI}(k_{\max})$ and $\mathrm{VI}_{\mathrm{post}}(k_{\max})$, and a composite map of active fire pixels detected during the time period being processed.

B.2 Identification of training samples

Having generated the composite imagery just described, a simple procedure is used to extract representative burned and unburned samples within each land cover class l present within the MODIS tile. To identify probable burned pixels, the composite active fire map is morphologically eroded. This eliminates the smallest fire-pixel clusters, which are less likely to be accompanied by a detectable burn scar (cf. Fig. 6.1). Burned training samples of $\Delta\mathrm{VI}(k_{\max})$ and $\mathrm{VI}_{\mathrm{post}}(k_{\max})$ are drawn from those pixels remaining in the eroded fire mask, and are partitioned by land cover class. In a complementary manner, dilating the composite active fire map provides a mask of pixels that are unlikely to have burned during the time period being processed, and training samples of unburned pixels for each land cover class are thus identified. Here more care is required since the active fire map will often greatly under-represent the spatial extent of large burns, so the radius of the dilation kernel is increased in proportion to the size of individual fire-pixel clusters. This is again consistent with the

empirical observation that large burns tend to be accompanied by large clusters of active fire pixels, and vice versa.

B.3 Classification of unambiguous burned and unburned pixels

The training samples extracted in the previous step are now used to derive conservative dynamic thresholds to classify unambiguous burned and unburned pixels. Pixels with land cover class l for which $\Delta\mathrm{VI}(k_{\max})$ is less than the upper quartile of $\Delta\mathrm{VI}(k_{\max})$ for all unburned training pixels in land cover class l are immediately labeled as *unburned*. Pixels with land cover class l for which $\Delta\mathrm{VI}(k_{\max})$ is greater than the upper quartile of $\Delta\mathrm{VI}(k_{\max})$, and $\mathrm{VI}_{\mathrm{post}}(k_{\max})$ is less than the lower quartile of $\mathrm{VI}_{\mathrm{post}}(k_{\max})$ for all burned training pixels in land cover class l are immediately classified as *burned*. Prior to performing this step an initial separability test is performed for each land cover class: if the distributions of $\Delta\mathrm{VI}(k_{\max})$ for the burned and unburned training samples show excessive overlap, all pixels within land cover class l are immediately classified as *unburned* and the quartile tests are not performed.

This step typically provides a final classification for 60% to 80% of all image pixels, resulting in a large reduction in the computational effort needed to process pixels in the remainder of the scene.

B.4 Classification of remaining pixels

Following the inital labeling of obvious burned and unburned pixels, one of two different approaches are then used to label the remaining unclassified pixels depending on the geographic region and time period being processed.

B.4.1 Region growing

In high-latitude regions having shorter MODIS revisit periods, and at lower latitudes where the majority of the area burned is dominated by large burn scars ($\gtrsim$100 km^2), region-growing is used to identify the remaining burned pixels within the MODIS tile being processed. Clusters of active fire pixels derived from the composite active-fire mask are used as seeds to iteratively "fill in" the surrounding burn scar. The values of $\Delta\mathrm{VI}(k_{\max})$ and $\mathrm{VI}_{\mathrm{post}}(k_{\max})$ for unclassified candidate pixels adjacent to a seed pixel are compared to the statistical distributions derived from the burned and unburned training samples. Bayes' rule is applied to estimate a posteriori probabilities for the candidate pixel and select the class to which it will be assigned. Additional temporal constraints are applied based on the burn dates of the parent seeds. Pixels classified as *burned* during the current iteration become seeds in the subsequent iteration. The process continues until no new seeds are found.

B.4.2 Contextual classification

In regions where the temporal sampling of active fires is less frequent, or relatively small burns ($<\sim$10 km^2) are abundant, an alternate classification approach is required. Region growing under these conditions will usually result in large omission errors since many smaller burns will lack active-fire seed pixels, and a contextual classifier is employed instead. In addition to using the spectral information available for the training pixels and the entire scene, the contextual classifier exploits the fact that both burned and unburned pixels tend to occur near pixels having the same burned or unburned status. Here, a Markov Random Field (MRF), a standard approach for modeling such spatial behavior, is employed. The MRF is defined by a probability density function that encodes the likelihood that a pixel is burned based on the state of its eight immediate neighbors. This information is incorporated with the spectral information provided by $\Delta\mathrm{VI}(k_{\max})$ and $\mathrm{VI}_{\mathrm{post}}(k_{\max})$, and each pixel not classified during step A.3 is assigned the class (*burned* or *unburned*) having the maximum a posteriori (MAP) probability. Estimation of these probabilities is performed using the iterated conditional modes (ICM) method described by Besag [1986]. ICM requires a rough preliminary classification to initiate the iterative process, and for this a naive Bayes classifier is used. The preliminary class assigned to each pixel within land cover class l is that which has the highest a posteriori probability estimated using Bayes' rule:

$$p_l(\mathrm{B}|\Delta\mathrm{VI}, \mathrm{VI}_{\mathrm{post}}) = \frac{p_l(\Delta\mathrm{VI}|\mathrm{B})\, p_l(\mathrm{VI}_{\mathrm{post}}|\mathrm{B})\, p_l(\mathrm{B})}{p_l(\mathrm{VI}, \Delta\mathrm{VI}_{\mathrm{post}})} \quad \text{(B.3)}$$

$$p_l(\mathrm{U}|\Delta\mathrm{VI}, \mathrm{VI}_{\mathrm{post}}) = \frac{p_l(\Delta\mathrm{VI}|\mathrm{U})\, p_l(\mathrm{VI}_{\mathrm{post}}|\mathrm{U})\, p_l(\mathrm{U})}{p_l(\mathrm{VI}, \Delta\mathrm{VI}_{\mathrm{post}})}, \quad \text{(B.4)}$$

where “B” and “U” denote the classes *burned* and *unburned*, respectively. (Note that the index $k_{\max}$ has been dropped in the above equations to reduce clutter.) Again making use of information provided by active fire observations, the a priori probability of a burned pixel $p_l(\mathrm{B})$ in land cover class l is estimated as the fraction of all pixels of land cover class l within the scene in which an active fire was detected during the time period being processed. From this $p_l(\mathrm{U}){=}1{-}p_l(\mathrm{B})$.

B.5 Validation

At present, validation of the 500-m burned area maps has been limited to Russia through comparison with maps generated manually from high resolution satellite imagery [Loboda and Csiszar, 2004]. Using 20 Landsat scenes acquired between 17 August 2001 and 19 August 2002, Loboda and Csiszar found good agreement between the burn scars mapped by the algorithm with those traced manually (Fig. B.1). Validation efforts are currently being extended to Australia and South America.

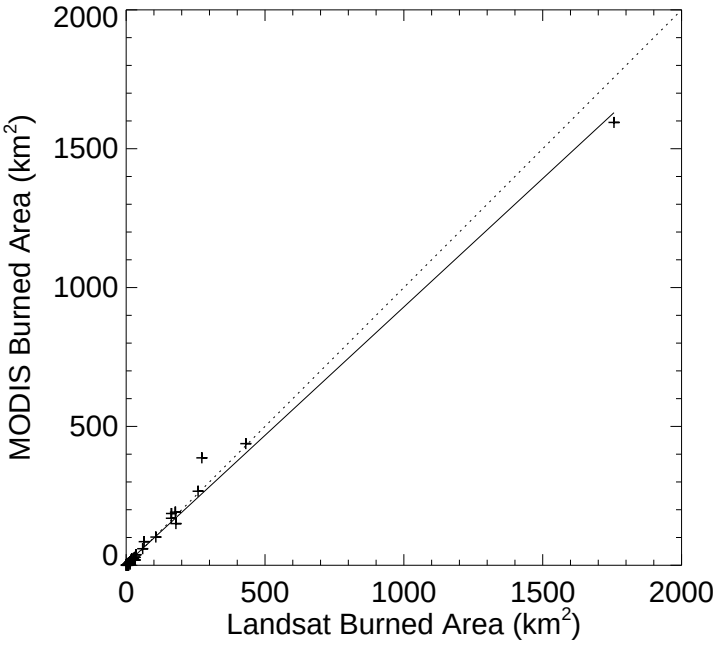

Figure B.1: Areas of 39 individual burn scars in Russia during 2001 and 2002 as mapped by 500-m burned area detection algorithm versus ground truth derived manually from Landsat imagery. The slope and intercept of the solid black regression line are 0.925 and 5.5 km^2, respectively, with a correlation of 0.996.

Appendix C

List of Acronyms

ASTER	Advanced Spaceborne Thermal Emission and Reflection Radiometer
ATSR	Along-Track Scanning Radiometer
AATSR	Advanced Along-Track Scanning Radiometer
AVHRR	Advanced Very High Resolution Radiometer
CIFFC	Canadian Interagency Forest Fire Centre
CAR	Central African Republic
CMG	Climate Modeling Grid
DMSP	Defense Meteorological Satellite Program (satellite)
ERBS	Earth Radiation Budget Satellite
FRE	fire radiative energy
FRP	fire radiative power
GFP	Global Fire Product
GOES	Geostationary Operational Environmental Satellite
IQR	interquartile range
MCF	mean cloud fraction
MODIS	Moderate Resolution Imaging Spectroradiometer
NDVI	Normalized Difference Vegetation Index
NH	northern hemisphere
NIFC	National Interagency Fire Center
OLS	Operational Linescan System
PDF	probability density function
SEVIRI	Spinning Enhanced Visible and Infrared Imager
SH	southern hemisphere
TRMM	Tropical Rainfall Measuring Mission (satellite)
UARS	Upper Atmospheric Research Satellite
VAS	Visible Infrared Spin Scan Radiometer Atmospheric Sounder
VCF	Vegetation Continuous Fields
VIRS	Visible and Infrared Scanner
WF_ABBA	Wildfire Automated Biomass Burning Algorithm

BIBLIOGRAPHY

N. J. Abram, M. K. Gagan, M. T. McCulloch, J. Chappell, and W. S. Hantoro. Coral reef death during the 1997 Indian ocean dipole linked to Indonesian wildfires. *Science*, 301:952–955, 2003.

F. Achard, H. D. Eva, A. Glinni, P. Mayaux, H.-J. Stibig, and T. Richards. Identification of deforestation hot spot areas in the humid tropics. Technical Report TREES Publications Series B, Research Report No. 4, EUR 18079 EN, European Commission, Luxembourg, 1998.

S. A. Ackerman, K. I. Strabala, W. P. Menzel, R. A. Frey, C. C. Moeller, and L. E. Gumley. Discriminating clear sky from clouds with MODIS. *Journal of Geophysical Research*, 103(D24):32141–32157, 1998.

M. O. Andreae. Biomass burning: its history, use, and distribution and its impact on environmental quality and global climate. In J. S. Levine, editor, *Global Biomass Burning*, pages 3–21. MIT Press, Cambridge, 1991.

A. F. Arellano, Jr., P. S. Kasibhatla, L. Giglio, G. R. van der Werf, and J. T. Randerson. Top down estimates of global CO sources using MOPITT measurements. *Geophysical Research Letters*, 31:L01104, 2004. doi: 10.1029/2003GL018609.

O. Arino and J.-M. Rosaz. 1997 and 1998 world ATSR fire atlas using ERS-2 ATSR-2 data. In L. F. Neuenschwander, K. C. Ryan, and G. E. Golberg, editors, *Proceedings of the Joint Fire Science Conference*, pages 177–182, Boise, Idaho, June 1999. University of Idaho and the International Association of Wildland Fire.

P. M. Barbosa, D. Stroppiana, and J.-M. Grégoire. An assessment of vegetation fire in Africa (1981-1991): Burned areas, burned biomass, and atmospheric emissions. *Global Biogeochemical Cycles*, 13(4):933–950, 1999.

J. E. Besag. On the statistical analysis of dirty pictures. *Journal of the Royal Statistical Society, Series B*, 48:259–302, 1986.

S. H. Boles and D. L. Verbyla. Comparison of three AVHRR based fire detection algorithms for interior Alaska. *Remote Sensing of Environment*, 72:1–16, 2000.

L. Boschetti, H. D. Eva, P. A. Brivio, and J.-M. J.-M. Grégoire. Lessons to be learned from the comparison of three satellite-derived biomass burning products. *Geophysical Research Letters*, 31:L21501, 2004. doi: 10.1029/2004GL021229.

L. Breiman, J. A. Friedman, R. A. Olshen, and C. J. Stone. *Classification and Regression Trees*. Chapman & Hall/CRC, Boca Raton, 1984.

L. Breiman and W. S. Meisel. General estimates of the intrinsic variability of data in nonlinear regression models. *Journal of the American Statistical Association*, 71: 301–307, 1976.

D. R. Cahoon, Jr., B. J. Stocks, J. S. Levine, W. R. Cofer, III, and K. P. O'Neill. Seasonal distribution of African savanna fires. *Nature*, 359:812–815, 1992.

N. Clerici, L. Boschetti, H. Eva, and J.-M Grégoire. Assessing vegetation fires activity and its drivers in West-Central Africa using MODIS and TRMM data. In *Proceedings of the International Geoscience and Remote Sensing Symposium*, volume 3, pages 2087–2090, Anchorage, Alaska, 2004. IEEE Computer Society. doi: 10.1109/IGARSS.2004.1370768.

P. J. Crutzen and M. O. Andreae. Biomass burning in the tropics: Impact on atmospheric chemistry and biogeochemical cycles. *Science*, 250:1669–1678, 1990.

P. J. Crutzen, L. E. Heidt, J. P. Krasnec, W. H. Pollock, and W. Seiler. Biomass burning as a source of atmospheric gases CO, H_2, N_2O, NO, CH_3Cl and COS. *Nature*, 282: 253–256, 1979.

I. Csiszar, A. Abuelgasim, Z. Li, J.-Z. Jin, R. Fraser, and W.-M. Hao. Interannual changes of active fire detectability in North America from long-term records of the Advanced Very High Resolution Radiometer. *Journal of Geophysical Research*, 108 (D2):4075–4084, 2003. doi: 10.1029/2001JD001373.

I. Csiszar, L. Denis, L. Giglio, C. O. Justice, and J. Hewson. Global fire distribution from MODIS. *International Journal of Wildland Fire*, 14:117–130, 2005.

P. J. Curran and P. M. Atkinson. Issues of scale and optimal pixel size. In A. Stein, F. van der Meer, and B. Gorte, editors, *Spatial Statistics for Remote Sensing*, pages 115–133. Kluwer Academic Publishers, Dordrecht, 2002.

R. Damoah, N. Spichtinger, C. Forster, P. James, I. Mattis, U. Wandinger, S. Beirle, T. Wagner, and A. Stohl. Around the world in 17 days – hemispheric-scale transport of forest fire smoke from Russia in May 2003. *Atmospheric Chemistry and Physics*, 4:1311–1321, 2004.

R. Damoah, N. Spichtinger, R. Servranckx, M. Fromm, E. W. Eloranta, I. A. Razenkov, P. James, M. Shulski, C. Forster, and A. Stohl. A case study of pyro-convection using transport model and remote sensing data. *Atmospheric Chemistry and Physics*, 6:173–185, 2006.

M. Desbois, T. Kayiranga, and B. Gnamien. Diurnal cycle of convective cloudiness over tropical africa observed from Meteosat: geographic characterization and interannual variations. *Annales Geophysicae*, 7:395–404, 1989.

J. L. Devore. *Probability and Statistics for Engineering and the Sciences*. Brooks/Cole Publishing Company, Monterey, 1987.

P. R. Dowty. The simulation of AVHRR data for the evaluation of fire detection techniques. In J. S. Levine, editor, *Biomass burning and global change: Remote sensing, modeling and inventory development, and biomass burning in Africa*, volume 1, pages 40–50. MIT Press, Cambridge, 1996.

J. Dozier. A method for satellite identification of surface temperature fields of subpixel resolution. *Remote Sensing of Environment*, 11:221–229, 1981.

B. N. Duncan, R. V. Martin, A. C. Staudt, R. Yevich, and J. A. Logan. Interannual and seasonal variability of biomass burning emissions constrained by satellite observations. *Journal of Geophysical Research*, 108(D2):4100, 2003. doi: 10.1029/2002JD002378.

E. Dwyer, J.-M. Grégoire, and J. M. C. Pereira. Climate and vegetation as driving factors in global fire activity. In J. L. Innes, M. Beniston, and M. M. Verstraete, editors, *Biomass Burning and its Inter-Relationships with the Climate System*, pages 171–191. Kluwer Academic Publishers, Dordrecht, 2000a.

E. Dwyer, J. M. C. Pereira, J.-M. Grégoire, and C. C. DaCamara. Characterization of the spatio-temporal patterns of global fire activity using satellite imagery for the period April 1992 to March 1993. *Journal of Biogeography*, 27:57–69, 1999.

E. Dwyer, S. Pinnock, and J.-M. Grégoire. Global spatial and temporal distribution of vegetation fires as determined from satellite observations. *International Journal of Remote Sensing*, 21:1289–1302, 2000b.

D. P. Edwards, L. K. Emmons, J. C. Gille, D. A. Chu, J.-L. Attié, L. Giglio, S. W. Wood, J. Haywood, M. N. Deeter, S. T. Massie, D. C. Ziskin, and J. R. Drummond. Satellite observed pollution from southern hemisphere biomass burning. *Journal of Geophysical Research*, 2006. In press.

D. P. Edwards, L. K. Emmons, D. A. Hauglustaine, D. A. Chu, J. C. Gille, Y. J. Kaufman, G. Pétron, L. N. Yurganov, L. Giglio, M. N. Deeter, V. Yudin, D. C. Ziskin, J. Warner, J.-F. Lamarque, G. L. Francis, S. P. Ho, D. Mao, J. Chen, E. I. Grechko, and J. R. Drummond. Observations of carbon monoxide and aerosols from the Terra satellite: Northern Hemisphere variability. *Journal of Geophysical Research*, 109:D24202, 2004. doi: 10.1029/2004JD004727.

C. D. Elvidge, K. E. Baugh, E. A. Kihn, H. W. Kroehl, and E. R. Davis. Mapping city lights with nighttime data from the DMSP Operational Linescan System. *Photogrammetric Engineering and Remote Sensing*, 63:727–734, 1997.

C. D. Elvidge, H. W. Kroehl, E. A. Kihn, K. E. Baugh, E. R. Davis, and W.-M. Hao. Algorithm for the retrieval of fire pixels from DMSP operational linescan system data. In J. S. Levine, editor, *Biomass burning and global change: Remote sensing, modeling and inventory development, and biomass burning in Africa*, volume 1, pages 73–85. MIT Press, Cambridge, 1996.

H. Eva and S. Flasse. Contextual and multiple-threshold algorithms for regional active fire detection with AVHRR data. *Remote Sensing Reviews*, 14:333–351, 1996.

H. Eva and E. F. Lambin. Remote sensing of biomass burning in tropical regions: sampling issues and multisensor approach. *Remote Sensing of Environment*, 64: 292–315, 1998.

N. L. Fisher. *Statistical Analysis of Circular Data*. Cambridge University Press, Cambridge, 1995.

M. D. Flannigan and T. H. Vonder Haar. Forest fire monitoring using NOAA satellite AVHRR. *Canadian Journal of Forest Research*, 16:975–982, 1986.

S. P. Flasse and P. Ceccato. A contextual algorithm for AVHRR fire detection. *International Journal of Remote Sensing*, 17:419–424, 1996.

A. S. Fotheringham, C. Brunsdon, and M. E. Charlton. *Geographically Weighted Regression: The Analysis of Spatially Varying Relationships*. John Wiley & Sons, West Sussex, 2002.

M. A. Friedl, D. K. McIver, J. C. F. Hodges, X. Y. Zhang, D. Muchoney, A. H. Strahler, C. E. Woodcock, S. Gopal, A. Schneider, A. Cooper, A. Baccini, F. Gao, and C. Schaaf. Global land cover mapping from MODIS: Algorithms and early results. *Remote Sensing of Environment*, 83:287–302, 2002.

S. Generoso, F.-M. Bréon, Y. Balkanski, O. Boucher, and M. Schulz. Improving the seasonal cycle and interannual variations of biomass burning aerosol sources. *Atmospheric Chemistry and Physics*, 3:1211–1222, 2003.

L. Giglio, I. Csiszar, and C. O. Justice. Global distribution and seasonality of active fires as observed with the Terra and Aqua MODIS sensors. *Journal of Geophysical Research*, 2006a. In press.

L. Giglio, J. Descloitres, C. O. Justice, and Y. J. Kaufman. An enhanced contextual fire detection algorithm for MODIS. *Remote Sensing of Environment*, 87:273–282, 2003a.

L. Giglio and C. O. Justice. Effect of wavelength selection on characterization of fire size and temperature. *International Journal of Remote Sensing*, 24(17):3515–3520, 2003.

L. Giglio and J. D. Kendall. Application of the dozier retrieval to wildfire characterization: A sensitivity analysis. *Remote Sensing of Environment*, 77:34–39, 2001.

L. Giglio and J. D. Kendall. Commentary on "Improving the seasonal cycle and interannual variations of biomass burning aerosol sources" by Generoso et al. *Atmospheric Chemistry and Physics*, 4:585–587, 2004.

L. Giglio, J. D. Kendall, and C. O. Justice. Evaluation of global fire detection algorithms using simulated AVHRR infrared data. *International Journal of Remote Sensing*, 20(10):1947–1985, 1999.

L. Giglio, J. D. Kendall, and R. Mack. A multi-year active fire data set for the tropics derived from the TRMM VIRS. *International Journal of Remote Sensing*, 24(22): 4505–4525, 2003b.

L. Giglio, J. D. Kendall, and C. J. Tucker. Remote sensing of fires with the TRMM VIRS. *International Journal of Remote Sensing*, 21(1):203–207, 2000.

L. Giglio, J. Pinzon, and P. S. Kasibhatla. Comment on "Seasonal, intraseasonal, and interannual variability of global land fires and their effects on atmospheric aerosol distribution" by Y. Ji and E. Stocker. *Journal of Geophysical Research*, 108(D24): 4754, 2003c. doi: 10.1029/2003JD003548.

L. Giglio, G. R. van der Werf, J. T. Randerson, G. J. Collatz, and P. S. Kasibhatla. Global estimation of burned area using MODIS active fire observations. *Atmospheric Chemistry and Physics*, 6:957–974, 2006b.

R. O. Green. Estimation of biomass fire temperature and areal extent from calibrated AVIRIS spectra. In *Summaries of the Sixth Annual JPL Airborne Earth Science Workshop*, JPL Publication 96-4, pages 105–113, Pasadena, 1996.

K. Hamilton. A note on the observed diurnal and semi-diurnal rainfall variation. *Journal of Geophysical Research*, 86(C):12122–12126, 1981.

M. C. Hansen, R. S. DeFries, J. R. G Townshend, M. Carroll, C. Dimiceli, and R. A. Sohlberg. Global percent tree cover at a spatial resolution of 500 meters: First results of the MODIS vegetation continuous fields algorithm. *Earth Interactions*, 7 (10), 2003. doi: 10.1175/1087-3562.

M. C. Hansen, R. S. DeFries, J. R. G. Townshend, and R. Sohlberg. Global land cover classification at 1 km spatial resolution using a classification tree approach. *International Journal of Remote Sensing*, 21:1331–1364, 2000.

W.-M. Hao, M.-H. Liu, and P. J. Crutzen. Estimates of annual and regional releases of CO_2 and other trace gases to the atmosphere from fires in the tropics, based on the FAO statistics for the period 1975–1980. In J. G. Goldammer, editor, *Fire in the Tropical Biota: Ecosystem Processes and Global Challenges*, pages 400–462. Springer-Verlag, Berlin, 1990.

C. L. Heald, D. J. Jacob, P. I. Palmer, M. J. Evans, G. W. Sachse, H. B. Singh, and D. R. Blake. Biomass burning emission inventory with daily resolution: Application to aircraft observations of Asian outflow. *Journal of Geophysical Research*, 108 (D21):8811, 2003. doi: 10.1029/2002JD003082.

P. Huber. *Robust Statistics*. Wiley, New York, 1981.

C. Ichoku, Y. J. Kaufman, L. Giglio, Z. Li, R. H. Fraser, J.-Z. Jin, and W. M Park. Comparative analysis of daytime fire detection algorithms using AVHRR data for the 1995 fire season in Canada: Perspective for MODIS. *International Journal of Remote Sensing*, 24:1669–1690, 2003.

A. Iwasaki, H. Fujisada, H. Akao, O. Shindou, and S. Akagi. Enhancement of spectral separation performance for ASTER/SWIR. In M. Strojnik and B. F. Andresen, editors, *Infrared Spaceborne Remote Sensing IX*, volume 4486, pages 42–50. SPIE, 2002.

D. Jaffe, I. Bertschi, L. Jaeglé, P. Novelli, J. S. Reid, H. Tanimoto, R. Vingarzan, and D. L. Westphal. Long-range transport of Siberian biomass burning emissions and impact of surface ozone in western North America. *Geophysical Research Letters*, 31:L16106, 2004. doi: 10.1029/2004GL020093.

Y. Ji and E. Stocker. An overview of the TRMM/TSDIS fire algorithm and product. *International Journal of Remote Sensing*, 23:3285–3303, 2002.

E. A. Johnson. *Fire and Vegetation Dynamics: Studies From the North American Boreal Forest*. Cambridge University Press, Cambridge, 1992.

C. O. Justice, L. Giglio, S. Korontzi, J. Owens, J. T. Morisette, D. Roy, J. Descloitres, S. Alleaume, F. Petitcolin, and Y. Kaufman. The MODIS fire products. *Remote Sensing of Environment*, 83:244–262, 2002.

C. O. Justice, J. D. Kendall, P. R. Dowty, and R. J. Scholes. Satellite remote sensing of fires during the SAFARI campaign using NOAA AVHRR data. *Journal of Geophysical Research*, 101(D23):23851–23863, 1996.

C. O. Justice, J.-P. Malingreau, and A. W. Setzer. Satellite remote sensing of fires: Potential and limitations. In P. J. Crutzen and J. G. Goldammer, editors, *Fire in the Environment*, pages 77–88. Wiley, New York, 1993.

E. S. Kasischke, N. L. Christensen, Jr., and B. J. Stocks. Fire, global warming and the mass balance of carbon in boreal forests. *Ecological Applications*, 5:437–451, 1995.

E. S. Kasischke, J. H. Hewson, B. Stocks, G. R. van der Werf, and J. Randerson. The use of ATSR active fire counts for estimating relative patterns of biomass burning – a study from the boreal forest region. *Geophysical Research Letters*, 30(18):1969, 2003. doi: 10.1029/2003GL017859.

E. S. Kasischke and J. E. Penner. Improving global estimates of atmospheric emissions from biomass burning. *Journal of Geophysical Research*, 109:D14S01, 2004. doi: 10.1029/2004JD004972.

Y. J. Kaufman, D. D. Herring, K. J. Ranson, and G. J. Collatz. Earth Observing System AM1 mission to Earth. *IEEE Transactions on Geoscience and Remote Sensing*, 36: 1045–1055, 1998a.

Y. J. Kaufman, C. Ichoku, L. Giglio, S. Korontzi, D. A. Chu, W.-M. Hao, R.-R. Li, and C. O. Justice. Fires and smoke observed from the Earth Observing System MODIS instrument – products, validation, and operational use. *International Journal of Remote Sensing*, 24:1765–1781, 2003.

Y. J. Kaufman, C. O. Justice, L. P. Flynn, J. D. Kendall, E. M. Prins, L. Giglio, D. E. Ward, W. P. Menzel, and A. W. Setzer. Potential global fire monitoring from EOS-MODIS. *Journal of Geophysical Research*, 103(D24):32215–32238, 1998b.

Y. J. Kaufman, A. Setzer, C. O. Justice, C. J. Tucker, M. C. Pereira, and I. Fung. Remote sensing of biomass burning in the tropics. In J. G. Goldammer, editor, *Fire in the Tropical Biota: Ecosystem Processes and Global Challenges*, pages 371–399. Springer-Verlag, Berlin, 1990.

P. J. Kennedy, A. S. Belward, and J.-M Grégoire. An improved approach to fire monitoring in West Africa using AVHRR data. *International Journal of Remote Sensing*, 15:2235–2225, 1994.

S. Langaas. Temporal and spatial distribution of savanna fires in Senegal and The Gambia, West Africa, 1989-90, derived from multi-temporal AVHRR night images. *International Journal of Wildland Fire*, 2(1):21–36, 1992.

S. Langaas. Diurnal cycles in savanna fires. *Nature*, 363:120, 1993a.

S. Langaas. A parametrised bispectral model for savanna fire detection using AVHRR night images. *International Journal of Remote Sensing*, 14:2245–2262, 1993b.

B. Langmann and A. Heil. Release and dispersion of vegetation and peat fire emissions in the atmosphere over Indonesia 1997/1998. *Atmospheric Chemistry and Physics*, 4:2145–2160, 2004.

R. Lasaponara, V. Cuomo, M. F. Macchiato, and T. Simoniello. A self-adaptive algorithm based on AVHRR multitemporal data analysis for small active fire detection. *International Journal of Remote Sensing*, 24(8):1723–1749, 2003.

T. F. Lee and P. M. Tag. Improved detection of hotspots using AVHRR 3.7 μm channel. *Bulletin of the American Meteorological Society*, 71:1722–1730, 1990.

Z. Li, Y. J. Kaufman, C. Ichoku, R. Fraser, A. Trishchenko, L. Giglio, J.-Z. Jin, and X. Yu. A review of AVHRR-based active fire detection algorithms: principles, limitation, and recommendations. In F. J. Ahern, J. G. Goldammer, and C. O. Justice, editors, *Global and Regional Vegetation Monitoring from Space: Planning a Coordinated International Effort*, pages 199–225. SPB Academic Publishing, The Hague, 2001.

Z. Li, S. Nadon, and J. Cihlar. Satellite-based detection of Canadian boreal forest fire: development and application of the algorithm. *International Journal of Remote Sensing*, 21:3057–3069, 2000.

X. Lin, L. D. Fowler, and D. A. Randall. Flying the TRMM satellite in a general circulation model. *Journal of Geophysical Research*, 107(D16):0–0, 2002.

T. Loboda and I. Csiszar. Estimating burned area from AVHRR and MODIS: validation results and sources of error. In *Proceedings of the Current Aspects of Remote Sensing of Earth from Space Conference*, Moscow, Russia, November 2004.

J.-P. Malingreau. The contribution of remote sensing to the global monitoring of fires in tropical and subtropical ecosystems. In J. G. Goldammer, editor, *Fire in the Tropical Biota: Ecosystem Processes and Global Challenges*, pages 337–370. Springer-Verlag, Berlin, 1990.

J. P. Malingreau and J.-M. Grégoire. Developing a global vegetation fire monitoring system for global change studies: A framework. In J. S. Levine, editor, *Biomass burning and global change: Remote sensing, modeling and inventory development, and biomass burning in Africa*, volume 1, pages 14–24. MIT Press, Cambridge, 1996.

J. P. Malingreau, G. Stephens, and L. Fellows. Remote sensing of forest fires: Kalimantan and North Borneo in 1982-3. *Ambio*, 14(6):314–315, 1985.

J. Mandel. *The Statistical Analysis of Experimental Data*. Dover, New York, 1984.

M. P. Martín, P. Ceccato, S. Flasse, and I. Downey. Fire detection and fire growth monitoring using satellite data. In E. Chuvieco, editor, *Remote Sensing of Large Wildfires*, pages 101–122. Springer-Verlag, Berlin, 1999.

E. Masuoka, A. Fleig, R. W. Wolfe, and F. Patt. Key characteristics of the MODIS data products. *IEEE Transactions on Geoscience and Remote Sensing*, 36:1313–1323, 1998.

M. Matson and J. Dozier. Identification of subresolution high temperature sources using a thermal IR sensor. *Photogrammetric Engineering and Remote Sensing*, 47: 1311–1318, 1981.

M. Matson and B. Holben. Satellite detection of tropical burning in Brazil. *International Journal of Remote Sensing*, 8:509–516, 1987.

W. P. Menzel and E. M. Prins. Monitoring biomass burning with the new generation of geostationary satellites. In J. S. Levine, editor, *Biomass burning and global change: Remote sensing, modeling and inventory development, and biomass burning in Africa*, volume 1, pages 56–64. MIT Press, Cambridge, 1996.

J. D. Miller and S. R. Yool. Mapping forest post-fire canopy consumption in several overstory types using multi-temporal Landsat TM and ETM data. *Remote Sensing of Environment*, 82:481–496, 2002.

D. Mollicone, H. D. Eva, and F. Achard. Human role in Russian wild fires. *Nature*, 440, 2006.

J. T. Morisette, L. Giglio, I. Csiszar, and C. O. Justice. Validation of the MODIS active fire product over Southern Africa with ASTER data. *International Journal of Remote Sensing*, 26:4239–4264, 2005a.

J. T. Morisette, L. Giglio, I. Csiszar, A. Setzer, W. Schroeder, D. Morton, and C. O. Justice. Validation of MODIS active fire detection products derived from two algorithms. *Earth Interactions*, 9(9):1–25, 2005b.

J. T. Morisette, J. L. Privette, and C. O. Justice. A framework for the validation of MODIS land products. *Remote Sensing of Environment*, 83:77–96, 2002.

K. Muirhead and A. Cracknell. Straw burning over Great Britain detected by AVHRR. *International Journal of Remote Sensing*, 65:827–833, 1985.

A. J. Negri, T. L. Bell, and L. Xu. Sampling and the diurnal cycle of precipitation using TRMM. *Journal of Atmospheric and Oceanic Technology*, 19:1333–1344, 2002.

M. Nishihama, R. Wolfe, D. Solomon, F. Patt, J. Blanchette, A. Fleig, and E. Masuoka. Modis level 1a earth location: algorithm theoretical basis document version 3.0. Technical Report SDST-092, NASA, 1997.

D. Oertel, K. Briess, W. Halle, M. Neidhardt, E. Lorenz, R. Sandau, F. Schrandt, W. Skrbek, H. Venus, I. Walter, B. Zender, B. Zhukov, J. G. Goldammer, A. C. Held, M. Hille, and H. Brueggemann. Airborne forest fire mapping with an adaptive infrared sensor. *International Journal of Remote Sensing*, 24:3663–3682, 2003.

D. W. Pack, C. J. Rice, B. J. Tressel, C. J. Lee-Wagner, and E. M. Oshika. Civilian uses of surveillance satellites. *Crosslink*, 1(1):2–8, 2000.

J. E. Penner, R. E. Dickinson, and C. A. O'Neill. Effects of aerosol from biomass burning of the global radiation budget. *Science*, 256:1432–1434, 1992.

J. M. Pereira, B. S. Pereira, P. Barbosa, D. Stroppiana, M. J. P. Vasconcelos, and J.-M. Grégoire. Satellite monitoring of fire in the EXPRESSO study area during the 1996 dry season experiment: Active fires, burnt area, and atmospheric emissions. *Journal of Geophysical Research*, 104(D23):30701–30712, 1999.

C. Potter, V. B. Genovese, S. Klooster, M. Bobo, and A. Torregrosa. Biomass burning losses of carbon estimated from ecosystem modeling and satellite data analysis for the Brazilian Amazon region. *Atmospheric Environment*, 35:1773–1781, 2001.

E. M. Prins, J. M. Feltz, W. P. Menzel, and D. E. Ward. An overview of GOES-8 diurnal fire and smoke results for SCAR-B and the 1995 fire season in South America. *Journal of Geophysical Research*, 103(D24):31821–31836, 1998.

E. M. Prins and W. P. Menzel. Geostationary satellite detection of biomass burning in South America. *International Journal of Remote Sensing*, 13:2783–2799, 1992.

E. M. Prins and W. P. Menzel. Trends in South American biomass burning detected with the GOES VAS from 1983-1991. *Journal of Geophysical Research*, 99(D8): 16719–16735, 1994.

E. M. Prins, J. Schmetz, L. P. Flynn, D. W. Hillger, and J. M. Feltz. An overview of diurnal active fire monitoring using a suite of international geostationary satellites. In F. J. Ahern, J. G. Goldammer, and C. O. Justice, editors, *Global and Regional Vegetation Monitoring from Space: Planning a Coordinated International Effort*, pages 145–170. SPB Academic Publishing, The Hague, 2001.

N. Ramankutty and J. A. Foley. Characterizing patterns of global land use: An analysis of global croplands data. *Global Biogeochemical Cycles*, 12:667–685, 1998.

T. Randriambelo, S. Baldy, M. Bessafi, M. Petit, and M. Despinoy. An improved detection and characterization of active fires and smoke plumes in south-eastern Africa and Madagascar. *International Journal of Remote Sensing*, 19(14): 2623–2638, 1998.

D. Rosenfeld. TRMM observed first direct evidence of smoke from forest fires inhibiting rainfall. *Geophysical Research Letters*, 26:3105–3108, 1999.

D. P. Roy, L. Giglio, J. D. Kendall, and C. O. Justice. A multitemporal active-fire based burn scar detection algorithm. *International Journal of Remote Sensing*, 20: 1031–1038, 1999.

D. P. Roy, P. E. Lewis, and C. O. Justice. Burned area mapping using multi-temporal moderate spatial resolution data – a bi-directional reflectance model-based expectation approach. *Remote Sensing of Environment*, 83:263–286, 2002.

M. L. Salby and P. Callaghan. Sampling error in climate properties derived from satellite measurements: Consequences of undersampled diurnal variability. *Journal of Climate*, 10:18–36, 1997.

R. J. Scholes, J. D. Kendall, and C. O. Justice. The quantity of biomass burned in southern Africa. *Journal of Geophysical Research*, 101(D19):23667–23676, 1996.

M. Schultz. On the use of ATSR fire count data to estimate the seasonal and interannual variability of vegetation fire emissions. *Atmospheric Chemistry and Physics*, 2:387–395, 2002.

C. A. Seielstad, J. P. Riddering, S. R. Brown, L. P. Queen, and W.-M. Hao. Testing the sensitivity of a MODIS-like daytime active fire detection model in alaska using NOAA/AVHRR infrared data. *Photogrammetric Engineering and Remote Sensing*, 68:831–838, 2002.

W. Seiler and P. J. Crutzen. Estimates of gross and net fluxes of carbon between the biosphere and atmosphere from biomass burning. *Climatic Change*, 2:207–247, 1980.

A. W. Setzer and M. C. Pereira. Amazonia biomass burnings in 1987 and an estimate of their tropospheric emissions. *Ambio*, 20:19–22, 1991.

M. W. Shephard and E. J. Kennelly. Effect of band-to-band coregistration on fire property retrievals. *IEEE Transactions on Geoscience and Remote Sensing*, 41: 2648–2661, 2003.

M. Simon, S. Plummer, F. Fierens, J. J. Hoelzemann, and O. Arino. Burnt area detection at global scale using ATSR-2: The GLOBSCAR products and their qualification. *Journal of Geophysical Research*, 109:D14S02, 2004. doi: 10.1029/2003JD003622.

R. V. Soares. Fire in some tropical and subtropical South American vegetation types: An overview. In J. G. Goldammer, editor, *Fire in the Tropical Biota: Ecosystem Processes and Global Challenges*, pages 63–81. Springer-Verlag, Berlin, 1990.

A. J. Soja, A. I. Sukhinin, D. R. Cahoon, Jr., H. H. Shugart, and P. W. Stackhouse, Jr. AVHRR-derived fire frequency, distribution and area burned in Siberia. *International Journal of Remote Sensing*, 25:1939–1960, 2004.

D. G. Streets, K. F. Yarber, J. H. Woo, and G. R. Carmichael. Biomass burning in Asia: Annual and seasonal estimates and atmospheric emissions. *Global Biogeochemical Cycles*, 17(4):1099, 2003. doi: 10.1029/2003GB002040.

D. Stroppiana, P. A. Brivio, and J.-M. Grégoire. Modelling the impact of vegetation fires, detected from NOAA-AVHRR data, on tropospheric chemistry in tropical Africa. In J. L. Innes, M. Beniston, and M. M. Verstraete, editors, *Biomass Burning and its Inter-Relationships with the Climate System*, pages 193–213. Kluwer Academic Publishers, Dordrecht, 2000a.

D. Stroppiana, S. Pinnock, and J.-M. Grégoire. The Global Fire Product: daily fire occurrence from April 1992 to December 1993 derived from NOAA AVHRR data. *International Journal of Remote Sensing*, 21:1279–1288, 2000b.

A. I. Sukhinin, N. H. F. French, E. S. Kasischke, J. H. Hewson, A. J. Soja, I. A. Csiszar, E. J. Hyer, T. Loboda, S. G. Conard, V. I. Romasko, E. A. Pavlichenko, S. I. Miskiv, and O. A. Slinkina. Satellite-based mapping of fires in russia: New products for fire management and carbon cycle studies. *Remote Sensing of Environment*, 93:546–564, 2004.

K. Tansey, J.-M Grégoire, D. Stroppiana, A. Sousa, J. Silva, J. M. C. Pereira, L. Boschetti, M. Maggi, P. A. Brivio, R. Fraser, S. Flasse, D. Ershov, E. Binaghi, D. Graetz, and P. Peduzzi. Vegetation burning in the year 2000: Global burned area estimates from SPOT VEGETATION data. *Journal of Geophysical Research*, 109 (D14S03), 2004. doi: 10.1029/2003JD003598.

W. Thiao and O. M. Turpeinen. Large-scale variations in tropical cold cloudiness based on a simple cloud indexing method. *Journal of Climate*, 5:173–180, 1992.

G. R. van der Werf, J. T. Randerson, G. J. Collatz, and L. Giglio. Carbon emissions from fires in tropical and subtropical ecosystems. *Global Change Biology*, 9: 547–562, 2003.

G. R. van der Werf, J. T. Randerson, G. J. Collatz, L. Giglio, P. S. Kasibhatla, A. F. Arellano, Jr., S. C. Olsen, and E. S. Kasischke. Continental-scale partitioning of fire emissions during the 1997 to 2001 El Niño/La Niña period. *Science*, 303:73–76, 2004.

G. R. van der Werf, J. T. Randerson, L. Giglio, G. J. Collatz, P. S. Kasibhatla, and A. F. Arellano, Jr. Interannual variability of global biomass burning emissions from 1997 to 2004. *Atmospheric Chemistry and Physics Discussions*, 6:3175–3226, 2006.

E. F. Vermote and N. Z. El Saleous C. O. Justice. Operational atmospheric correction of the MODIS data in the visible to middle infrared: First results. *Remote Sensing of Environment*, 83:97–111, 2002.

J. M. Wallace. Diurnal variations in precipitation and thunderstorm frequency over the conterminous United States. *Monthly Weather Review*, 103:406–419, 1975.

M. G. Weber and M. D. Flannigan. Canadian boreal forest ecosystem structure and function in a changing climate: impact on fire regimes. *Environmental Reviews*, 5: 145–166, 1997.

R. J. Whelan. *The Ecology of Fire*. Cambridge University Press, Cambridge, 1995.

R. E. Wolfe, D. P. Roy, and E. Vermote. MODIS land data storage, gridding, and compositing methodology: Level 2 grid. *IEEE Transactions on Geoscience and Remote Sensing*, 36:1324–1338, 1998.

M. J. Wooster. Small-scale experimental testing of fire radiative energy for quantifying mass combusted in natural vegetation fires. *Geophysical Research Letters*, 29(21): 2027, 2002. doi: 10.1029/2002GL015487.

M. J. Wooster and Y. H. Zhang. Boreal forest fires burn less intensely in Russia than in North America. *Geophysical Research Letters*, 31:L20505, 2004. doi: 10.1029/2004GL020805.

M. J. Wooster, B. Zhukov, and D. Oertel. Fire radiative energy for quantitative study of biomass burning: derivation from the BIRD experimental satellite and comparison to MODIS fire products. *Remote Sensing of Environment*, 86:83–107, 2003.

Y. Yamaguchi, A. B. Kahle, H. Tsu, T. Kawakami, and M. Pniel. Overview of Advanced Spaceborne Thermal Emission and Reflection Radiometer (ASTER). *IEEE Transactions on Geoscience and Remote Sensing*, 46:1062–1071, 1998.